In-Depth Study and Applications of 2D Functional Materials: Twisted Multilayer Graphene and Metal Wire Networks

A thesis
Submitted for the Degree of
DOCTOR OF PHILOSOPHY
by
Nikita Gupta

JNCASR

Chemistry and Physics of Materials Unit,
Jawaharlal Nehru Centre for Advanced Scientific
Research, Bangalore – 560064
(A Deemed to be University)
July - 2020

Dedicated to,

My mentor,

Prof. Giridhar U. Kulkarni

DECLARATION

I hereby declare that the thesis entitled, "**In-depth study and applications of 2D functional materials: Twisted multilayer graphene and Metal wire networks.**" is an authentic record of research work carried out by me at the Chemistry and Physics of Materials Unit, Jawaharlal Nehru Centre for Advanced Scientific Research, Bangalore, India under the supervision of Professor Giridhar U. Kulkarni and it has not been submitted elsewhere for the award of any degree or diploma.

In keeping with the general practice in reported scientific observations, due acknowledgement has been made whenever the work described is based on the findings of other investigators. Any omission that might have occurred due to oversight or error in judgement is regretted.

Nikita Gupta

CERTIFICATE

Certified that the work described in this thesis titled "**In-depth study and applications of 2D functional materials: Twisted multilayer graphene and Metal wire networks**" has been carried out by **Ms. Nikita Gupta** at the Chemistry and Physics of Materials Unit, Jawaharlal Nehru Centre for Advanced Scientific Research, Bangalore, India under my supervision and that it has not been submitted elsewhere for the award of any degree or diploma.

Professor Giridhar U. Kulkarni

(Research Supervisor)

Acknowledgements

I would like to thank the following people, without whom I would not have been able to make it through my research during PhD!

My supervisor, **Professor Giridhar U. Kulkarni**, who could recognise my potential even before I did, whose insight always made a given experiment ten times faster, who mentored me to become my best self, and who also inculcated in all his students great presentation skills, will continue to remain my motivation behind continuing research. It is a privilege to have worked under his guidance.

"Bharat Ratna" **Professor C. N. R. Rao** has been an inspiration in devoting my life to science. And I am extremely grateful to him for providing the best possible facility for carrying out research at JNCASR and for always keeping science first. I thank JNCASR for funding and IGSTC project partners for daily and travel allowances during German collaboration.

I am thankful to Prof. Mukundan Thelakkat, Tanaji P. Gujar and Chetan R. Singh and the group at University of Bayreuth for collaborative research and for helping me to have a good experience in Bayreuth, Germany. I also thank Dr. K. D. M. Rao, Dr. Ritu Gupta, Dr. Ankush Kumar, Dr. Umesha Mogera, Professor F. C. Krebs, Dr. Amy Marconnet, Prof. T. S. Fisher, Kartikeya Srivastava and Sunil Walia for fruitful collaboration within the group.

I also want to thank the past and present chairmen of our department, Chemistry and Physics of Materials Unit for their support and encouragement throughout. I want

Preface

This thesis work pertains to understanding the landscape of a new type of graphene system, called twisted multilayer graphene and various applications of metal mesh network obtained using crackle lithography. It is divided into five chapters.

Chapter 1 introduces nanoscale and nanomaterials of different dimensionality. It is discussed how a collection of 1D materials may give it a dimension between 1 and 2, and for a collection of 2D materials, a mixed dimensionality between 2 and 3. The later sections review the applications of various types of graphene and of metal wire network. Lastly, the scope of thesis is discussed. **Chapter 2** lists the characterisation techniques used in the thesis work.

Chapter 3a deals with the fabrication of metal mesh network by the crackle templating method, using electroless process of depositing metal. The method was utilised for making front electrodes of Si solar cells. The commercial crystalline Si solar cell has a high manufacturing cost because of the top electrode metallization of textured cell surface, which typically involves screen printing. The highly textured surface poses a challenge for the conventional recipes even for those involving nanomaterials. The Ni mesh directly laid on the surface employing crackle templating method is shown to have conformal contact with the surface, thus improving the efficiency of the cells, their stability and most importantly, potentially reduction in the fabrication cost. **Chapter 3b** demonstrates another application of the metal mesh for strain sensing, specifically for delineating small movements in the human body. Monitoring live movements is becoming increasingly important for biomedical and huma- machine technologies, for

which high sensitivity and fast response are of utmost importance. The chapter describes the fabrication of Au mesh, partially embedded in polydimethylsiloxane. The semi-embedded morphology of the network gives the sensor sturdiness and ease in making contact. In-situ scanning electron microscopy and infrared thermal microscopy analysis have revealed that nanometric break junctions form throughout the wire network, leading to a large change in sheet resistance of the mesh. The sensor exhibits high sensitivity with a gauge factor of 108 and ultrafast response of 0.03 s. High repeatability as well as cyclic stability have been demonstrated in the live examples involving human body activities, importantly while mounting the sensor in strategic remote locations way from the active sites where strains are the highest. The latter part of the chapter deals with the formation of break junction in the Au network on stretching. These break-junctions get healed in the presence of an external bias due to electromigration. In-situ scanning electron microscopy confirms the healing process.

Chapter 4a pertains to studies on a new form of graphene namely, twisted multilayer graphene, by Raman and selective area electron diffraction measurements, importantly both on the same locations. This type of graphene contains twists among the layers for which, a descriptor, termed as turbostratic factor has been described, which essentially takes into account the average value of twist angles and their distribution. The factor normalised with respect to factorial of number of twists, signifies various ways of ordering the twists. The factor forms a monotonic relation with the 2D intensity of Raman, and this trend hitherto not known, is widely applicable to other 2D systems, particularly produced by techniques such as CVD, where twist is an inherent nature.

This graphene used in the study exhibits a network of wrinkles and ripples, typical of high 2D crystallinity. Joule heating of the wrinkles in twisted multilayer graphene, discussed in **chapter 4b**, reveals that the current flowing through the wrinkles is much higher than the flatter regions. The wrinkles give graphene stretchability which is otherwise not possible for a flat layered material. This property was exploited in designing a sensor with high stretchability and high sensitivity. **Chapter 5** presents the summary and outlook for the thesis work.

Table of Contents

Chapter 1

Introduction

1.1 Nanoscale and nanomaterials

The word "nano" derives from the Latin word *nanus* meaning dwarf. The term is used in our metric system as a prefix to denote one billionth (10^{-9}) of a quantity such as metre, kilogram, second etc.[1] A nanometre is one billionth times smaller than a metre. In perspective, it is analogous to comparing the size of a mustard seed with respect to that of earth (see Figure 1.1). That is how small a nanometre is, so small that unless a powerful microscope is used, it cannot be perceived. A nanometre is used to measure things that are very small such as atoms and molecules, the smallest pieces of everything around us. For example, a human hair is about 100,000 nanometres wide (see Figure 1.2a), red blood cell is ~5000 nm, which is effectively ~5 μm in size (see Figure 1.2b), a DNA is 2 nm wide (see Figure 1.2c) and a water molecule is less than one nanometre. The European Commission defined nanomaterial as a material in an unbound state or as aggregate or as an agglomerate and for 50% or more of particles in the number size distribution having one or more external dimensions in the size range 1 nm – 100 nm.[2]
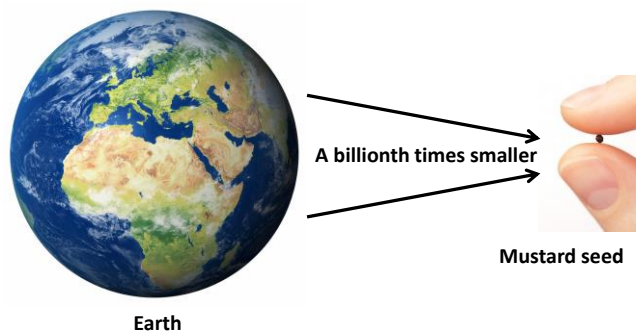
Figure 1.1 Size comparison. Shrinking earth, a billion times, the size of a mustard seed is obtained. This is the size difference between a metre and a nanometre. (Image sources: google images)
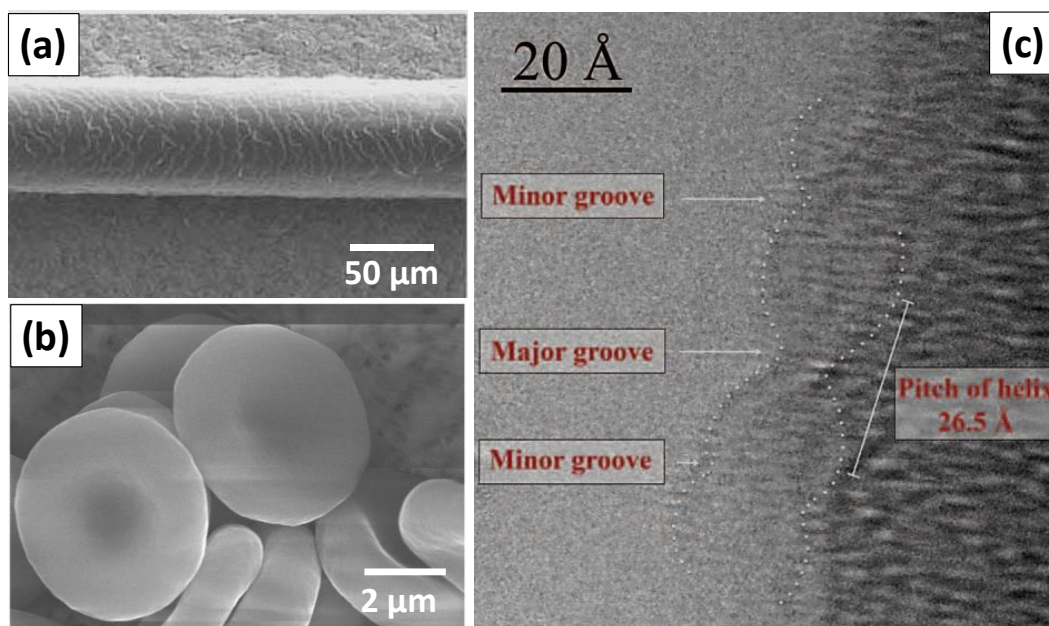
Figure 1.2 Microscopy of objects in daily life. (a) SEM of a hair strand has texture, tens of nanometers in size.[3] (b) SEM of red blood cells[4] and(c) A DNA helix marked by dotted lines.[5]

The scientific community generally attributes the first acknowledgement of importance of nanoscale range to the brilliant Nobel Laureate physicist Richard Feynman, when he gave the lecture, "There's Plenty of Room at the Bottom", meaning

that working in the nanoscale range would open a great deal of future opportunities. He conceptualised the nanotechnology field by saying that a day will come when things will be miniaturised, when huge amount of information could be recorded in small spaces and when machines like computers could be made smaller and compact. This would depend on the choice of speciality materials with well-defined properties. At a broader level, materials can be categorised into two types: structural materials and functional materials.

Structural materials are used for their load bearing capacities which are measured by properties such as elastic modulus, yield strength, ultimate tensile strength, hardness, ductility, fracture limit, fatigue and creep resistance. These materials include cast iron,
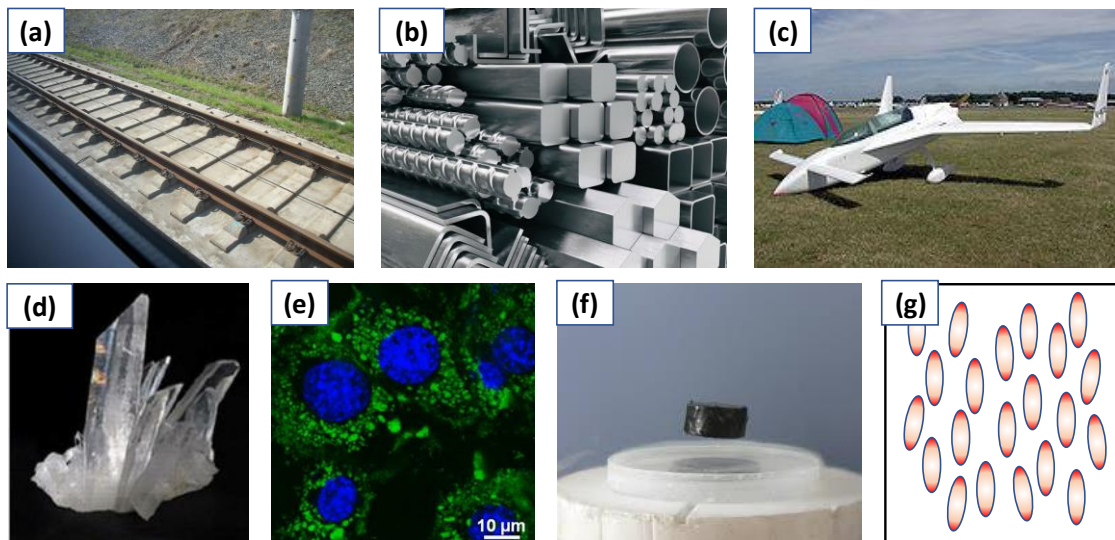
Figure 1.3 Structural and functional materials.(a) Fibre reinforced concrete track slab, (b) stainless steel, (c) light composite aircraft, (d) quartz crystal, natural piezoelectric material, (f) Fluorescent silica nanobeads, (g) magnet levitating above a superconductor below the critical temperature and (h) schematic of liquid crystalline physical gel. (Image source: google images, Wikipedia)

reinforced concrete (see Figure 1.3a), stainless steel (see Figure 1.3b), light composites for aircrafts (see Figure 1.3c) etc.[6]

Functional materials are those which respond to some external stimuli. They display a physical property which is of use, such as optical (including fluorescence, phosphorescence and Raman scattering), electrical (including photoconductors and superconductors), dielectrics (piezoelectrics, ferroelectrics, thermoelectrics and liquid crystals), magnetics, etc (see Figure 1.3d-g).

1.2 Nanomaterials of different dimensionalities
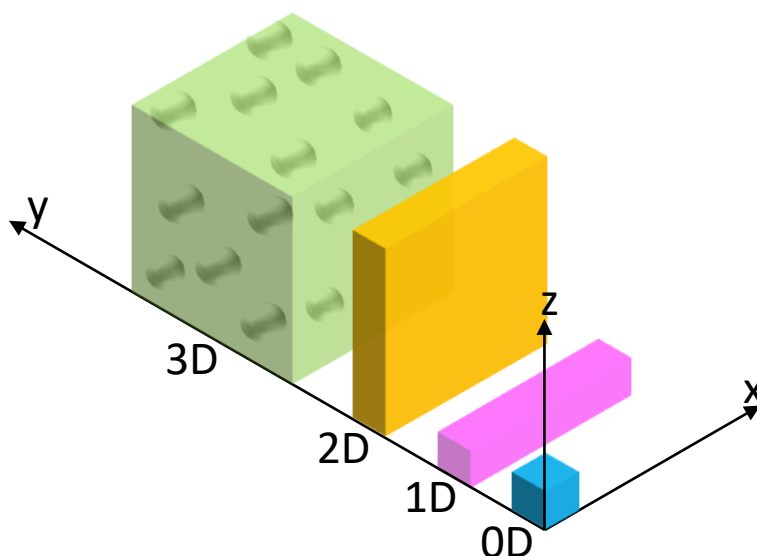
Figure 1.4 A schematic of how nanomaterials of different dimensionalities look like.

These materials form the basis of technology and that is the reason a specific property in a material is demanded for a given application. For example, the high electrical conductivity of copper is useful for making electrical circuits, low density of aluminium is useful for designing the body of an aircraft, the noble metals are used to make ornaments, etc. This often makes us think that the properties of a material are

solely dependent on what it constitutes, which is not always the case. One more thing that is responsible for giving a material its unique property is its size, especially when it is in the nano regime. Nanomaterials have different chemical and physical properties owing to their unique sizes. Classification of nanomaterials is based on the number of dimensions that are not confined to the nanoscale (<100 nm) as shown in the schematic in Figure 1.4. The various types are described below:

Zero dimensional (0D): Also called nanoparticles, the 0D materials are defined as nano-objects with all three dimensions in the nanoscale, whose longest and shortest edge do not differ by more than a factor of three.[7] They are surrounded by an interface typically consisting of ions, inorganic and organic materials. They behave as a whole unit with respect to their transport and properties. When these particles have at least one dimension between 1 nm and 10 nm and have a narrow size distribution, these are called as nanoclusters. Nanopowders are agglomerates of ultrafine particles, nanoparticles, or nanoclusters. Single-domain ultrafine particles are often termed as nanocrystals. Nanoparticles having optical and electronic properties are called as quantum dots (see Figure 1.5b). Just like atoms and molecules, these have bound and discrete electronic states. As they tightly confine either electrons or holes, they have properties intermediate between bulk semiconductors and discrete atoms or molecules. Nanoparticles can be used for a variety of practical applications such as in manufacturing scratchproof eyeglasses, in crack-resistant paints, in transparent sunscreens, etc. As shown in Figure 1.5a, the nano size of zinc oxide (ZnO) particles in a sunscreen allow them to reflect light efficiently, thereby blocking sunlight. Quantum

dots (see Figure 1.5b) can be utilized in diode lasers,[8] solar cells,[9] displays,[10] photocatalysts,[11] etc as they have sharper density of states.
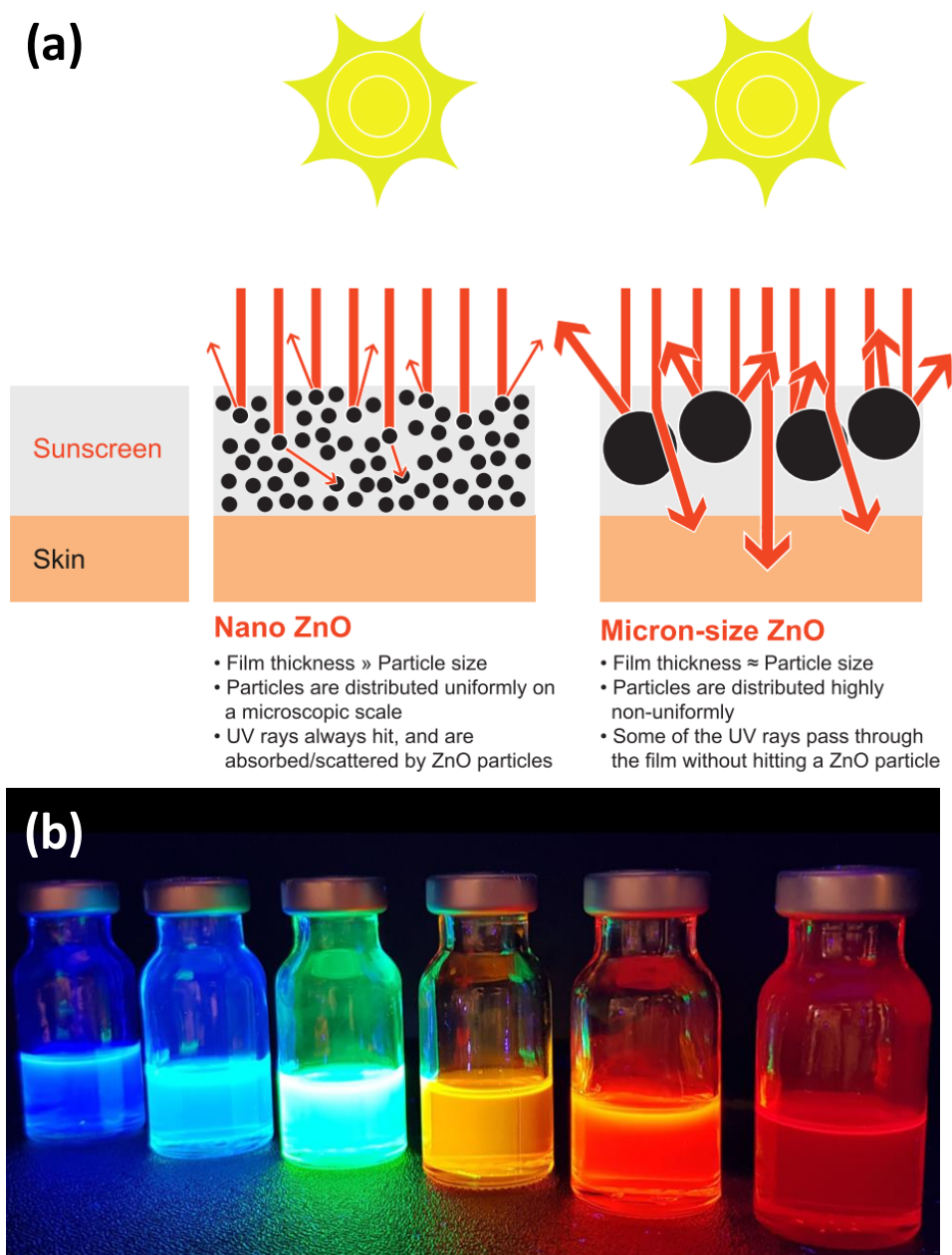
Figure 1.5 0D materials. Applications of 0D materials for (a) making transparent sunscreens and (b) quantum dots. (Image sources: google images)
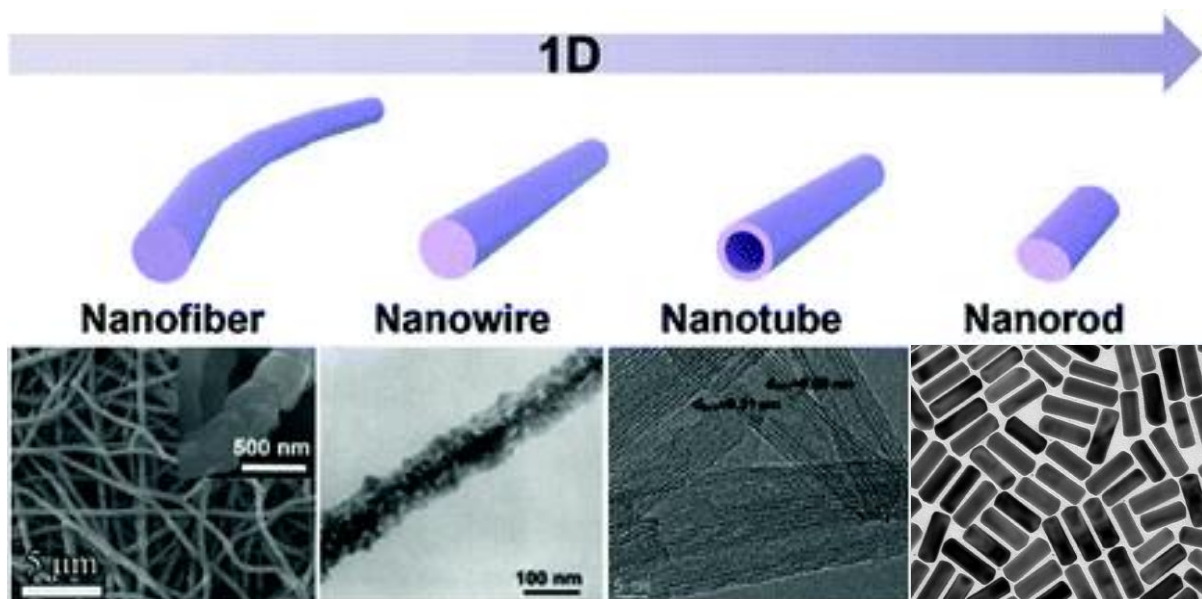
Figure 1.6 1D nanomaterials. Various types of 1D nanomaterials with corresponding microscopy images. Reproduced with permission.[12]

One dimensional (1D): When one dimension of the nanomaterial is outside the length scale 1-100 nm, then those are called 1D nanomaterials which include nanowires, nanofibers, nanobelts, nanorods and nanotubes. Nanowires have aspect ratio up to 1000 while nanorods have between 2-15, but both are solid nanostructure, nanotubes on the other hand are hollow (see Figure 1.6). 1D nanomaterials have unique structure that offer facile electronic and ionic transport and strong tolerance to stress change, for applications in energy storage systems, electronics, magnetism, optics and catalysis.[13] They have been utilized for variety of applications such as photoluminescence of ZnO nanorods, heating efficiency of iron nanowires, thermal stability and optical properties of polyvinyl alcohol composite nanofibers, electrical properties of half-doped manganite nanowire, adjusting magnetic properties of Co nanowires by changing the diameter.[14]

Two dimensional (2D): Sometimes also called single-layer materials, 2D materials are the crystalline materials consisting of a single layer of atoms, where two dimensions of the nanomaterial are outside the nanometre length scale. To date, approximately 700 2D materials have been predicted to be stable, although many are yet to be synthesised. The first 2D material was graphene (see Figure 1.7a) which was isolated from graphite in 2004 by micromechanical cleavage, by Andre Geim and Konstantin Novoselov[15] (discussed in detail in Section 1.2.1). Other single-layered elemental 2D materials do not have a strictly flat structure as is in graphene because of prevalent sp^3 bonding and are buckled (see Figure 1.7b). These elemental 2D materials can be metal (single or double layers of platinum, palladium, rhodium), semi-metal (graphene, silicene, germanene), semiconducting (phosphorene, antimonene) or insulating (stanene, bismuthene). Apart from elemental, 2D materials also occur in the form of compounds, the simplest example of which is graphyne, which has a lattice of benzene rings connected by acetylene bonds and has mixed hybridisation because of a few sp^3 bonds and a few sp^2 bonds. A perfect analogue of graphene is boron nitride which has a flat honeycomb lattice of alternating boron and nitrogen atoms. It has a high band gap ranging from 5 to 6 eV,[16] which makes it an excellent insulator. There is another class of compound 2D materials called transition metal dichalcogenides such as molybdenum disulphide and tungsten diselenide which consist of a unit of one layer of a transition metal atoms covalently bonded to two layers of chalcogen atoms. Because of the presence of direct bandgap, these monolayers have potential applications in electronics. The most recent 2D materials are MXenes which are layered transition metal carbides or carbonitrides.

Owing to their high electrical conductivity combined with hydrophilic surface, this material holds promise in energy storage applications, gas sensing and composites.
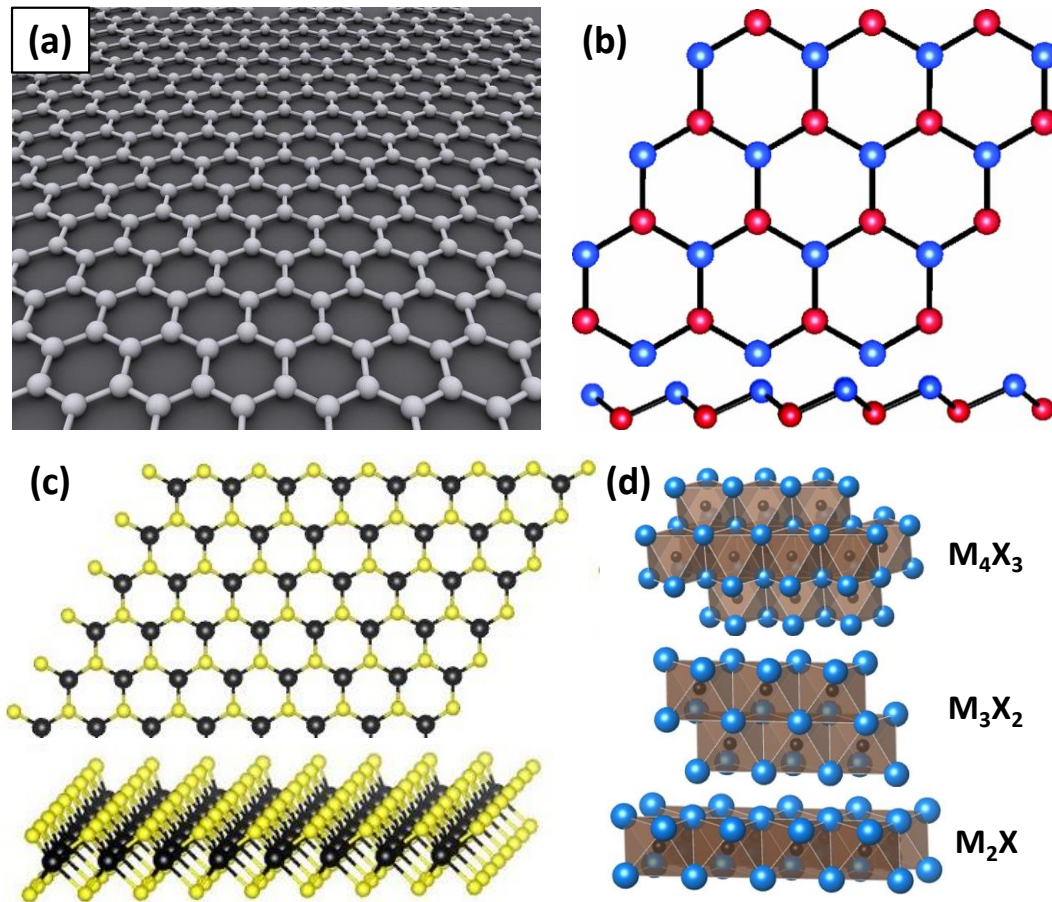
Figure 1.7 Schematics of various 2D materials like, (a) graphene, (b) buckled elemental layers like silicene, germanene, stanene, plumbene etc, in top view and cross-sectional view (c) transition metal dichalcogenides in top view and cross-sectional view and (d) MXenes. (Image source: Wikipedia)

Three dimensional (3D): Materials having all the three dimensions larger than the nanometer length scale but containing features on the nanoscale are called 3D materials, which include nanocomposites, nanostructured films, nanoporous materials, nanocrystalline materials and nanotextured surfaces. Nanocomposites are solid

materials made up of multiple phases where at least one of the phases is in nano regime or the repeat distance between various phases is in the nano regime. The properties of these materials are different from those of the constituent phases and depend on the size of these phases. For example, when the phases are as small as 5 nm, they show catalytic activities and when the phases are ~50 nm, they may change the refractive index of the host component in the nanocomposite. Nanocomposites are also found in nature, one common example being bone (see Figure 1.8a).[17] These composites differ from the conventional composite material because of exceptionally high surface to volume ratio, the area of interface between matrix and reinforcement phase being an order of magnitude greater than conventional ones. This enables a very small quantity (0.5% to 5%) of nanoscale reinforcement to show an observable effect. For example, adding carbon nanotubes enhances electrical and thermal conductivity. The second type of 3D nanomaterials are nano-crystallites which are single-phase or multiphase polycrystalline materials with crystallite size below 100 nm, so that ~50% of the material consists of grain boundaries (see Figure 1.8b).[18] These materials are different from the two solid-state structures: crystalline state with long-range order and glassy state with short-range order and hence may be utilized technologically. 3D nanomaterials can also exist as films called nanostructured films which may be up to several micrometers thick but contains a large concentration of nanoscale features such as dislocations, grain boundaries, defects, twinning etc, homogeneously distributed throughout the film (see Figure 1.8d).[22] Even a surface can be 3D nanomaterial if it is covered with nano-sized structures, called nanotextured surface which is superamphiphobic, repelling water,

ice, oil and microorganisms (see Figure 1.8c).[23] They are also termed as smart surfaces because of its antireflectivity and transparency.
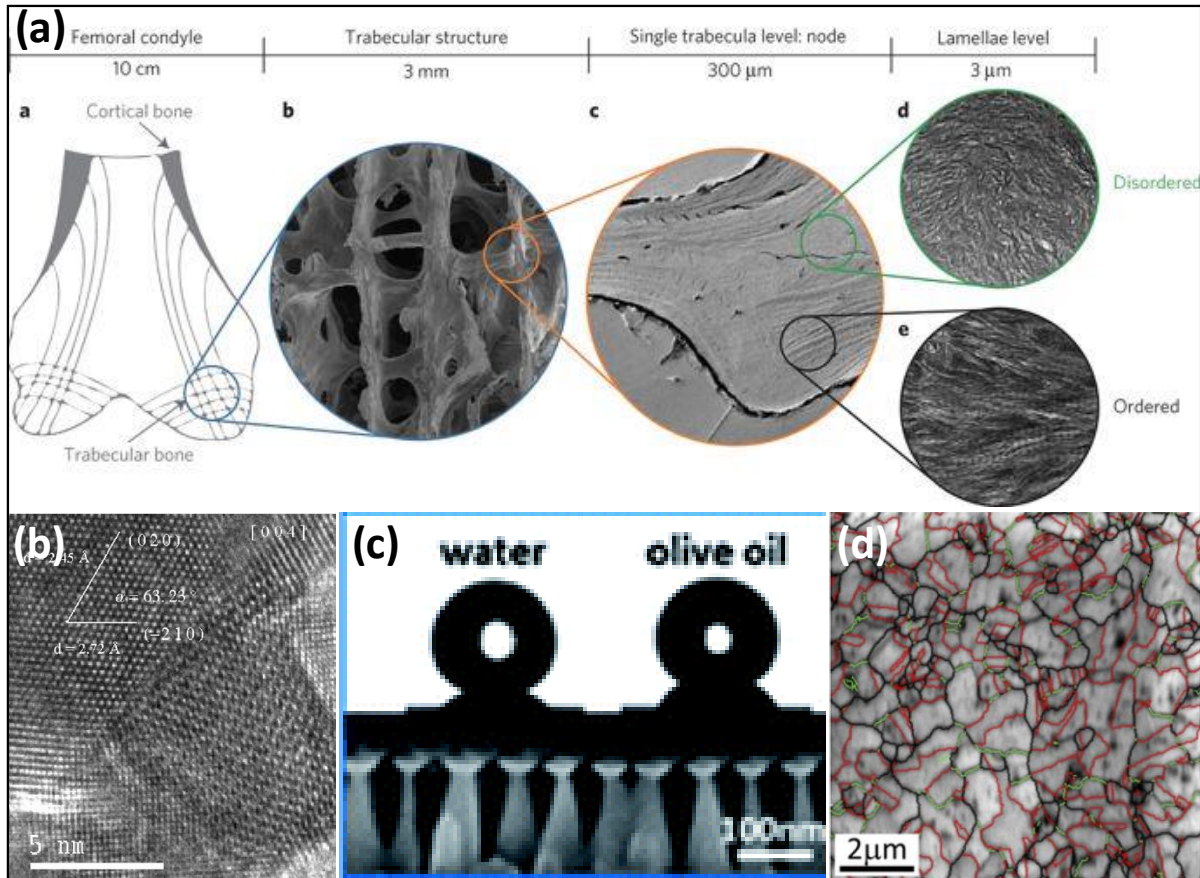
Figure 1.8 Examples of 3D nanomaterials. (a) microscopy of bone structure,[19] (b) TEM of copper nanocrytallites,[20] (c) amphiphobic nanotextured film[21] and (d) grain boundary distributions on nanostructured top surface of ultrafine grained copper.[22]

The following paragraphs discuss a few examples of nanomaterials of different dimensionalities that are relevant to this thesis:

1.2.1 2D materials: Graphene

Graphene is one of the allotropes of carbon where all the carbon atoms are sp^2 hybridised to form a planar sheet of carbon atoms. It has hexagonal lattice where one

atom forms each vertex. It is like an infinite flat aromatic molecule where every benzene ring has six adjacent benzene rings (see Figure 1.9a). It is also considered the basic building block of the common allotropes of carbon because it can be wrapped to form 0D fullerenes (see Figure 1.9b), can be rolled to form 1D carbon nanotubes (see Figure 1.9c) and can be stacked to form 3D graphite (see Figure 1.9d).[24] Owing to its long-range π conjugation, it has excellent electrical and thermal conductivity. In proportion to its thickness, it is 100 times stronger than steel (intrinsic strength of 130 GPa). The field received enormous interest when Geim and co-workers at Manchester University first isolated single layer of graphene in 2014, because two-dimensional crystals were thought to be thermodynamically unstable. A large amount of interesting physics in graphene was discovered after this experimental isolation such as ambipolar field effect, quantum hall effect at room temperature, as reinforcing agent in a polymer matrix,[25] high young's modulus (1 TPa), high optical transmittance, barrier and flame retardant due to zero band gaps and so on.

Electronic properties of Graphene: Graphene is a semi-metal with zero band-gap because its conduction bands and valence bands meet at the Dirac points which are located at the six vertices of the hexagon in the momentum space. As shown in Figure 1.10, there are two non-equivalent sets of three points on the edge of the Brillouin zone denoted by K and K'. In the vicinity of the K-points, the energy depends linearly on the wave vector, similar to relativistic particle. Since graphene lattice has a basis of two atoms, the electrons can be described by an equation that is formally equivalent to the massless Dirac equation. Hence, the electrons and holes are called Dirac fermions. This gives

graphene its remarkable electron mobility of ~15000 cm²V⁻¹s⁻¹ and electrical resistivity of 10^{-6} Ωcm, at room temperature.
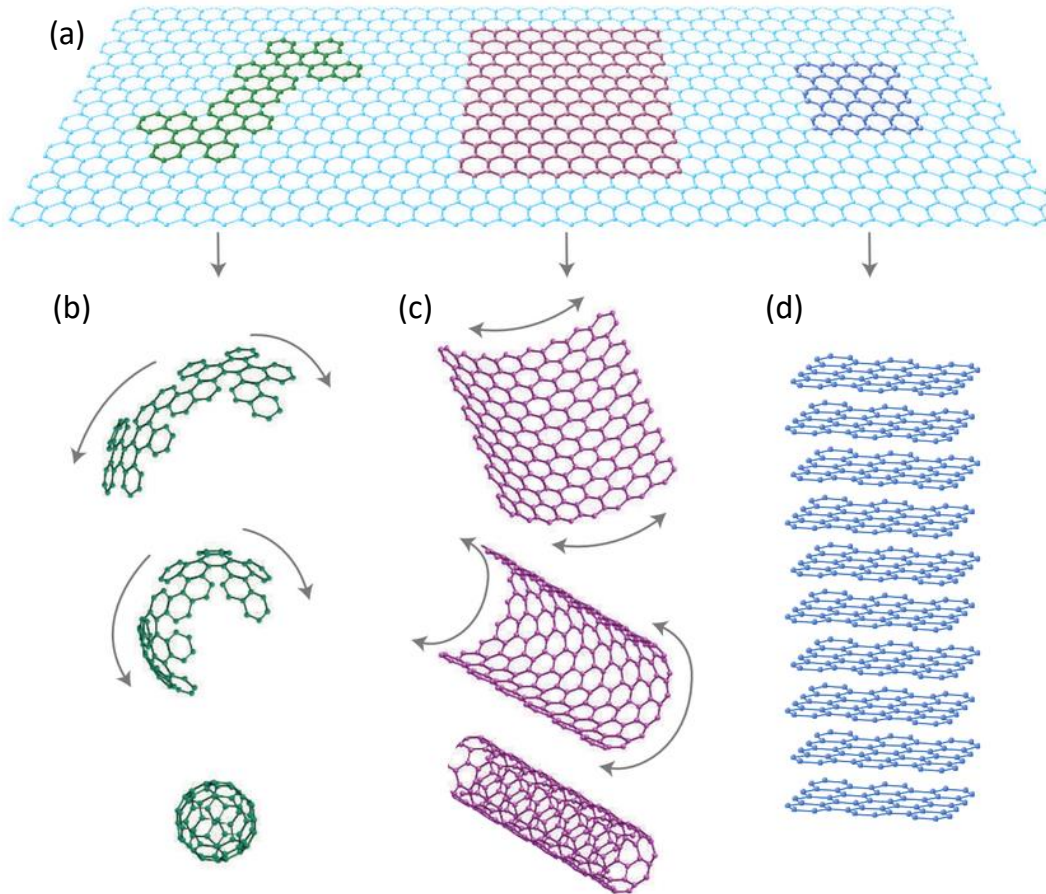
Figure 1.9 Allotropes of carbon derived from graphene. (a) Graphene having hexagonal planar lattice with each vertex as carbon atom. Schematic representation of how it can be stacked to form (b) graphite, rolled to form (c) carbon nanotube and can be wrapped to form (d) fullerene. Reproduced with permission.[26]

Thermal properties: Graphene can exhibit two types of thermal conductivities, in-plane and inter-planar. The repeating structure of graphene makes it an ideal material to conduct heat in-plane. For Interplanar conductivity, other nanomaterials such as CNTs are added.
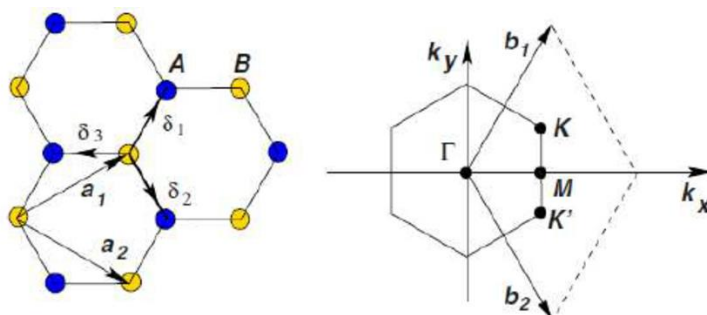
Figure 1.10 Honeycomb lattice of graphene and its first Brillouin zone.[27]

The regular structure allows the movement of phonons through the material without impediment at any point along the surface. The in-plane conductivity of a single-layered sheet is 3000-5000 $Wm^{-1}K^{-1}$, but the cross-plane conductivity can be as low as 6 $Wm^{-1}K^{-1}$, due to the weak inter-planar van der Waals forces.[28] The specific heat capacity of the electronic gas in graphene has been estimated to be around 2.6 $\mu Jg^{-1}K^{-1}$ at 5 K. Because of graphene's ability to dissipate heat, it can be used in electronics. Other potential uses include thermal interface materials, heat spreaders, thermal greases, nanocomposites etc.

Flexibility: The repeating sp^2 hybridized backbone of graphene gives it, its flexibility, as there is rotation around some of the bonds, still providing enough rigidity and stability that it can withstand changes in conformation and support other ions. This is a very desirable property as there are not many molecules that can be flexible and supportive at the same time. In terms of its elasticity, graphene has found to have a spring constant between 1-5 Nm^{-1}, with Young's modulus of 0.5 TPa.[29] What makes it particularly special is that graphene also contains elastic properties, being able to retrace to its initial size after releasing strain. Its flexibility could be used in emerging technologies such as rollerball computers, heat sensitive clothing and flexible phones.[30]
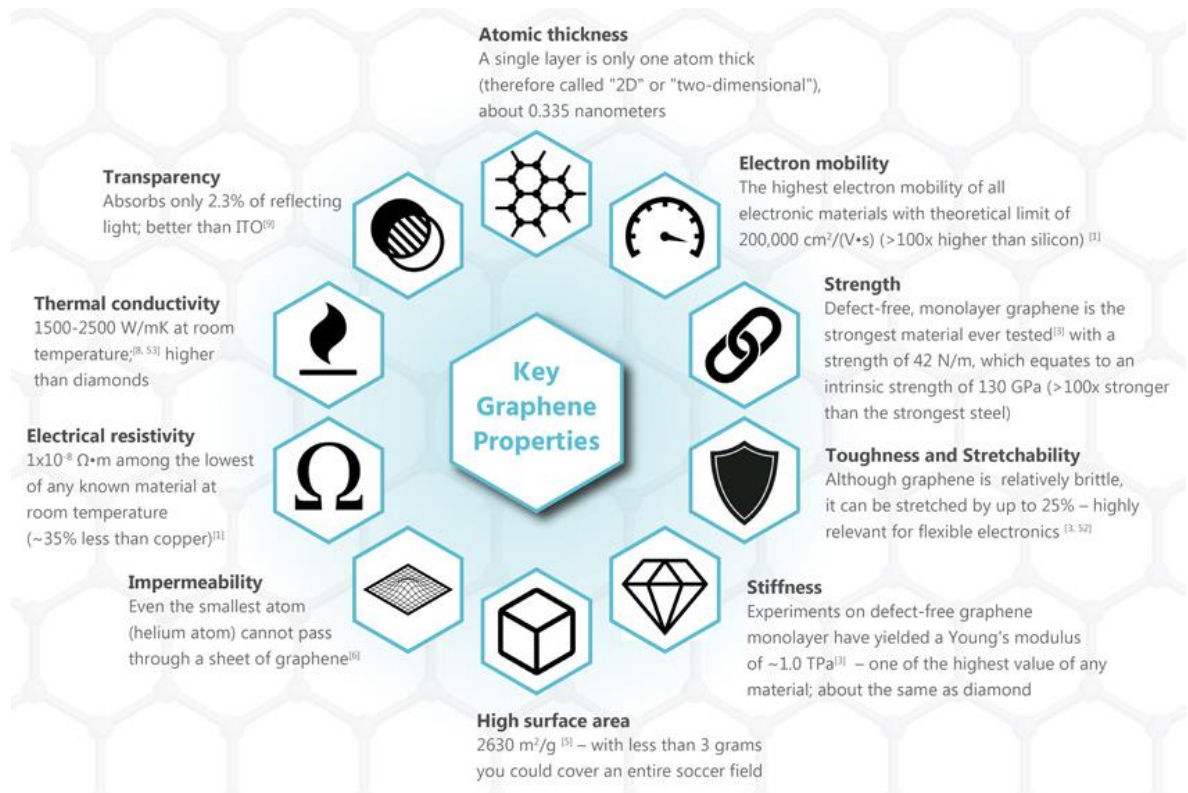
Figure 1.11 Key properties of graphene.[31]

Mechanical Strength: One more property of graphene that stands out is its inherent strength. Lee et. al. measured the mechanical properties of free-standing monolayer graphene by using nanoindentation in an AFM and established graphene as "the strongest material ever measured", in their words.[32] Due to the strength of its 0.142 nm-long carbon bonds, graphene is the strongest material ever discovered, with an ultimate tensile strength of 130 GPa compared to 0.4 GPa for A36 structural steel. Not only is graphene extraordinarily strong, it is also very light at 0.77 mg/m^2 (for comparison purposes, 1 square metre of paper is roughly 1000 times heavier). Interestingly, a single sheet of graphene, being only 1 atom thick, enough in size enough to cover a whole football field, would weigh under 1 gram.

Optical Properties: Graphene's ability to absorb 2.3% of white light is also a unique and interesting property, especially considering that it is only 1 atom thick. This is due to its electronic properties; the electrons acting like massless charge carriers with very high mobility. A few years ago, it was proved that the amount of white light absorbed is based on the fine structure constant. Adding another layer of graphene increases the amount of white light absorbed by approximately the same value (2.3%). Therefore, 97.7% of light passes through a single layer, with ~0.1% reflected from its initial trajectory. However, the more graphene layers there are stacked on top of each other, the greater the light absorption becomes and the optical transparency decreases linearly, meaning that a graphene sample composed of 5 layers would have absorption of 11.5% and optical transparency of around 88% - 88.5%. Graphene possesses unique optical transitions and can absorb light over a wide range of frequencies. The ability for graphene to absorb radiation from many different regions in the electromagnetic spectrum is down to its band structure, lack of a band-gap and the interaction between the electromagnetic radiation and the Dirac fermions in the graphene sheet. Graphene can also produce optical transitions in electric fields, and this is known as gate-dependent optical transitions. Under an applied electrical field, low density of states near the Dirac point causes the Fermi level of the graphene to shift. It is a process often used in electronics to modulate the current, as a change in the Fermi level changes the conductivity, as well as for tuning the transmission of an optical source. Graphene can also emit some form of photoluminescence.[33] Pristine graphene is known to emit light when it has been excited by a near-infrared laser. The mechanism of light emittance is

due to high temperature of femtosecond laser photons which hit the graphene sheet, as they are known to emit in the visible light spectrum.

In terms of how much the true properties of graphene are understood, this is just the tip of the iceberg. It is believed that graphene can excel at becoming primary material to be integrated into electronics which makes it worthwhile to understand what makes it such an amazing material. While a lot of imagination in coming up with new ideas for potential applications and uses of graphene, it takes time to fully appreciate how and what graphene is, to develop these ideas into reality. Exploring the practical aspect, various forms in which graphene exists, have been explained below.

Graphite: This is a crystalline form of the elemental carbon occurring naturally in nature. It contains a lot of domains of multilayer graphene where each layer has a weak van der Waal bond among them. It is a three-dimensional material. It conducts electricity due to the vast delocalisation of π electrons. It also acts a great lubricant as the graphene layers can slip over each other due to week interaction. One of the common examples of presence of graphite is in the lead of pencils. Another type of multilayer graphene is Highly Oriented Pyrolytic Graphene (HOPG) which is synthetically produced. It has an angular spread of less than 1° between the graphene sheets.

Few-layer graphene: When multilayer graphene has less ten layers, it is called as few-layer graphene, a 3D nanomaterial. It is mostly prepared by intercalation exfoliation of expanded graphite in sulphuric acid. These stacked few layers hold promise of using as a substitute for indium tin oxide as a transparent conducting electrode.

Graphene oxide: It is a compound of carbon, hydrogen and oxygen in variable ratios made by treating graphite with strong oxidising agents. In 1957, Hummers and Offeman developed an efficient method of its preparation using a mixture of sulphuric acid, sodium nitrate and potassium permanganate.[34] It typically preserves the layer structure
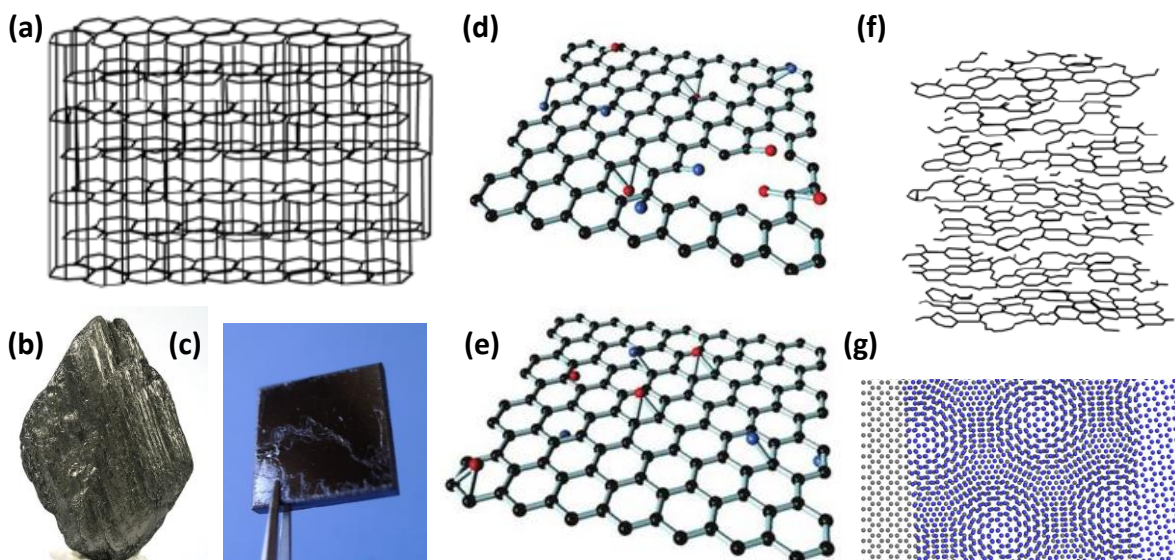
Figure 1.12 Graphene like materials. (a) 3D graphite, (b) naturally occurring graphite, (c) highly oriented pyrolytic graphene, (d) graphene oxide, (e) reduced graphene oxide, (f) turbostratic graphite and (g) twisted bilayer graphene.

of parent graphite, but the layers are buckled and the interlayer spacing is two times larger (0.7 nm) than that of graphite. The oxygenated functionalities make it hydrophilic which allows its exfoliation in water through sonication. This eventually produces monolayer or few-layer oxygen functionalised graphene, called graphene oxide. The presence of oxygen functional groups allows its easy dispersion in organic solvents, water and different matrixes. This is a major benefit when combining the material with polymer or ceramic matrixes to enhance their mechanical and electrical properties. Graphene oxide functions as an electrical insulator, because of the

disturbance of its sp^2 bonding networks. It has been shown that it is possible to attach fullerene-functionalized secondary amines and porphyrin-functionalized primary amines to graphene oxide platelets, to enhance the nonlinear optical performance of the material.

Reduced graphene oxide: It is effectively graphene which is produced by reducing the graphene oxide using hydrazine hydrate, hydrogen plasma, or by heating. This is a scalable way of producing graphene. Unfortunately, the reduction process damages the structure of the graphene creating imperfections and vacancies.

Turbostratic graphite: This is a type of graphite in which there is quenched rotational misalignment between adjacent graphene sheets, *i.e.* one sheet is rotated with respect to its neighbour. Because of this, the interaction between the layers is very week and the interlayer spacing (>0.342) is larger than that for crystalline graphite (0.335).[35] This kind of graphite is produced when carbon materials are produced at low temperatures, below 1300°C. However, there is a huge number of defects in the system.

Twisted bilayer graphene: When one of the stacking layers gets twisted with a certain angle relative to the other, so-called twisted bilayer graphene (tBLG) is formed, which has been proved to have unique electrical properties, optical properties, chemical properties and phonon thermal properties. One intriguing property is the emergence of a flat band in a small twist angle leading to superconducting state.[36]

Graphene nanoribbon: Graphene nanoribbons (GNRs) are strips of graphene having width of less than 50 nm. As graphene width decreases, both quantum confinement and edge effects become pronounced. There are various ways of producing it. One way is

applying sharp diamond knife on graphite to create nanoblocks, followed by exfoliation.[37] They can also be produced by unzipping or axially cutting nanotube.[38] They are also grown on the edges of three-dimensional structures etched into SiC wafers. The very high mobility, gate voltage-controlled electron or hole carriers, and tuneable bandgap, suggest that GNRs may be ideal for nanoscale electronics and have triggered immense interest in the large-scale synthesis of GNRs.[39]

1.2.2 1D nanomaterials: nanowires, carbon nanotubes

One-dimensional (1D) nanostructured materials, including nanotubes, nanofibers, and nanowires, have attracted much attention due to their interesting properties and wide range of potential applications. 1D materials are generally considered to be high-capacity and stable electrode materials, due to their uniform structure, orientated electronic and ionic transport, and strong tolerance to stress change. The networks of these 1D nanomaterials such as Ag nanowires and carbon nanotubes have been used as transparent conducting electrode.

Nanowires: A nanowire is a nanostructure having the ratio of its length to width greater than 1000. Nanowires have many interesting properties that are not seen in bulk or 3D materials. This is because electrons in nanowires are quantum confined laterally and thus occupy energy levels that are different from the energy bands found in bulk materials. The synthesis involves top-down approach involving lithography, milling or thermal oxidation and bottom-up approach involving combining constituent adatoms or growing nanowires in solution. Nanowires can be conducting (Ni, Pt, Au), semiconducting (Si, Ga, In), insulating (SiO_2, TiO_2), superconducting (Yttrium barium

copper oxide) and even molecular where molecules such as DNA occur in repeated units. For industrial applications, metal nanowires are used for welding wires as small as 10 nm.[40] Due to the unique one-dimensional structure with remarkable optical properties, the nanowires also open new opportunities for realising high-efficiency photovoltaic devices.[41] When silicon wafers of lower purity are used with nanowires, the efficiency improves considerably leading to the reduction on material consumption.[42] Ink-based films comprised of conductive percolation networks of Ag NWs with high aspect ratios are particularly promising, because they report exceptional transparency and conductivity that can surpass even ITO based TCEs. One useful application of the nanowires can also be for making MOS transistors, which are the building blocks of most of the electronics today. According to Moore's law, the transistors are becoming smaller and smaller in size, the challenge is ensuring a good gate control over the channel. The high-aspect ratio of these nanowires can be put to great use by making the channel with a nanowire, surrounded by a gate dielectric. This will lead to an efficient on-off by giving a good control of electrostatic potential.

Carbon nanotubes: Carbon nanotubes (CNTs) are tubes made up of sp^2 hybridised carbon, having a diameter in nanometers. Individual nanotubes align themselves into rope-like structure by van de Waals forces. It is possible to prepare metre long nanotubes with an aspect ratio of more than 100,000,000:1 and the smallest length is that of an organic compound, cycloparaphenylene. Most of the times, the aspect ratio is very high, and the length is often assumed to be infinite. Just like graphene (see Figure 1.13a), CNTs do not have usual x and y axes. Instead, they have armchair and zigzag axes as shown in Figure

1.13b and c, according to the direction of their curvature. However, these are not the only configurations that a CNT can have. If you cut open a CNT parallel to its axis into a rectangle and you find that its mirror image cannot be superimposed, then it's a chiral nanotube (see Figure 1.13d). It is possible to join two CNTs or join graphene with CNT to form heterojunctions as has seen studied theoretically[43] and experimentally.[44] These junctions can form the basis of pillared graphene and other 3D architectures, which can lead to development of all-carbon electronics. These are the strongest and stiffest materials. Since their density is very low for a solid, 1.3 to 1.4 gcm^{-3}, their specific strength, 48000 $kNmkg^{-1}$, is the best of known materials. They can be either metal, quasi-metal or semiconducting but not semi-metal, because the Dirac point is slightly shifted from K point in the Brillouin zone, owing to the curvature of the tube surface. Techniques that are used to produce CNTs in large quantities are laser ablation, arc discharge, chemical vapour deposition and high-pressure carbon monoxide disproportionation. Transparent conducting electrodes are also based on continuous films of pure single walled carbon nanotubes (SWNTs). These intrinsic electrical conductors are formed into uniform, optically homogeneous films of controllable thickness that are thin enough to be transparent over technologically relevant regions of the electromagnetic spectrum.[45]

1.2.3 Mixed dimensionality systems: nanowire networks, metal grids, metal mesh

A purely 2D material can be thought of being formed by infinite 1D units placed next to each other without any gaps. However, a surface formed by 1D units arranged in a certain fashion, not allowing filling up of all the space, is not a purely 2D material,

despite appearing like one. In terms of fractals, a material is supposed to have a fractal dimension between 1-2 if the structure is too complex to be called as 1D and is too simple to be called as 2D. Similarly, if a structure is too complex to be called a 0D and is too simple to be called a 1D, it has a fractal dimension between 0 and 1. To calculate the fractal dimension of a pattern, it is divided into several boxes and then it is seen for each box whether or not it contains any pixels of the pattern. Examples of networks having fractal dimensions between 1 and 2 are CNT networks, AgNW networks, metal mesh, metal grids, etc.
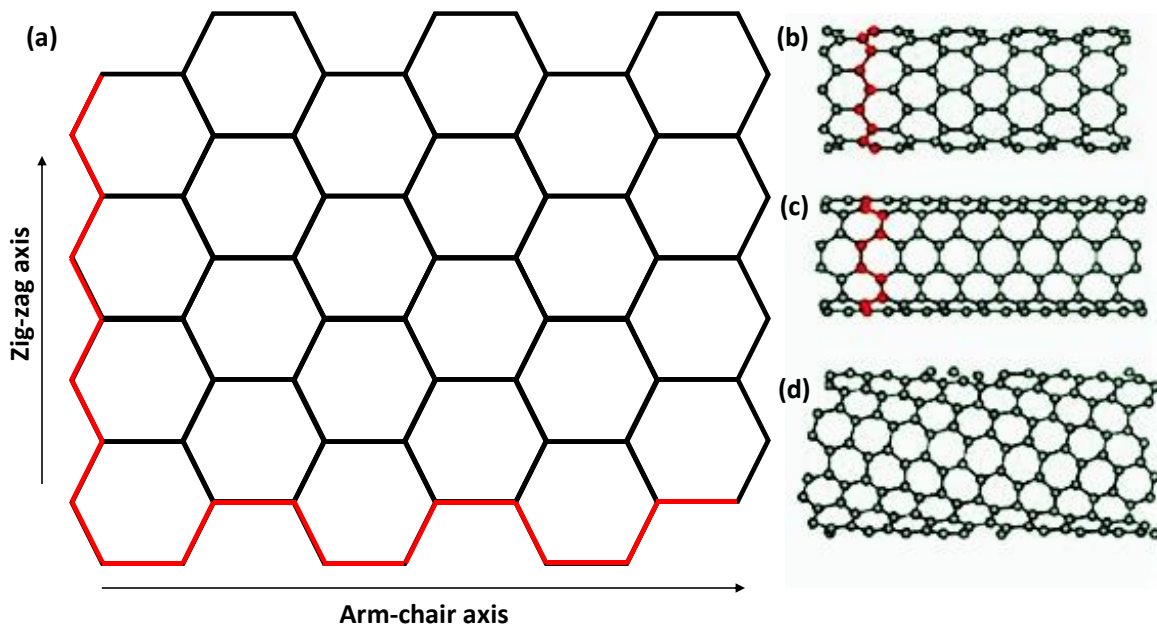
Figure 1.13 Carbon nanotube configurations. (a) Zigzag and armchair axes marked in graphene lattice, which is thought to roll up into carbon nanotubes of different configurations. Schematic of carbon nanotubes in (b) zigzag, (c) armchair and (d) chiral configurations. (Image source: Google images)

Metal nanowire network: Networks of metal nanowires have the potential to meet the needs of next-generation device technologies that require flexible transparent conductors. The most used material for transparent conducting applications is Indium Tin Oxide (ITO) which suffers from scarcity of raw material, brittleness and high cost.[46] Metal nanowire networks can not only match the electro-optical performance of ITO but also fulfil the emerging demands for flexible devices such as solar cells, touch screens, displays, wearables etc[47] where the most promising ones are Ag and Cu nanowires based networks. Their main properties include transparency, electrical resistance and bending ability. Very small diameters of the nanowires may lead to high electrical resistance and too large may lead to increase in shadowing effect, dropping the transparency. Thus, a trade off needs to be found. The junctions also play a key role, by increasing the resistance and the roughness of the film. There are some real-world challenges including nanowire length distribution, non-isotropic orientation and curvature which affect the nanowire film formation. Various physical mechanisms such as diffusion of metal atoms over a long period of time, electromigration process during electrical stress or oxidation of the metal in presence of humidity or high temperature condition, limit the stability of these films. Also, mild scratching or mechanical stress may detach the nanowires from the transparent substrate. In order to prevent such instability, encapsulation is performed by thin oxide layers. The additional steps of annealing or encapsulating make this process of achieving transparent conducting electrode quite complicated.
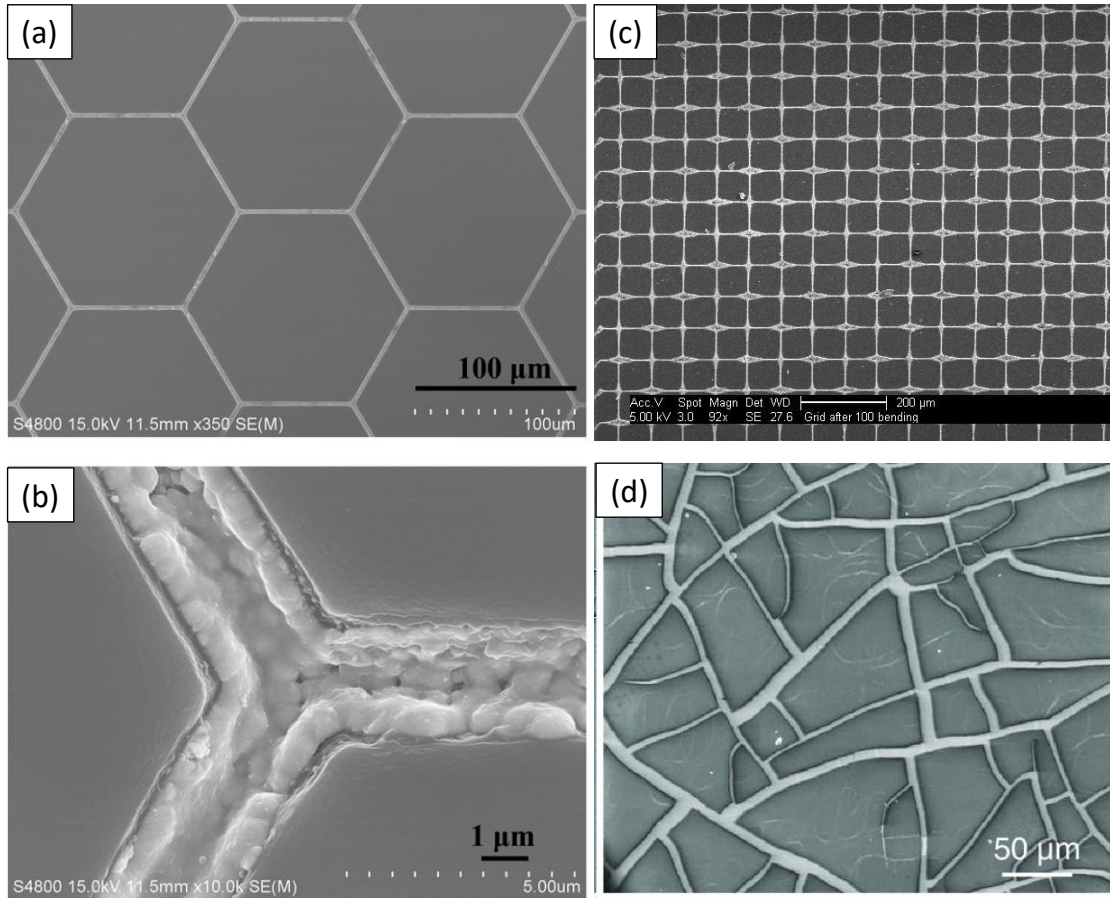
Figure 1.14 SEM images of different types of metal meshes. Hexagonal metal mesh shown in (a) low and (b) high magnification.[48] (c) grid type metal mesh[49] and (d) crackle metal mesh.[50] Reproduced with permission.

Metal grids: These are the films where the metal is deposited by photolithography, laser sintering or direct writing, in a periodic pattern such as hexagonal (see Figure 1.14a and b), squarish (see Figure 1.14c), triangular, brick-walls, pyramids, circular etc.[51] The deposition of the grid need not have a mask always, and the transmittance and electrical conductivity may be changed by changing the design of the grid by modifying the computer-aided design data.[52] Transparent electrodes can be easily prepared using these grids on polymer or glass substrates without using any high temperature or vacuum environment.

Metal mesh: Also called metal wire network, metal mesh refers to very thin interconnected metal networks with or without a transparent substrate. They have been prepared by depositing metal in templates such as hierarchical patterns of random cracks (see Figure 1.14d), grain boundaries or leaf venations. As they have a template, the conductivity of the mesh can be improved by depositing metal for longer duration to increase the height of the mesh, without compromising on the transparency. These metal mesh electrodes can be prepared on rigid/flexible substrates using different fabrication techniques including sputtering, thermal evaporation, laser direct writing, electrodeposition, lithographic patterning/imprinting, printing, or a combination of two techniques for hybrid electrodes. The structure of a metal mesh usually gives rough surface to overcome which researchers have attempted to passivate it by depositing a conductive layer such as zinc oxide or they have encapsulated the entire TCE in a polymer.[50] This transparent conductor is almost similar to the metal grids, except that the patterns are random instead of periodic. Therefore, the light interference occurring when incident light is closer in wavelength to the period length for a periodic grid structure, can be avoided.

1.3 Applications of graphene

1.3.1 Graphene composites: Composites are materials formed by combining two or more materials with different properties to produce an end material with unique characteristics. These materials do not dissolve together but remain distinct within the final composite structure. Composite materials can be made to be stronger, lighter, or more durable than traditional materials due to properties they gain from combining

their different components. Graphene's presence can enhance the conductivity and strength of bulk materials and help create composites with superior qualities. Graphene can also be added to metals, polymers and ceramics to create composites that are conductive and resistant to heat and pressure. To be able to harness these properties, graphene sheets should be produced on a sufficient scale, then incorporated and homogeneously distributed into various matrices. Song et. al reported outstanding thermal conductivity ($\sim$1.53 Wm^{-1}K^{-1}) and mechanical properties ($\sim$1.03 GPa) by dispersing non-oxidised graphene flakes with non-covalent functionalisation of 1-pyrenebutyric acid.[53] Graphene as nanofiller is very promising owing to its high surface area, aspect ratio, tensile strength, thermal conductivity and electrical conductivity, EMI shielding ability, flexibility and transparency.

1.3.2 Electronics: Li et. al. have developed a graphene foam-based battery design to bridge the gap between batteries and capacitors, which can charge as fast as a capacitor and can discharge in 20 s.[54] Yao et. al. have developed two-terminal transparent flexible memory device using graphene.[55] After the initial large current creates the nanochannels, smaller charges can then be used to break or make the circuit to encode binary information and a still smaller current can be used to check the state of the memory without charging it. In 2008, Das et. al. reported a top-gated graphene transistor.[56] Presently, highly critical issues with the extensive use of graphene in electronics are related to manufacturing. Although growth on copper surfaces has made bulk manufacture of a large area graphene layer possible, there are a number of

technical challenges to be overcome, both in terms of cost and quality before the first consumer products using graphene can be commercialised.[57]

1.3.3 Hydrogen evolution: Hydrogen energy is considered as the most powerful candidate to alternate fossil energy due to its clean, renewable, and environmentally friendly properties and high energy density.[58] Pure flat graphene is catalytically inert in hydrogen evolution reaction (HER). Mo-doped graphene is reported to exhibit excellent catalytic ability in HER.[59] The curvature also plays a vital role to improve the HER activity of graphene.[60] Kumataki *et. al.* have produced nanometric sized holey graphene which in acid conditions outperforms an electrode using regular non-holey graphene.[61]

1.4 Applications of metal mesh electrodes

1.4.1 Transparent conducting electrodes: Transparent conducting films are thin films of optically transparent and electrically conductive material. Randomly conducting networks of wires or metal meshes obtained from templates are new generation transparent electrodes, which are easy to produce and are cost-effective (more details have been mentioned in section 1.2.3). They can be either used as stand-alone transparent conductors or as a component in a device. Ag-based mesh electrodes have been demonstrated which are stable under bending and sonication tests. On further coating with Cu, the meshes were found to be stable in ambient atmosphere for more than a year.[62] Metal meshes based on cracked TiO_2 templates have been utilised for touchscreen applications.

1.4.2 Optoelectronic devices: Metal mesh inherently possesses high electrical conductivity, optical transparency, mechanical robustness, and a low fabrication cost due to which they become the best candidates for optoelectronic devices. They also give rise to interesting features such as inducing additional light scattering due to the presence of nanoparticles in the mesh,[63] can be made flexible thus serving a good candidate for making organic LEDs,[64] offers strong adhesion and conformity with the substrate[65] and can withstand harsh chemical and environmental conditions.[66] These qualities make them advantageous to be utilised for photovoltaics, OLED, supercapacitors and electrochromic devices.[51] Ag metal mesh has been used as a substitute for ITO in a thin film organic solar cell having comparable performance and good scalability.[67] Pd based meshes have been demonstrated to show hydrogen sensing at a concentration as low as 0.02% in 13 s.[68] Au wire network-based electrode has been used to fabricate transparent and flexible capacitors of 20 μF cm^{-2} at 1 Hz with average transmittance of ~68%. A flexible capacitive touch panel has been demonstrated to detect multiple stimuli involving pressure touch (up to 180 kPa) and temperature sensing (<50 °C).[69] By sandwiching a laser ablated ZnO film between two Au wire networks, UV photodetectors have been fabricated which show a sensitivity of 630%, detectivity of ~10^{10} Jones and responsivity of ~10^{-2} AW^{-1}.[50] Electrochromic supercapacitors using Au metal mesh has been demonstrated to have excellent capacitance (~15 mFcm^{-2}) which can change colour from green to blue with charging.[70]

1.4.3 Opto-electrical devices: When current is passed through a metal mesh, applying a few volts, it becomes a transparent heater, having applications in making

defrosting and de-icing windows typically used for various optoelectrical appliances such as advertisement boards, liquid crystal displays, avionics displays etc. Transparent heaters are more efficient compared to hydrophobic coatings for defrosting or anti-icing, especially in harsh weather conditions. Metal mesh provides uniform heating with a variation of only ~3 °C without any hotspots, at the same being cost-effective.[71] As these meshes are aperiodic, they are easily able to avoid optical diffraction, hindering visibility at certain angles. These meshes exhibit sheet resistances as low as ~6 $\Omega\square^{-1}$ at transmittance of 86% and raise the temperature to 93 °C with an input voltage of only ~5 V with fast response (< 20 s).[72]

1.4 Scope of the thesis

The present thesis is divided into two parts namely metal mesh electrodes and twisted graphene. The first part of the thesis deals with junction-less metal mesh fabricated by crackle lithography. The application of this metal mesh for solar cell front electrodes is demonstrated for the first time, detailing how these electrodes serve better than the conventional ones in terms of fabrication process and costs. The electrodes themselves serve as highly sensitive strain sensors using a polymer base which pave a way for usage in electronic skin. The graphene literature talks about single-layer graphene, bernal stacked graphene where the graphene layers are stacked in AB configuration (most stable form thermodynamically), twisted bilayer graphene where layers are intentionally placed twisted with respect to each other using manipulators, and turbostratic graphene where the graphene layers are inherently twisted but has a high density of defects. In the present work, a new form of graphene is being discussed which is multi-layered, has inherent twists among its layers and still, has no defects. What makes this type of graphene stand out, is being discussed along with its possible applications.

√

1.5 References

(1)   Buzea, C.; Pacheco, I. I.; Robbie, K. Nanomaterials and Nanoparticles: Sources and Toxicity. *Biointerphases***2007**, *2* (4), MR17–MR71.

(2)   Portela, C. M.; Vidyasagar, A.; Krödel, S.; Weissenbach, T.; Yee, D. W.; Greer, J. R.; Kochmann, D. M. Extreme Mechanical Resilience of Self-Assembled Nanolabyrinthine Materials. *Proc. Natl. Acad. Sci.***2020**, 201916817.

(3)   Wei, G.; Bhushan, B.; Torgerson, P. M. Nanomechanical Characterization of Human Hair Using Nanoindentation and SEM. *Ultramicroscopy***2005**, *105* (1), 248–266.

(4)   Hortolà, P. Sem Analysis of Red Blood Cells in Aged Human Bloodstains. *Forensic Sci. Int.***1992**, 55 (2), 139–159.

(5)   Marini, M.; Falqui, A.; Moretti, M.; Limongi, T.; Allione, M.; Genovese, A.; Lopatin, S.; Tirinato, L.; Das, G.; Torre, B.; et al. The Structure of DNA by Direct Imaging. *Sci. Adv.***2015**, *1* (7), e1500734.

(6)   Clayton, C. R. Materials Science and Engineering: An Introduction. *Mater. Sci. Eng.***1987**.

(7)   Boholm, M.; Arvidsson, R. A Definition Framework for the Terms Nanomaterial and Nanoparticle. *Nanoethics***2016**, *10* (1), 25–40.

(8)   Huffaker, D. L.; Park, G.; Zou, Z.; Shchekin, O. B.; Deppe, D. G. 1.3 Mm Room-Temperature GaAs-Based Quantum-Dot Laser. *Appl. Phys. Lett.***1998**, *73* (18), 2564–2566.

(9)   Semonin, O. E.; Luther, J. M.; Choi, S.; Chen, H.-Y.; Gao, J.; Nozik, A. J.; Beard, M. C. Peak External Photocurrent Quantum Efficiency Exceeding 100% via MEG in a Quantum Dot Solar Cell. *Science***2011**, *334* (6062), 1530–1533.

(10)   Kim, T.-H.; Cho, K.-S.; Lee, E. K.; Lee, S. J.; Chae, J.; Kim, J. W.; Kim, D. H.; Kwon, J.-Y.; Amaratunga, G.; Lee, S. Y.; et al. Full-Colour Quantum Dot Displays Fabricated by Transfer Printing. *Nat. Photonics***2011**, *5* (3), 176–182.

(11)   Xu, Y.-F.; Yang, M.-Z.; Chen, B.-X.; Wang, X.-D.; Chen, H.-Y.; Kuang, D.-B.; Su, C.-Y. A CsPbBr3 Perovskite Quantum Dot/Graphene Oxide Composite for Photocatalytic CO_2 Reduction. *J. Am. Chem. Soc.***2017**, *139* (16), 5660–5663.

(12)   Zhao, B.; Ran, R.; Liu, M.; Shao, Z. A Comprehensive Review of Li4Ti5O12-Based Electrodes for Lithium-Ion Batteries: The Latest Advancements and Future Perspectives. *Mater. Sci. Eng. R Reports***2015**, *98*, 1–71.

(13)   Jin, T.; Han, Q.; Wang, Y.; Jiao, L. 1D Nanomaterials: Design, Synthesis, and Applications in Sodium–Ion Batteries. *Small***2018**, *14* (2), 1703086.

(14)   Yang, Y.; Chen, Y.; Wu, Y.; Chen, X.; Kong, M. Diameter-Controllable Magnetic Properties of Co Nanowire Arrays by Pulsed Electrodeposition. *J. Nanomater.***2010**, *2010*, 793854.

(15)   Novoselov, K. S.; Geim, A. K.; Morozov, S. V; Jiang, D.; Zhang, Y.; Dubonos, S. V; Grigorieva, I. V; Firsov, A. A. Electric Field Effect in Atomically Thin Carbon Films. *Science***2004**, *306* (5696), 666–669.

(16)   Lin, Y.; Connell, J. W. Advances in 2D Boron Nitride Nanostructures: Nanosheets, Nanoribbons, Nanomeshes, and Hybrids with Graphene. *Nanoscale***2012**, *4* (22),

6908–6939.

(17) He, W.-X; Rajasekharan, A. K.; Tehrani-Bagha, A.R.; Andersoon, M. Mesoscopically Ordered Bone Mimetic Nanocomposites. *Front. Bioeng. Biotechnol.***2015**, 27(13),2260-2264.

(18) Birringer, R. Nanocrystalline Materials. *Mater. Sci. Eng. A***1989**, *117*, 33–43.

(19) Tertuliano, O. A.; Greer, J. R. The Nanocomposite Nature of Bone Drives Its Strength and Damage Resistance. *Nat. Mater.***2016**, *15* (11), 1195–1202.

(20) Lu, L.; Sui, M. L.; Lu, K. Superplastic Extensibility of Nanocrystalline Copper at Room Temperature. *Science***2000**, *287* (5457), 1463–1466.

(21) Telecka, A.; Li, T.; Ndoni, S.; Taboryski, R. Nanotextured Si Surfaces Derived from Block-Copolymer Self-Assembly with Superhydrophobic, Superhydrophilic, or Superamphiphobic Properties. *RSC Adv.***2018**, *8* (8), 4204–4213.

(22) Zhao, Y.; Furnish, T. A.; Kassner, M. E.; Hodge, A. M. Thermal Stability of Highly Nanotwinned Copper: The Role of Grain Boundaries and Texture. *J. Mater. Res.***2012**, *27* (24), 3049–3057.

(23) Chelliah, C. R. A. J.; Swaminathan, R. Pulsed Laser Deposited Hexagonal Wurzite ZnO Thin-Film Nanostructures/Nanotextures for Nanophotonics Applications. *J. Nanophotonics***2018**, *12* (1), 1–10.

(24) Allen, M. J.; Tung, V. C.; Kaner, R. B. Honeycomb Carbon: A Review of Graphene. *Chem. Rev.***2010**, *110* (1), 132–145.

(25) Mohan, V. B.; Lau, K.; Hui, D.; Bhattacharyya, D. Graphene-Based Materials and Their Composites: A Review on Production, Applications and Product

Limitations. *Compos. Part B Eng.***2018**, *142*, 200–220.

(26) Vyatskikh, A. Transparent and Conductive Hybrid Graphene/Carbon Nanotube Films, 2015.

(27) Huda, M. N. Epitaxial Growth of Lateral Graphene / Hexagonal Boron Nitride Heterostructures, 2016.

(28) Fugallo, G.; Cepellotti, A.; Paulatto, L.; Lazzeri, M.; Marzari, N.; Mauri, F. Thermal Conductivity of Graphene and Graphite: Collective Excitations and Mean Free Paths. *Nano Lett.***2014**, *14* (11), 6109–6114.

(29) Frank, I. W.; Tanenbaum, D. M.; van der Zande, A. M.; McEuen, P. L. Mechanical Properties of Suspended Graphene Sheets. *J. Vac. Sci. Technol. B Microelectron. Nanom. Struct. Process. Meas. Phenom.***2007**, *25* (6), 2558–2561.

(30) Kim, H.; Ahn, J.-H. Graphene for Flexible and Wearable Device Applications. *Carbon N. Y.***2017**, *120*, 244–257.

(31) Cooper, D. R.; D'Anjou, B.; Ghattamaneni, N.; Harack, B.; Hilke, M.; Horth, A.; Majlis, N.; Massicotte, M.; Vandsburger, L.; Whiteway, E.; et al. Experimental Review of Graphene. *ISRN Condens. Matter Phys.***2012**, *2012*, 501686.

(32) Lee, C.; Wei, X.; Kysar, J. W.; Hone, J. Measurement of the Elastic Properties and Intrinsic Strength of Monolayer Graphene. *Science***2008**, *321* (5887), 385 LP – 388.

(33) Cao, L.; Meziani, M. J.; Sahu, S.; Sun, Y.-P. Photoluminescence Properties of Graphene versus Other Carbon Nanomaterials. *Acc. Chem. Res.***2013**, *46* (1), 171–180.

(34) Hummers, W. S.; Offeman, R. E. Preparation of Graphitic Oxide. *J. Am. Chem.*

*Soc.***1958**, *80* (6), 1339.

(35)   Li, Z. Q.; Lu, C. J.; Xia, Z. P.; Zhou, Y.; Luo, Z. X-Ray Diffraction Patterns of Graphite and Turbostratic Carbon. *Carbon***2007**, *45* (8), 1686–1695.

(36)   Cao, Y.; Fatemi, V.; Fang, S.; Watanabe, K.; Taniguchi, T.; Kaxiras, E.; Jarillo-Herrero, P. Unconventional Superconductivity in Magic-Angle Graphene Superlattices. *Nature***2018**, *556*, 43.

(37)   Mohanty, N.; Moore, D.; Xu, Z.; Sreeprasad, T. S.; Nagaraja, A.; Rodriguez, A. A.; Berry, V. Nanotomy-Based Production of Transferable and Dispersible Graphene Nanostructures of Controlled Shape and Size. *Nat. Commun.***2012**, *3* (1), 844.

(38)   Kosynkin, D. V; Higginbotham, A. L.; Sinitskii, A.; Lomeda, J. R.; Dimiev, A.; Price, B. K.; Tour, J. M. Longitudinal Unzipping of Carbon Nanotubes to Form Graphene Nanoribbons. *Nature***2009**, *458* (7240), 872–876.

(39)   Li, X.; Wu, L.; Hao, L.; Fu, Y. Chapter 5 - Emerging 2D Nanomaterials for Supercapacitor Applications; Cheong, K. Y., Impellizzeri, G., Fraga, M. A. B. T.-E. M. for E. C. and S., Eds.; Elsevier, 2018; 155–183.

(40)   Peng, Y.; Cullis, T.; Inkson, B. Bottom-up Nanoconstruction by the Welding of Individual Metallic Nanoobjects Using Nanoscale Solder. *Nano Lett.***2009**, *9* (1), 91–96.

(41)   Yu, P.; Wu, J.; Liu, S.; Xiong, J.; Jagadish, C.; Wang, Z. Design and Fabrication of Silicon Nanowires towards Efficient Solar Cells. *Nano Today***2016**, *11*.

(42)   Kayes, B. M.; Atwater, H. A.; Lewis, N. S. Comparison of the Device Physics Principles of Planar and Radial P-n Junction Nanorod Solar Cells. *J. Appl.*

*Phys.***2005**, *97* (11), 114302.

(43)   Ma, K. L.; Yan, X. H.; Guo, Y. D.; Xiao, Y. Electronic Transport Properties of Junctions between Carbon Nanotubes and Graphene Nanoribbons. *Eur. Phys. J. B***2011**, *83* (4), 487–492.

(44)   Harris, P. J. F.; Suarez-Martinez, I.; Marks, N. A. The Structure of Junctions between Carbon Nanotubes and Graphene Shells. *Nanoscale***2016**, *8* (45), 18849–18854.

(45)   Wu, Z.; Chen, Z.; Du, X.; Logan, J. M.; Sippel, J.; Nikolou, M.; Kamaras, K.; Reynolds, J. R.; Tanner, D. B.; Hebard, A. F.; et al. Transparent, Conductive Carbon Nanotube Films. *Science***2004**, *305* (5688), 1273–1276.

(46)   Angmo, D.; Espinosa, N.; Krebs, F. Indium Tin Oxide-Free Polymer Solar Cells: Toward Commercial Reality BT - Low-Cost Nanomaterials: Toward Greener and More Efficient Energy Applications; Lin, Z., Wang, J., Eds.; Springer London: London, **2014**; 189–225.

(47)   Manning, H. G.; da Rocha, C. G.; Callaghan, C. O.; Ferreira, M. S.; Boland, J. J. The Electro-Optical Performance of Silver Nanowire Networks. *Sci. Rep.***2019**, *9* (1), 11550.

(48)   Chen, X.; Guo, W.; Xie, L.; Wei, C.; Zhuang, J.; Su, W.; Cui, Z. Embedded Ag/Ni Metal-Mesh with Low Surface Roughness As Transparent Conductive Electrode for Optoelectronic Applications. *ACS Appl. Mater. Interfaces***2017**, *9* (42), 37048–37054.

(49)   Aharon, S.; Layani, M.; Cohen, B.-E.; Shukrun, E.; Magdassi, S.; Etgar, L. Self-

Assembly of Perovskite for Fabrication of Semitransparent Perovskite Solar Cells. *Adv. Mater. InterfacesAdvanced Mater. Interfaces***2015**, *2* (12).

(50) Kiruthika, S.; Singh, S.; Kulkarni, G. U. Large Area Transparent ZnO Photodetectors with Au Wire Network Electrodes. *RSC Adv.***2016**, *6* (50), 44668–44672.

(51) Lee, H. B.; Jin, W.-Y.; Ovhal, M. M.; Kumar, N.; Kang, J.-W. Flexible Transparent Conducting Electrodes Based on Metal Meshes for Organic Optoelectronic Device Applications: A Review. *J. Mater. Chem. C***2019**, *7* (5), 1087–1110.

(52) Hong, S.; Yeo, J.; Kim, G.; Kim, D.; Lee, H.; Kwon, J.; Lee, H.; Lee, P.; Ko, S. H. Nonvacuum, Maskless Fabrication of a Flexible Metal Grid Transparent Conductor by Low-Temperature Selective Laser Sintering of Nanoparticle Ink. *ACS Nano***2013**, *7* (6), 5024–5031.

(53) Song, S. H.; Park, K. H.; Kim, B. H.; Choi, Y. W.; Jun, G. H.; Lee, D. J.; Kong, B.-S.; Paik, K.-W.; Jeon, S. Enhanced Thermal Conductivity of Epoxy–Graphene Composites by Using Non-Oxidized Graphene Flakes with Non-Covalent Functionalization. *Adv. Mater.***2013**, *25* (5), 732–737.

(54) Li, N.; Chen, Z.; Ren, W.; Li, F.; Cheng, H.-M. Flexible Graphene-Based Lithium Ion Batteries with Ultrafast Charge and Discharge Rates. *Proc. Natl. Acad. Sci. U. S. A.***2012**, *109* (43), 17360–17365.

(55) Yao, J.; Lin, J.; Dai, Y.; Ruan, G.; Yan, Z.; Li, L.; Zhong, L.; Natelson, D.; Tour, J. M. Highly Transparent Nonvolatile Resistive Memory Devices from Silicon Oxide and Graphene. *Nat. Commun.***2012**, *3* (1), 1101.

(56)   Das, A.; Pisana, S.; Chakraborty, B.; Piscanec, S.; Saha, S. K.; Waghmare, U. V; Novoselov, K. S.; Krishnamurthy, H. R.; Geim, A. K.; Ferrari, A. C.; et al. Monitoring Dopants by Raman Scattering in an Electrochemically Top-Gated Graphene Transistor. *Nat. Nanotechnol.***2008**, *3* (4), 210–215.

(57)   Zurutuza, A.; Marinelli, C. Challenges and Opportunities in Graphene Commercialization. *Nat. Nanotechnol.***2014**, *9* (10), 730–734.

(58)   Stern, A. G. A New Sustainable Hydrogen Clean Energy Paradigm. *Int. J. Hydrogen Energy***2018**, *43* (9), 4244–4255.

(59)   Li, J.-S.; Wang, Y.; Liu, C.-H.; Li, S.-L.; Wang, Y.-G.; Dong, L.-Z.; Dai, Z.-H.; Li, Y.-F.; Lan, Y.-Q. Coupled Molybdenum Carbide and Reduced Graphene Oxide Electrocatalysts for Efficient Hydrogen Evolution. *Nat. Commun.***2016**, *7* (1), 11204.

(60)   Qu, Y.; Ke, Y.; Shao, Y.; Chen, W.; Kwok, C. T.; Shi, X.; Pan, H. Effect of Curvature on the Hydrogen Evolution Reaction of Graphene. *J. Phys. Chem. C***2018**, *122* (44), 25331–25338.

(61)   Kumatani, A.; Miura, C.; Kuramochi, H.; Ohto, T.; Wakisaka, M.; Nagata, Y.; Ida, H.; Takahashi, Y.; Hu, K.; Jeong, S.; et al. Chemical Dopants on Edge of Holey Graphene Accelerate Electrochemical Hydrogen Evolution Reaction. *Adv. Sci.***2019**, *6* (10), 1900119.

(62)   Kiruthika, S.; Gupta, R.; Anand, A.; Kumar, A.; Kulkarni, G. U. Fabrication of Oxidation-Resistant Metal Wire Network-Based Transparent Electrodes by a Spray-Roll Coating Process. *ACS Appl. Mater. Interfaces***2015**, *7* (49), 27215–27222.

(63)   Wang, B.-Y.; Yoo, T.-H.; Lim, J. W.; Sang, B.-I.; Lim, D.-S.; Choi, W. K.; Hwang,

D. K.; Oh, Y.-J. Enhanced Light Scattering and Trapping Effect of Ag Nanowire Mesh Electrode for High Efficient Flexible Organic Solar Cell. *Small* **2015**, *11* (16), 1905–1911.

(64) Jin, W.-Y.; Ginting, R. T.; Ko, K.-J.; Kang, J.-W. Ultra-Smooth, Fully Solution-Processed Large-Area Transparent Conducting Electrodes for Organic Devices. *Sci. Rep.* **2016**, *6* (1), 36475.

(65) Kim, H.-J.; Lee, S.-H.; Lee, J.; Lee, E.-S.; Choi, J.-H.; Jung, J.-H.; Jung, J.-Y.; Choi*, D.-G. High-Durable AgNi Nanomesh Film for a Transparent Conducting Electrode. *Small* **2014**, *10* (18), 3767–3774.

(66) Guo, C. F.; Ren, Z. Flexible Transparent Conductors Based on Metal Nanowire Networks. *Mater. Today* **2015**, *18* (3), 143–154.

(67) Rao, K. D. M.; Hunger, C.; Gupta, R.; Kulkarni, G. U.; Thelakkat, M. A Cracked Polymer Templated Metal Network as a Transparent Conducting Electrode for ITO-Free Organic Solar Cells. *Phys. Chem. Chem. Phys.* **2014**, *16* (29), 15107–15110.

(68) Walia, S.; Gupta, R.; Rao, K. D. M.; Kulkarni, G. U. Transparent Pd Wire Network-Based Areal Hydrogen Sensor with Inherent Joule Heater. *ACS Appl. Mater. Interfaces* **2016**, *8* (35), 23419–23424.

(69) Walia, S.; Mondal, I.; Kulkarni, G. U. Patterned Cu-Mesh-Based Transparent and Wearable Touch Panel for Tactile, Proximity, Pressure, and Temperature Sensing. *ACS Appl. Electron. Mater.* **2019**, *1* (8), 1597–1604.

(70) Kiruthika, S.; Kulkarni, G. U. Smart Electrochromic Supercapacitors Made of Metal Mesh Electrodes with Polyaniline as Charge Storage Indicator. *Energy*

*Technol.***2020**, 1901364.

(71) Gupta, R.; Rao, K. D. M.; Kiruthika, S.; Kulkarni, G. U. Visibly Transparent Heaters. *ACS Appl. Mater. Interfaces***2016**, *8* (20), 12559–12575.

(72) Gupta, R.; Rao, K. D. M.; Srivastava, K.; Kumar, A.; Kiruthika, S.; Kulkarni, G. U. Spray Coating of Crack Templates for the Fabrication of Transparent Conductors and Heaters on Flat and Curved Surfaces. *ACS Appl. Mater. Interfaces***2014**, *6* (16), 13688–13696.

Chapter 2

Experimental Methods

Various characterisation techniques were used to analyse and study the devices made in this thesis work. The present chapter details the instruments used for characterisation.

2.1 Scanning electron microscopy (SEM)

SEM is used to image objects or features in an object which are not visible by an optical microscope due to limitation of wavelength in the visible range. It produces image of a sample by scanning the surface with a focused beam of electrons in a raster scan pattern. The electrons interact with atoms in the sample, producing various signals including secondary electrons, back-scattered electrons, X-rays and Auger electrons. X-rays are characteristic of the elements present in the sample, hence can be used to study the chemical composition, called energy dispersive X-ray spectroscopy (EDS). The Auger electrons are used to map local chemical composition of nanostructures with good spatial resolution. Backscattered and secondary electrons are required for imaging surface topography. Topography contrast arises because the number and trajectories of backscattered electrons and the number of secondary electrons depend on the angle of incidence between the beam and the specimen surface. Due to large depth of focus of electron beams, 3D images can be acquired.[1]

In the present study, FESEM was performed using Nova NanoSEM 600 equipment (FEI Co., The Netherlands). EDS mapping was performed using EDAX Genesis V4.52 (USA) attached to the SEM column. Low vacuum imaging was done in the same instrument using STEM and helix detectors respectively. For working in low vacuum environment, the pole piece was mounted with low vacuum detector (LVD) and the chamber was filled with water vapour at chamber pressure of ~4×10^{-3} Torr.

2.2 Optical microscopy

The optical images were procured with the Laben microscope, India which had magnification of 50X, 100X, 200X, 500X and 1000X. The microscope had transmission as well as reflective mode. The images were captured using pixel link software. An inverted dark-field microscope equipped with a dark-field condenser and a CCD camera (Pixel Link, PL-S621CU) was assembled from the Laben Instruments, India IM-20BD. Dark-field micrographs were obtained at 5X and 10X magnifications.

2.3 Solar simulator

To test a solar cell, it is required to measure its current-voltage characteristics, it is required to be kept in sunlight and compared to the characteristics in dark. The presence of clouds and change in solar inclination in different places do not allow comparison of solar cells and their standardisation. A solar simulator is a device that provides illumination just like the natural sunlight and provides a controllable indoor facility under laboratory conditions. The light from the simulator can be controlled in

three dimensions namely spectral content, spatial uniformity, and temporal stability. Each dimension is classified in one of three classes: A, B, or C, where the class A has the best spectral match of 0.75 – 1.25, least spatial non-uniformity of only 2% and the least temporal instability of 2%. In the present study, all the measurements were performed under AM 1.5 illumination using solar simulator model ss-50AAA-GB.

2.4 Transmission electron microscopy (TEM) and electron diffraction (ED)

TEM is a microscopy technique in which a beam of electrons is transmitted through a specimen to form an image. An image is formed from the interaction of the electrons with the sample as the beam is transmitted through the specimen. The image is then magnified and focused onto a fluorescent screen. Owing to the small de Broglie wavelength of electrons, TEM is capable of imaging at a significantly higher resolution, enabling to capture finer details, even as small as single column of atoms.[2] A TEM is capable of returning an extraordinary variety of nanometric and atomic-resolution information, revealing not only the locations of atoms but also the kinds of atoms they are and how they are bonded to each other. The lenses of a TEM are what gives it its flexibility of operating modes and ability to focus down to the atomic scale and magnify them back up to get an image on a camera. A lens is usually made of a solenoid coil surrounded by ferromagnetic materials designed to concentrate the coil's magnetic field into a precise and confined shape. Typically, there are three stages of lensing. The stages are the condenser lenses, the objective lenses, and the projector lenses. The condenser lenses are responsible for primary beam formation, while the objective lenses

focus the beam that comes through the sample itself. The projector lenses are used to expand the beam onto the phosphor screen or other imaging device, such as a film. In the present work, the TEM and ED were recorded using Technai F30 UHR instrument at 200KV.

2.5 Raman spectroscopy

It is a spectroscopy technique typically used to determine vibrational modes of molecules, although rotational and other low-frequency modes of systems may also be observed. Raman spectroscopy relies upon inelastic scattering of photons. A source of monochromatic light, usually from a laser in the visible, near infrared, or near ultraviolet range is used, although X-rays can also be used. The laser light interacts with molecular vibrations, phonons or other excitations in the system, resulting in the energy of the laser photons being shifted up or down. The magnitude of the Raman effect correlates with polarizability of the electrons in a molecule.[3] It is a form of elastic light scattering, where a photon excites the sample. This excitation puts the molecule into a virtual energy state for a short time before the photons are emitted. The Raman effect is based on the interaction between the electron cloud of a sample and the external field of the monochromatic light, which can create an induced dipole moment within the molecule based on its polarizability. Raman spectra were recorded in the backscattered geometry and three lasers were used having excitation wavelengths of 523, 630 and 785 nm using Horiba XploRA ONE Raman microscope with a motorized

sample stage. The Raman scans were taken at 50X objective length with power of 3 mW

at sample surface. The laser spot size is ~ 3 µm for the 50X objective used.

2.6 Atomic force microscopy (AFM)

AFM has a very high-resolution, of the order of fractions of a nanometre, more than

1000 times better than the optical diffraction limit. A small cantilever typically made up

of silicon or silicon nitride, with a sharp tip at one end is scanned over the surface,

bending the cantilever up and down, and hence changing the direction of light falling

on the tip.[4] This reflected light is captured by a photodiode. The height of the cantilever

is then adjusted to restore the response signal resulting in the measured cantilever

height tracing the surface. The reaction of the probe to the forces that the sample

imposes on it, can be used to form an image of the topography of a sample surface. It is

different from the other microscopy techniques because it does not use any lenses or

beam irradiation. Therefore, it does not suffer from aberration or limitations in spatial

resolution and does not need vacuum or staining the sample. The AFM can be operated

in several modes namely contact mode or tapping mode. In contact mode, the tip is

dragged across the sample surface and the contours of the surface are measured either

using the cantilever deflection or by using the feedback signal required to keep the

cantilever at a constant position. In tapping mode, the tip is kept at a close distance to

the sample so that it becomes detectable owing to a short-range force. The cantilever is

driven to oscillate up and down at its resonance frequency. The amplitude of this

oscillation varies from several nm to 200 nm and is kept constant as long as there is no

interaction with the surface. In the present study, AFM was performed using Multimode, Veeco digital instruments, USA with Nanoscope IV controller. The scanner was calibrated using a standard Pt coated Au grid with a pitch of 1 µm.

2.7 Optical profiler (OP)

OP measures step heights and surface roughness using light, in a way that it can detect the surface in 3D. A beam is shone at a surface and the time taken to return is measured. It has resolution from a few µm to hundreds of nanometres. A light beam is split, reflecting from the reference and test material followed by formation of interference fringes. The optical path differences are due to height variances in the test surfaces. Films which have a reflective surface such as silicon or glass were images using Wyko NT9100 (Veeco, USA) optical profiler. For roughness more than 160 nm, vertical scanning interferometry was utilised and for roughness less than 160 nm, phase shifting interferometry was employed.

2.8 UV-Vis spectroscopy

This spectroscopy technique uses light in the visible and adjacent ranges. This is the electromagnetic radiation range in which atoms and molecules undergo electronic transitions. To measure the transmittance, reflectance and absorbance of thin films, UV-visible spectra were recorded using Perkin-Elmer Lambda 900 UV/vis/NIR spectrophotometer using 1 mm path length cuvette.

2.9 X-ray diffraction (XRD)

The range of electromagnetic radiation wavelength matching the size of atoms, is the same as that of x-rays. Regular arrays of atoms scatter X-rays producing a regular array of spherical waves leading to constructive interference in specific directions determined by Bragg's law:

$$2d\sin\theta = n\lambda,$$

where d is the spacing between diffracting planes, θ is the incident angle, n is any integer, and λ is the wavelength of the beam.[5] By measuring θ, under which the constructive interference happens, the interplanar spacings, d, of every single crystallographic phase can be determined. The peak positions and intensities not only help in qualitative analysis but are also useful for lattice constant determination and stress determination of the sample. For this thesis work, Bruker D8 Discover diffractometer was used, attached with temperature and humidity-controlled stage with source, Cu Kα (λ = 1.5419 Å).

2.10 Electrical measurements

Electrical measurements were performed using Keithley 236 source measure unit and Keithley-4200 semiconductor characterization system in current-voltage and current-time modes. Temperature dependent measurements were performed using a cooling/heating stage (Linakm 600) equipped with a temperature controller (Linkam TMS 94).

2.11 References

(1)   Spiegelberg, S.; Kozak, A.; Braithwaite, G. 29 - Characterization of Physical, Chemical, and Mechanical Properties of UHMWPE; Kurtz, S. M. B. T.-U. B. H. (Third E., Ed.; William Andrew Publishing: Oxford, 2016; pp 531–552.

(2)   Bonnamy, S.; Oberlin, A. Chapter 4 - Transmission Electron Microscopy; Inagaki, M., Kang, F. B. T.-M. S. and E. of C., Eds.; Butterworth-Heinemann, 2016; pp 45–70.

(3)   Lau (Deceased), E. 5 - Preformulation Studies. In *Handbook of Modern Pharmaceutical Analysis*; Ahuja, S., Scypinski, S. B. T.-S. S. and T., Eds.; Academic Press, 2001; Vol. 3, pp 173–233.

(4)   Nasrollahzadeh, M.; Atarod, M.; Sajjadi, M.; Sajadi, S. M.; Issaabadi, Z. Chapter 6 - Plant-Mediated Green Synthesis of Nanostructures: Mechanisms, Characterization, and Applications. In *An Introduction to Green Nanotechnology*; Nasrollahzadeh, M., Sajadi, S. M., Sajjadi, M., Issaabadi, Z., Atarod, M. B. T.-I. S. and T., Eds.; Elsevier, 2019; Vol. 28, pp 199–322.

(5)   Chatterjee, A. K. 8 - X-Ray Diffraction; Ramachandran, V. S., Beaudoin, J. J. B. T.-H. of A. T. in C. S. and T., Eds.; William Andrew Publishing: Norwich, NY, 2001; pp 275–332.

Chapter 3

Metal Mesh Electrodes

3.1 Highly conformal Ni micromesh as a current collecting front electrode for reduced cost Si solar cell.

3.2 A cosmetic adaptable transparent strain sensor for sensitive delineating patterns in small movements of vital human organs.

Chapter 3.1

Highly Conformal Ni Micromesh as a Current Collecting Front Electrode for Reduced Cost Si Solar Cell

Summary: In the present work, a highly interconnected metal wire network has been employed as front electrode on conventional Si wafers. Here for the first time, an innovative solution-based crackle templating method was employed for conformal metal wire network patterning over large textured surfaces. Laser beam induced current mapping showed uniform photocurrent collection by the electrodes without any shadow losses. With electroless deposition of Ni wire network on corrugated solar cell, a short circuit current of 33.28 mA/cm² was obtained in comparison to 20.53 mA/cm² without the network electrode. On comparing the efficiency with the conventional cells with screen printed electrodes, a 20% increment in efficiency has been observed. Importantly, the estimated manufacturing cost is at least two orders lower. Apart from substituting the screen-printed electrode with crackle-based metal network, the latter was also deposited on commercial Si solar cells, leading to increase in efficiency and stability in spite of having higher shadowing losses.

3.1.1 Introduction

Conventional Si-based photovoltaics (SiPV) continues to contribute to nearly 90%[1-2] of the total electrical energy harvested from the solar radiation in spite of immense developments in new generation cells based on perovskite,[3-5] organic,[6-8] inorganic,[9-11] quantum dot[12-14] as well as hybrid materials.[15] Scalable production, high on-field efficiencies as well as their extraordinary environmental stability have kept the Si solar cells forefront in the photovoltaic race.[16-18]

The downside of the SiPV technology is related to one of the commercial aspects, namely the manufacturing cost of which a major component is the expensive screen printing process of the front contacts made of Ag grid.[19-20] Not only Ag as a metal is expensive, the printing process produces considerable amount of Ag waste which is not so easily recoverable, raising the overall manufacturing cost of the cells by as much as ~ 30%.[21] Replacing Ag by cheaper metals such as Ni or Cu though may serve well enough in retaining the output photovoltaic parameters, the associated processes are not straightforward.[21] Specifically, it is not common to find formulations of the corresponding metal inks, which are amenable to the screen printing process and produce high quality electrode lines upon metallisation.[21] Although the Ag grid as front contact bears a small footprint of ~ 10% on the active area,[22] the screen printed electrode lines are rather broad (~100 μm) causing considerable shadowing.[23] In order to produce unbroken, well conducting lines, screen printing demands a high aspect ratio (~ 0.3) for the lines which further adds to the cost.[24] Besides, the grid lines are relatively far apart (~ 2 mm) compared to the mean free path of the photogenerated

carriers (100 μm) which amounts to some power loss.[22] In spite of such issues, the screen printing method is still inevitable considering the antireflective roughened cell surface which is unfriendly to low cost contact based lithography techniques. Alternate methods such as inkjet,[25] multiple[26-27] and direct printing[28] have been explored for narrower Ag finger electrodes. For example, Mette et. al. used a modified screen printing paste in aerosol jet printing technique.[29] Photolithography, although widely used in making Si solar cells, is not favored for commercialization due to expensive photomasks and relatively large number of process steps.[30-31] The work presented in this article aims at an alternative solution to the Si cell front electrode.

As a replacement for Ag grid electrode, graphene coating,[32-33] PEDOT:PSS film[34-35] and carbon nanotube (CNT) networks[36-37] have been tried out as transparent conducting layer on Si device surface. There have been efforts to improve the cell performance by molecular doping of graphene[37] and also by coating an antireflective TiO_2[38] on top. However, few layer graphene of high quality over large area is not yet an affordable technology.[39] Similarly, the performance of CNT network can be improved by acid infiltration[40] or by TiO_2[41] coating. The CNTs although inherently highly conducting, tend to form networks with relatively high sheet resistances due to significant contribution from the junction resistance.[42] Further, the redundant tubes increase the haze leading to some optical losses without really contributing to the current collection.[43] Given the textured cell surface, ensuring CNT-Si conformal contact over large areas is difficult. These issues are being addressed by depositing a conducting polymer layer such as PEDOT:PSS over the networks.[44-45] There are also reports of using

Ag nanowires in combination with the PEDOT:PSS to improve the film conductivity.[46-47] However, the long term stability of such electrodes is always a matter of concern due to possible degradation of the organic layers.[48]

3.1.2 Scope of the present investigation

Despite having enormous commercial demand, owing to high conversion efficiency and long life, crystalline-Si solar cells suffer from a relatively high manufacturing cost. As regards cost, one pertinent issue is the top electrode metallization of textured cell surface, which typically involves screen printing of silver paste. The associated disadvantages call for alternative methods that can lower the cost without compromising the solar cell efficiency. Solution process could help in greatly help in reducing the amount of metal used, especially if the metal used is less costlier compared to silver, thereby reducing the overall cost. The present work addresses this issue by substituting the conventional screen-printed electrodes with solution-processed crackle patterned Ni electrodes. The solution process and the raw materials reduce the overall cost by two orders, along with 20% higher efficiency. The small feature size of the crackle network allows for coating over a commercial silicon solar cell with negligible additional shadowing losses, to increase their efficiency further.

3.1.3 Experimental Section

Fabrication of crack template: The plain Si wafers (100 oriented, n-doped, 10 Ωcm) were obtained from VinCorolla. Si solar cells, both prefinished till doping and fully finished with antireflection coating were obtained from Bharat Heavy Electronics Ltd., Bangalore. Both the plain Si wafers (100 oriented, n-doped, 10 Ωcm) and the prefinished corrugated Si solar cells were cut into 1 cm² pieces and were cleaned by ultrasonication in acetone, iso-propyl alcohol, and deionized water consecutively. To introduce the crackle template, a commercially available crack nail polish (Ming Ni Cosmetics Co., Guangzhou, China) consisting of acrylic emulsion was dispersed in diluter (having concentrations of 0.7 and 1 g/mL for plain and corrugated cells respectively) and rigorously ultrasonicated for 30 min. The mixture was spin coated on each substrate at 1000 rpm for 60 s.

Electroless Deposition of Metal on crack template: Au electroless solution was prepared by dissolving 2% hydrofluoric acid in 10 mM aqueous chloroauric acid. Ni electroless solution was prepared by dissolving 3 g Ni chloride, 2 g sodium hypophosphite, 6.5 g triammonium citrate in water.[49] This solution was mixed with ammonium hydroxide in the ratio 20:1 at 70 °C. A 1% HF etch is performed to remove native oxide layer from the Si surface before CP coating. During the deposition, edges of Si solar cell were isolated with polystyrene to prevent shorting. After metal deposition, the crack template was removed by lifting it off in chloroform and further rinsing by IPA. Cu wires are connected on top and at bottom using Ag paste to make the devices. The square-shaped Ag top contact is made close to the periphery to ensure

maximum current collection (see Figure 3.1.1). The Ni wire network is uniformly coated over the textured cell as shown by the optical micrograph image in Figure 3.1.1d. The feature size is very small and is not visible by naked eyes. The commercial Si solar cells used in current study is obtained by cutting a 3-busbar solar cell into 1 cm² pieces. As shown in Figure 3.1.1e, the conventional solar cell has been intentionally cut away from the busbar to avoid extra shadowing.
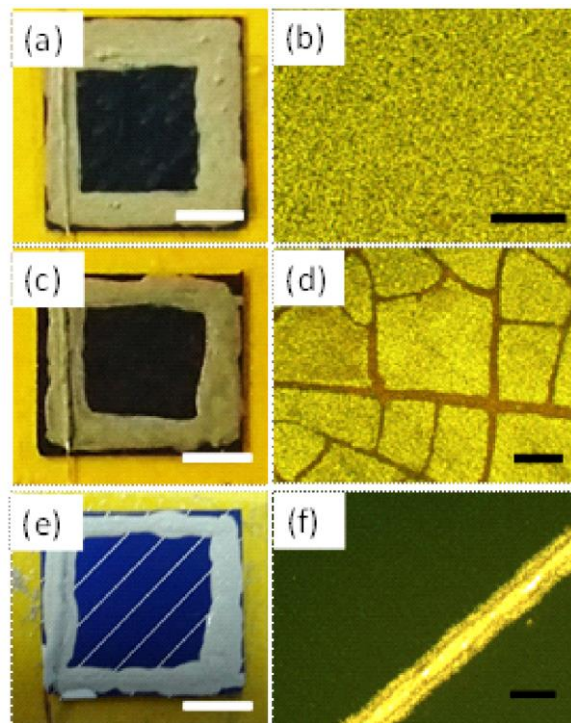

Figure 3.1.1 Comparison of three types of cells used in the study. Digital photographs of (a) prefinished Si solar cell, (c) Ni network coated Si solar cell and (e) conventional Si solar cell, with their respective optical micrographs given in (b), (d) and (f). The white and black scale bars represent 5 mm and 100 μm respectively.

Characterization: The electrical connections were made using Ag paste on the top and bottom of the cell with Cu wires to make circuit connections. The device was connected to the Keithley 2400 setup for I-V measurement. All the measurements were

performed in ambient conditions under AM 1.5 illumination using solar simulator model SS-50AAA-GB.

Laser beam induced current mapping (LBIC): The LBIC experiments were carried out at DTU, Denmark using a custom-made setup with 410 nm laser diode (5 mW output power, 100 μm spot size ~ 65 W/cm^2, Thor Labs) mounted on a computer controlled XY-stage. A custom written computer program was used to scan the Au wire network in a raster pattern in 200 μm steps in the X and the Y directions, logging the coordinates and measured current. The results were then converted to yellow/blue colored bitmaps in 255 different hues with another custom written program. Bright yellow represents the highest absolute current extracted while blue represents the lowest current. Current profiles along selected directions were taken from these maps to visualize the relative differences over the entire active surface.

3.1.4 Results and Discussion

3.1.4.1 Improving photoconductivity in doped Si by Au metal mesh

In this work, crackle templating method is used to deposit patterned metal, relying on making crack groves.[50] The patterned metal emerges as a fine wire mesh closely following the highly interconnected crack pattern itself. Prior to applying the method on Si solar cells, Au meshes were first deposited on plain, undoped Si substrates via electroless plating and the possibility of enhancing the collection of photogenerated charges was explored.
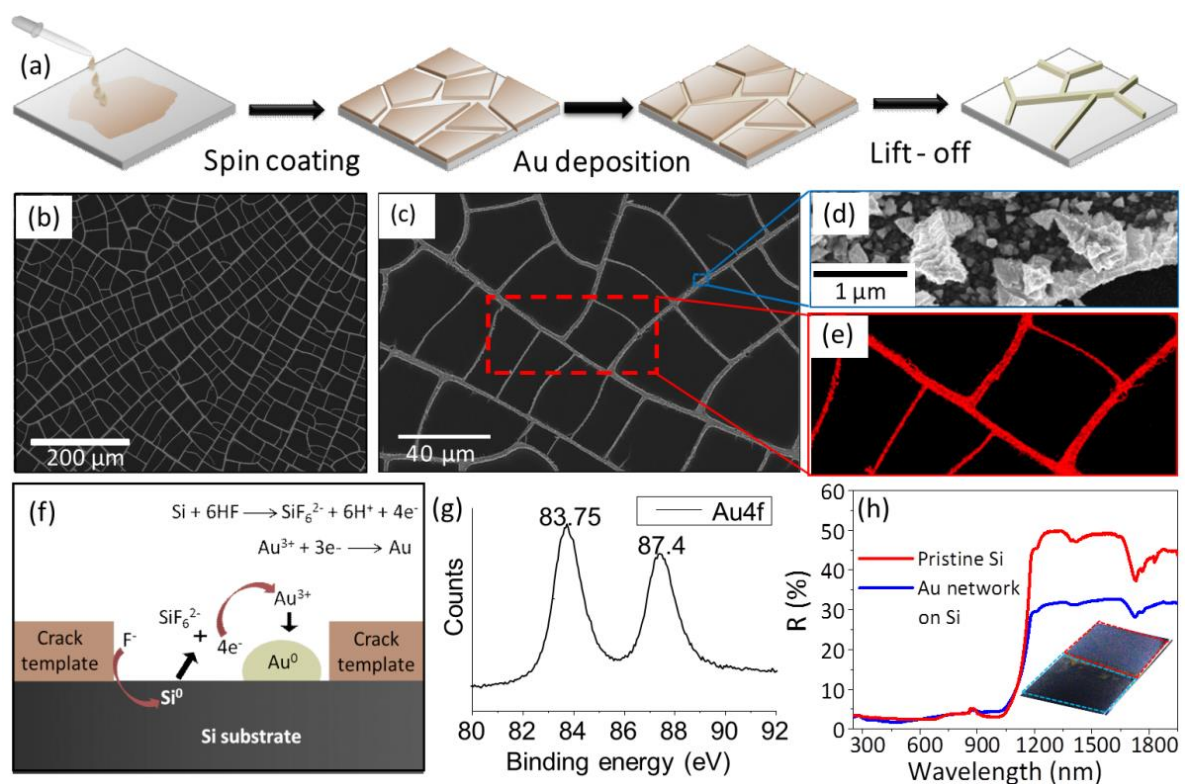
Figure 3.1.2 Fabrication and characterization of metal wire electrode on Si. (a) Schematic demonstration of the steps involved in the fabrication of Au wire network on Si substrate following crackle lithography. SEM images of Au wire network (b) showing the bird eye view over a large area (1.8 mm×1.5 mm), (c) and (d) are magnified views. (e) EDS map of the region marked by red dashed square (f) Mechanism for reduction of Au on Si exposed from the crackle grooves. (g) XPS spectra for Au 4f signal. (h) Reflectance spectra for pristine Si and Au wire network on Si with a digital photograph of pristine Si (inside red dotted rectangle) and Au network coated Si (inside blue dotted rectangle).

Briefly, a colloidal crackle precursor (CP) was spin coated on a polished n-type (100) oriented Si substrate, as depicted in Figure 3.1.2a. Upon drying, a highly interconnected micro-crack pattern formed spontaneously with clear grooves without any residual layer. Interestingly, these cracks are found to be much narrower in width (~ 2 μm) compared to those on PET, quartz and glass substrates made in our previous studies.[51-

[52] In many regions, the crack widths were down to 700 nm. The colloidal film of crackle precursor is known to form crackles due to the normal stress caused during the solvent evaporation and cohesive force between the colloidal particles. The optical micrograph of the crackle patterns is shown in Figure 3.1.3a showing high interconnectivity of cracks with each other which is crucial for electrode fabrication. The crackles start from one end of the substrate and end on the other end, virtually limited by the substrate area. Indeed, the crackle film consists of islands of squares, triangles and polygons. More importantly, the crackles are down to substrate without any residual layers, the substrate is seen through the crackle, which is depicted in Figure 3.1.3b and c. This is an essential thing for the usage of crackle as a template for

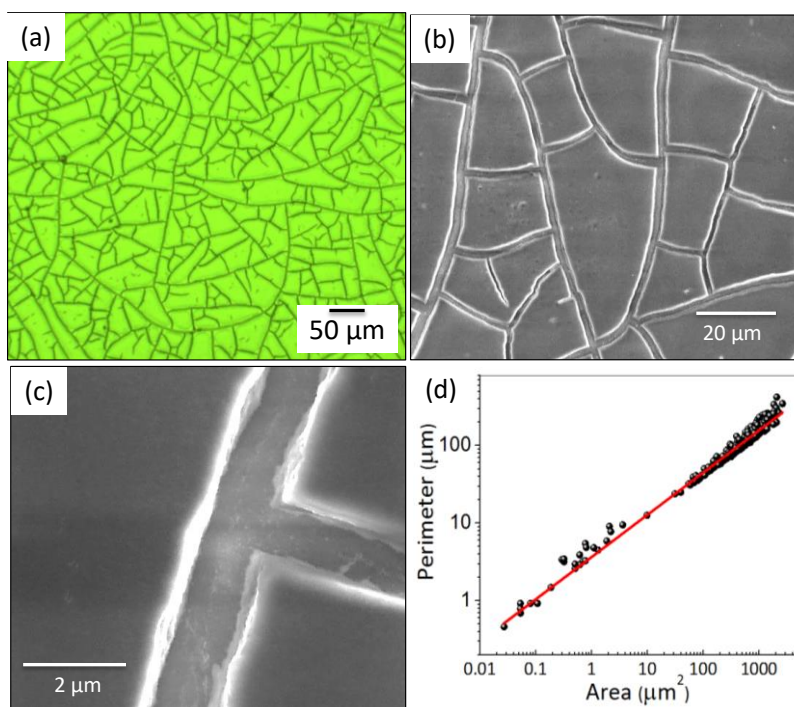
Figure 3.1.3 Microscopy analysis of crack formation. (a) Optical micrograph and (b) SEM image of crackle patterns, (c) magnified view of a single crackle. (d) log-log plot between perimeter and area of the crackle network calculated from (a).

patterning. The perimeter versus area curve follows power law as shown in Figure 3.1.3d, and the calculated fractal dimension is 1.08.[53] The exposed Si surface within the crack groove provides an active site for electroless deposition of Au (see Experimental Section).

Following deposition for 30 s, the crackle template was washed away in chloroform leaving a continuous large network of Au wires on Si substrate (see Figure 3.1.2b). The Au wire network is continuous from one end of the substrate to the other. Figure 3.1.2b shows Au wires uniformly spread over (Figure 3.1.2c) with cell sizes of ~ 960 μm^2. The EDS map in Figure 3.1.2e shows Au signal from the crackle region. Electroless deposition on Si involves a galvanic displacement reaction (see Figure 3.1.2f) essentially leading to metallic Au, as confirmed from the core level $4f_{7/2}$ and $4f_{5/2}$ positions, 83.75 and 87.40 eV respectively (Figure 3.1.2g). The novel features of the crack templating method are evident. The junctions in the wire network are seamless in contrast to crossbar junctions encountered in the conventional wire networks.[43]

Accordingly, the sheet resistance of the wire network was ~ 10 $\Omega/\square$ as against the surface resistance of 200 $\Omega/\square$ of bare Si substrate, implying negligible junction resistance in the network. In order to determine the optical properties of patterned Si (Si/Au network), a reflectance spectrum was acquired in the broad IR range, 1200 nm to 2000 nm. Noticeably, it shows 12% – 15% reduced reflectance when compared to bare Si surface (see Figure 3.1.2h), which would be hugely beneficial as IR contributes significantly to the Si photoconductivity.
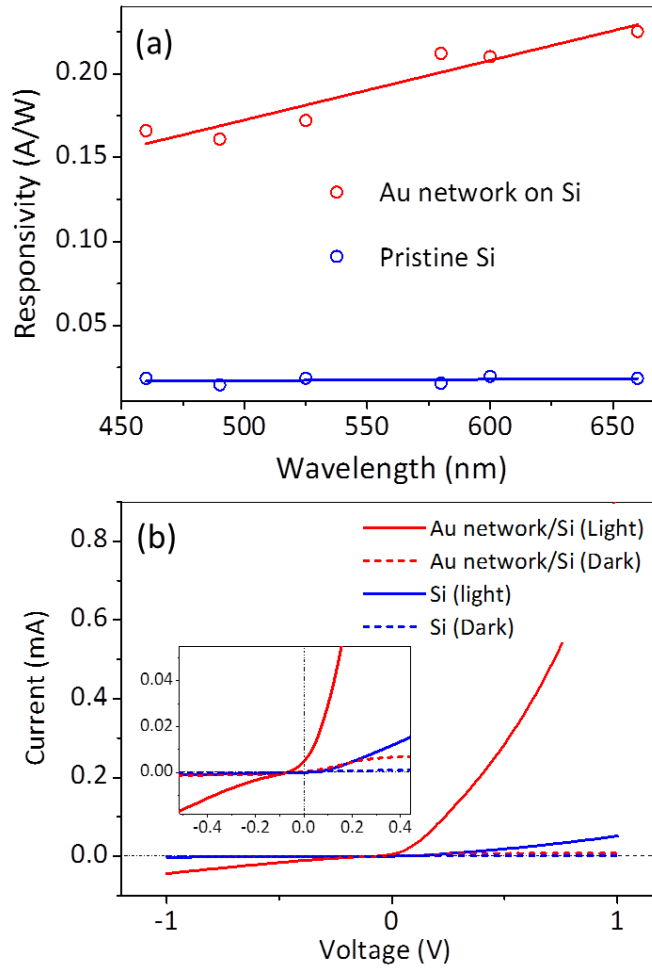
Figure 3.1.4 Photoresponse of Si/Au network. (a) Responsivity calculated for pristine and patterned Si as a function of wavelength. (b) I-V characteristics of Si with and without Au wire network in light and in dark. Inset shows the zoomed in view of I-V characteristics at origin.

On closer examination (Figure 3.1.2d), we notice that the Au wire surface is rough at the nanometer scale, exhibiting nanoconical structures, which may play an important role in enhancing inward focusing of light while reducing specular reflection.[54] This is an additional advantage derived by combining the templating method with the electroless deposition process.

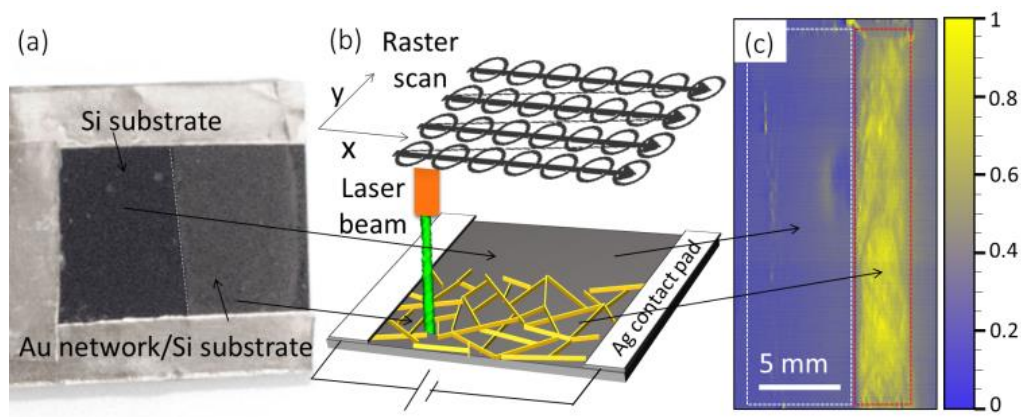**Figure 3.1.5 Laser Beam Induced Current mapping on Au network/Si.** (a) Digital Photograph of Si wafer partially covered with Au wire network. (b) Schematic showing raster scanning by laser over Si/Au network device for Laser Beam Induced Current (LBIC) experiment. (b) LBIC map of area with and without Au wire network, also marked by rectangles with red and white dotted lines respectively. The scale bar represents normalized current.

The current collection efficiency of the Au wire network was examined by measuring the responsivity of the pristine Si and Si/Au network. Figure 3.1.4a shows the DC responsivity of Si/Au network at 3 V in the visible range of 460 - 660 nm. As seen from the plot, the photoresponse of Si/Au network shows its maximum in the red region (650 nm; 0.22 A/W) going well with the inherent nature of absorption of Si.[55-56] Comparatively, the photoresponse from bare Si appears rather flat; due to increased recombination of photogenerated charge carriers in absence of current collecting grid. Importantly, the average photoresponse of Si/Au network is calculated to be 0.19 ± 0.03 A/W, which is an order higher than that of bare Si substrate. This is even more evident from the measured I-V characteristics in which the overall photocurrent under white light is also higher compared to that of bare Si (Figure 3.1.4b). Thus, it is clear that Si/Au network collects the photogenerated charge carriers effectively.

Further, the enhanced current collecting ability of Si/Au network was studied by Laser beam induced current (LBIC) mapping by bringing Au network on half of the area of Si wafer (see Figure 3.1.5a). The schematic of the LBIC process is shown in Figure 3.1.5b. The photocurrent map measured by LBIC over a large area is depicted in Figure 3.1.5c with intensity scales. As expected, the bare Si and Si/Au network region can be clearly distinguished by LBIC maps which are demarcated by white and red dotted rectangles respectively (Figure 3.1.5c). It is remarkable that in the Si/Au network region, we observe uniform distribution of the photocurrent signifying the absence of redundant wires, which would have led to shadowing losses without contributing to any photocurrent. The enhancement in the photocurrent collection is generic to any metal network grown electrolessly on Si as Ni wire network grown on Si behaves comparable to Si/Au network (see Figure 3.1.6). Having established the novel functional aspect of the metal mesh electrode on bare Si, we embarked on Si solar cell studies.
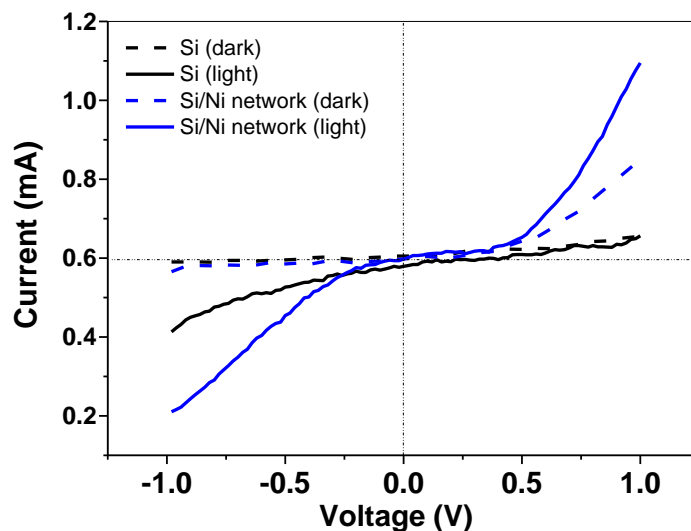
Figure 3.1.6 Photoresponse of Si/Ni network. IV characteristics of Si with and without Ni network in light and in dark.
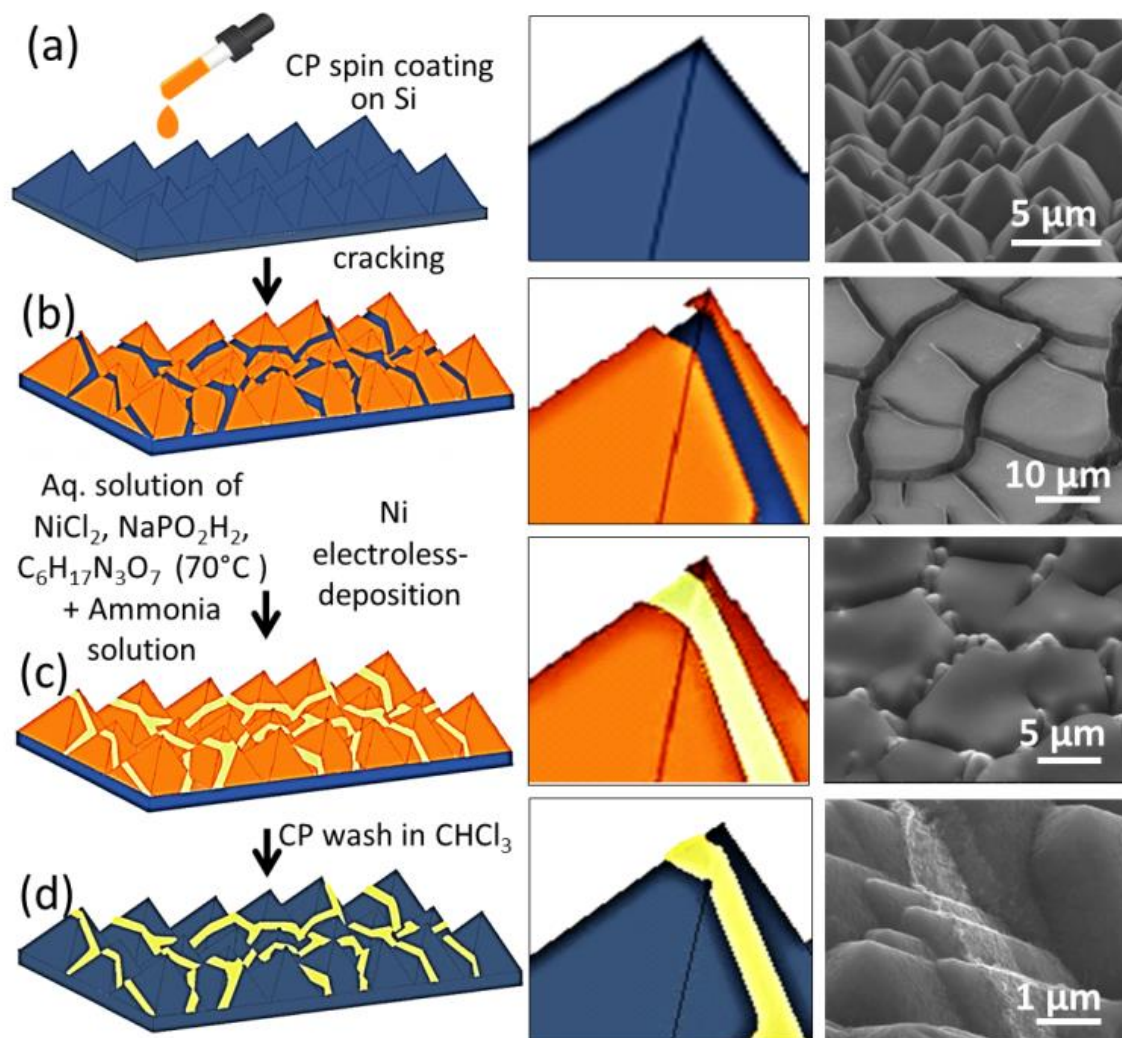
Figure 3.1.7 Fabrication of Ni wire network on corrugated p-n junction Si solar cell. (a-d) Schematic showing steps involved in the fabrication with a magnified view along with SEM images corresponding to each step. (a) Drop coating crackle precursor to get crack pattern on pristine Si solar cell. (b) Formation of cracks on the corrugated surface of Si solar cell. (c) Deposition of Ni by electroless process. (d) Conformally coated Ni wire network on Si solar cell after lift-off in $CHCl_3$. Middle column is the zoomed-in view of the left column for better depth visualization of crack. Right column represents corresponding SEM images.

3.1.4.2 Improving efficiency of Si solar cell by replacing Ag screen printed electrode

Conventionally, a Si solar cell is fabricated by phosphorus doping on front side of *p*-type Si wafer followed by anisotropic etching for texturing the front surface, depositing front and back electrodes by Ag and Al screen printing respectively and in the end passivating the top surface by SiN_x. The Si cells used in this study were without the screen-printed Ag electrodes and SiN_x passivation, termed henceforth as Ŝi solar cell (Figure 3.1.7). The pyramidally textured corrugated structure in SEM image (Figure 3.1.7a) shows its high surface roughness (~ 13 µm)[57] which is not conducive to conventional metallization by lithography. When CP was spin coated on Ŝi solar cell in a similar procedure as described previously (see Figure 3.1.2a), the crack network formation was quite facile in spite of the roughness (Figure 3.1.7b). The cracks are found to be even narrower than those observed on plain Si at the given templating conditions. The formation of such narrow cracks should lead to a much finer metal network significantly reducing the shadowing loss. In our study, we have chosen Ni for the front metallization over Au or Cu which are known to diffuse into Si with time, creating many electron-hole recombination centers.[58-60] Also, Ni is cost effective and gets easily electroless deposited on Si as can be seen in the calculation below (See Table 3.1.1).

It may be noted that the above calculations are based on used metal costs only, not involving process and wastage related costs. Ni deposited with the present method (crack template + electroless deposition) is again advantageous given that Ni^{2+} comes

from solution to get deposited in select places (crack grooves) while in case of Ag, the

paste (Ag°) is deposited using screen printing. The cost differences between Ni and Ag

may be even more than 3 orders.

Table 3.1.1 Material cost Analysis

Parameters	Ag screen printed electrode	Ni network Si solar cell electrode
Cost of the metal used ($/g)	0.703	0.014
Mass of metal used (mg)	0.100	1.2188
Cost of electrode ($/wafer)	0.07030	0.00017

(Mass of Ni was calculated using area of metal coverage to be 10% of the wafer, area of wafer to be 6" × 6" and thickness of electrode to be 1 μm)
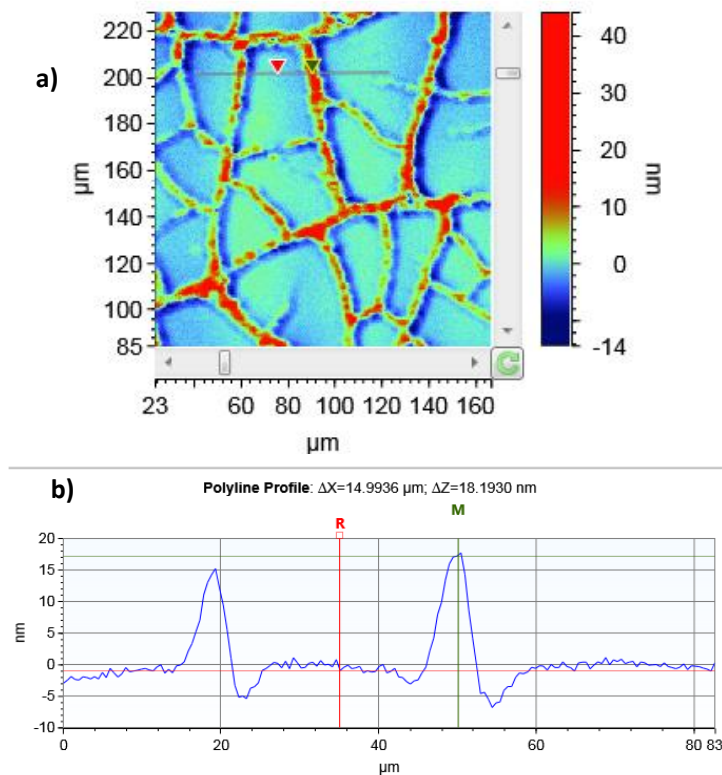

Figure 3.1.8 Optical profilometry of Si/Ni network. (a) Thickness mapping, (b) Height profile.

In order to avoid CP peeling off during solution processing, the CP templated cell was prebaked at 100 °C for 5 minutes which improved adhesion between CP and the Si surface. The substrate was then dipped in electroless Ni solution for 10 minutes (see experimental section for details). Under these conditions, Ni could be successfully deposited selectively into the crackle grooves as clearly seen from the SEM image in Figure 3.1.7c. The tiny spheres projecting out of the crack grooves result from deposition at the top of pyramids. After depositing the metal, the CP was washed away in chloroform leaving the Ni wire network intact on the top surface of Ŝi cell. It is noteworthy that the network sits conformally on the textured cell surface as shown in the SEM image in Figure 3.1.7d. The width of the metal wire network can be achieved down to ~ 1 µm, almost two orders less than what the screen-printing techniques offer. The typical thickness of Ni wires was measured to be 16 – 18 nm (see Figure 3.1.8). Thus, the combination of crackle lithography and electroless deposition on Ŝi solar cell can be effectively employed to produce conformal deposition of metal networks. The Ni network on the corrugated Si solar cell was converted into a binary bit image to calculate the area fraction of Ni network on the solar cell. It was found out to be covering ~ 10% (see Figure 3.1.9) of the total solar cell area. This value is comparable to the conventional cells with screen printed front electrodes. In order to give insight into the Ni-Si interface, XPS analysis was carried out (see Figure 3.1.10) which shows Ni rich silicide formation at the junction. The Si 2p and Ni 2p core level spectra indicate the formation of Ni_3Si as low Si presence gives rise to asymmetric Ni $2p_{3/2}$ peak. The peak

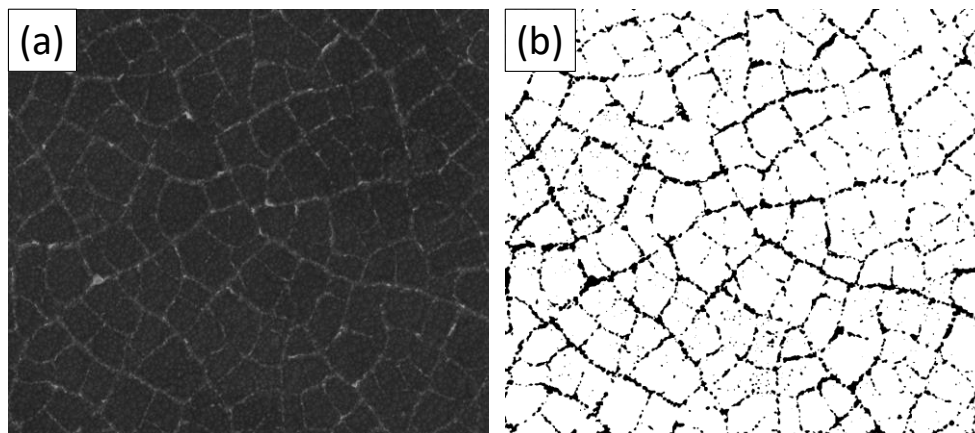**Figure 3.1.9 Calculation of area fraction of Ni electrode on Si solar cell**. (a) SEM image of Ni wire network on corrugated Si solar cell. (b) Binary bit image of the corresponding image in (a). (scale bar)
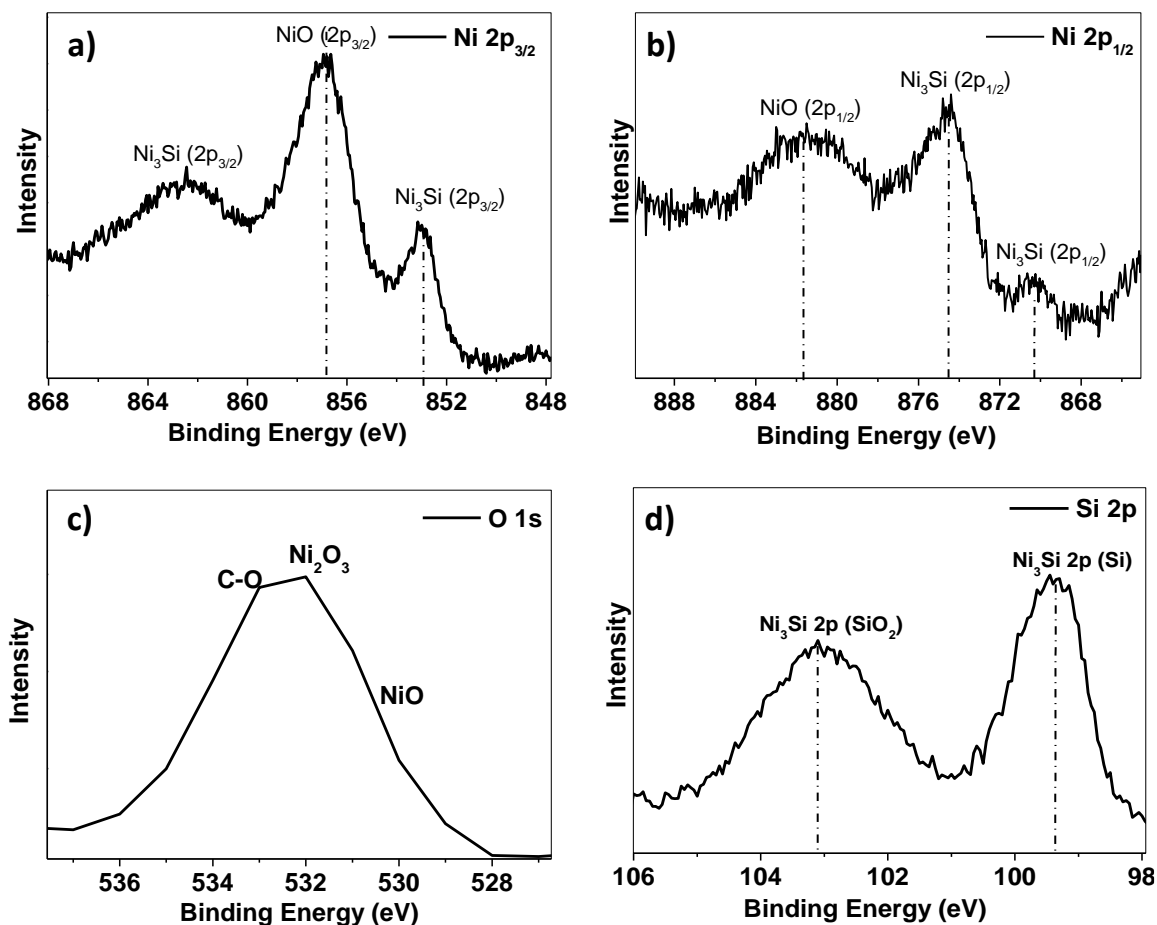

Figure 3.1.10 Normalized XPS core spectra at Ni and Si interface. Core level spectra of a) Ni $2p_{3/2}$, b) Ni $2p_{1/2}$, c) O 1s and d) Si 2p. Dotted lines are a guide to the eye.

at 881.7 eV in the Ni $2p_{3/2}$ spectrum and that at 531 eV in O1s spectrum show presence of NiO, which is possible as the deposition was carried out in ambient conditions.

The performance of Ni network coated Ŝi solar cell (Ni-Ŝi) was examined as described in Figure 3.1.11. The Ŝi solar cell without a current collecting grid shows a poor performance with a triangular shape of the blue curve in the IV quadrant in Figure 3.1.12. It is confirmed with a fill factor of only 23.8% and hence a 2.79% efficiency as shown in Table 3.1.2. Ni wire network enhanced the performance of Si solar cell even with lower duration of electroless deposition such as 5 minutes, shown by green. The conventional Si solar cell shows a squarish J-V characteristics with an efficiency of 9.3% (see Figure 3.1.11c), while electrolessly deposited Ni-Ŝi exhibits a higher efficiency of 11.2% with 10% enhancement (from 59.02% to 65.45%) in the fill factor compared to that of the conventional cell (see Table 3.1.3 for comparison). It may be noted that all Ŝi cells were from the same batch.

These parameters have been studied with varying deposition conditions as well. In all the cases, the wire networks are seen well connected and uniformly coated over the cell surface (see Figure 3.1.7d). Importantly, a 20% increment has been observed in the efficiency of the Ni-Ŝi cell. This value is underestimated considering that the conventional cell has the advantage of antireflective SiN_x coating. The observed increment can be attributed to lesser loss of the photogenerated charge carriers as they travel to the current collecting grid lines which are only few μm apart compared to few mm in conventional cells. Given the carrier diffusion length of ~100 μm in Si,[61] the finer electrode largely reduces the probability of recombination and scattering of

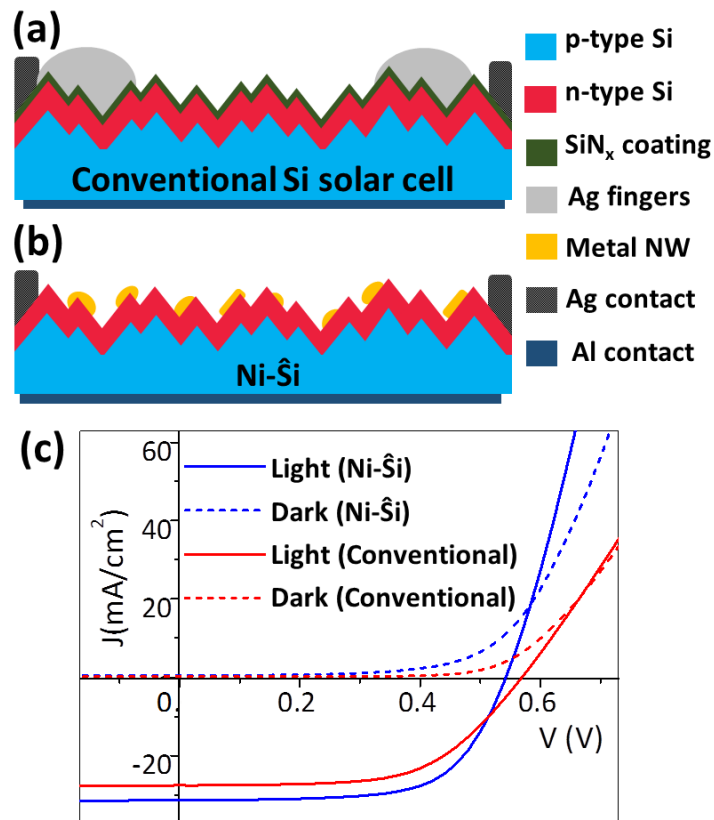**Figure 3.1.11** Performance of corrugated p-n junction Si solar cell with metal wire network top electrode. Side-view schematic of (a) conventional Si solar cell and (b) Ni-Ŝi. (c) J-V characteristics (in light and dark) of conventional Si solar cell and Ni-Ŝi.
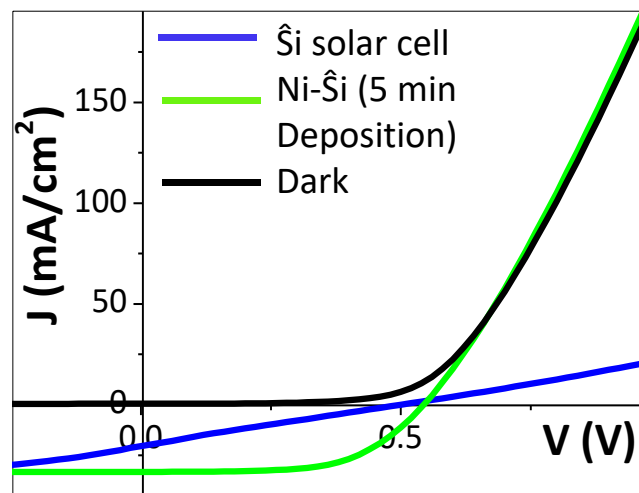
Figure 3.1.12 J-V characteristics of Si solar cell with and without Ni wire network (5 minutes electroless deposition) compared with dark.

Table 3.1.2 Performance parameters of corrugated p-n junction Si solar cell before and after Ni electroless deposition.

Ŝi Solar cell	Before Ni wire network deposition	After Ni wire network deposition
Ni electroless time (min)	-----	5
Prebake time (min)	------	5
Area (cm²)	0.79	0.69
V_{OC}(V)	0.5	0.54
J_{SC} (mA/cm²)	20.53	31.4
FF (%)	23.8	59.9
Efficiency (%)	2.26	10.06

Table 3.1.3 Performance parameters of Si solar cell prefinished to texturing and doping coated with Ni network (Ni-Ŝi) and Ag screen printed fingers (control cell).

Front electrode type	Ni network	Ag screen printed
V_{OC}(V)	0.54	0.57
J_{SC} (mA/cm²)	33.28	27.6
FF (%)	65.45	59.02
Efficiency (%)	11.15	9.3

the charge carriers.[62] This is also reflected in the high short circuit current density of 33.28 mA/cm² compared to 27.6 mA/cm² in the conventional, amounting to an increment of 21%. This is further supported by external quantum efficiency measurements where the performance of Ni-Ŝi is more pronounced in the long wavelength region compared to the conventional cell (see Figure 3.1.13). Additionally,

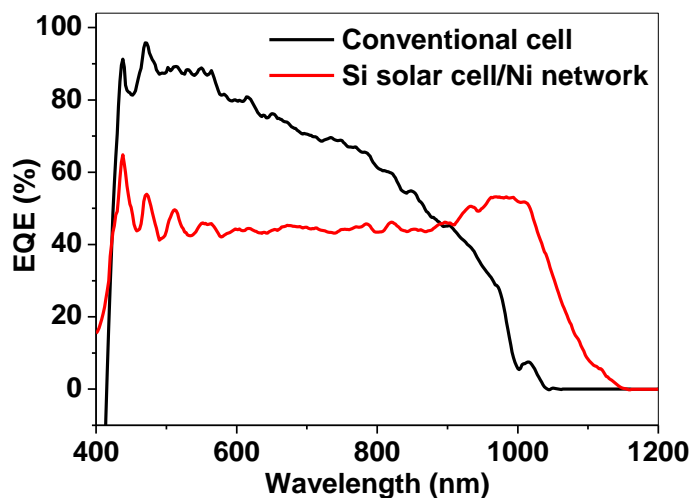**Figure 3.1.13** External Quantum Efficiency measurement of Ni-Ŝi compared with conventional cell (control).
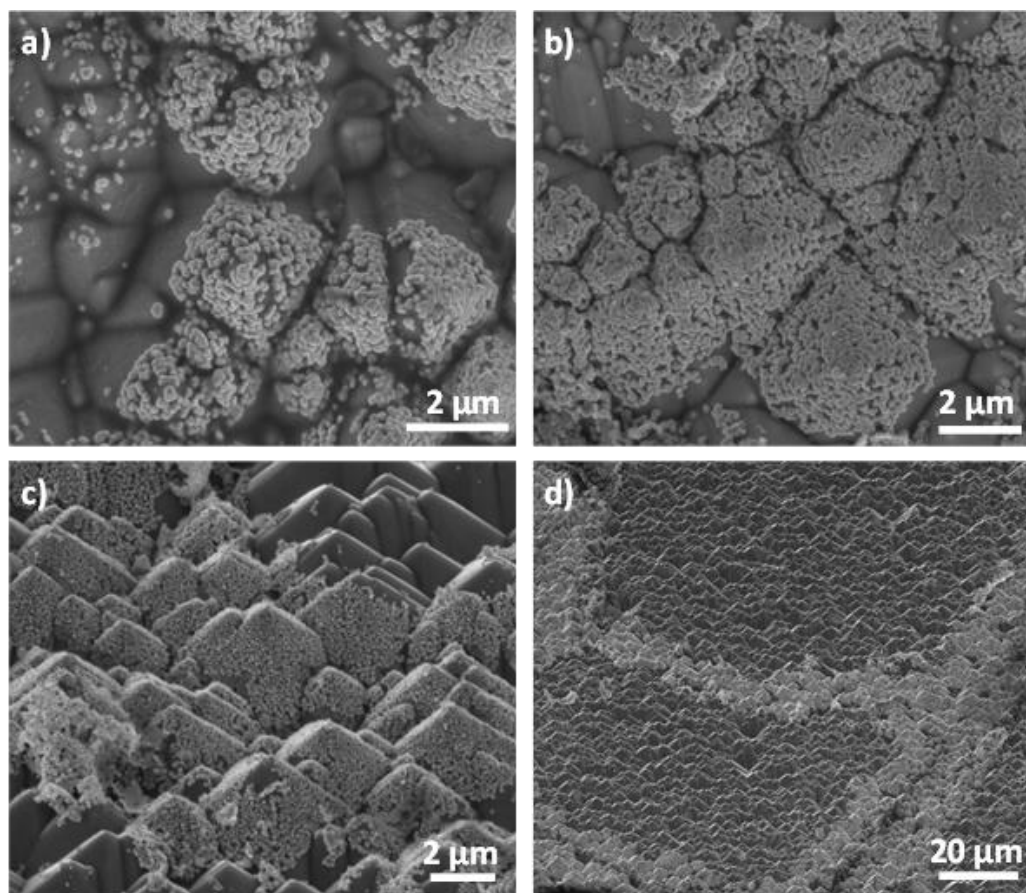

Figure 3.1.14 High resolution SEM images of light trapping nanostructures in Ni network coated Si solar cell where a), b) are top view and c) and d) are tilt view in different magnifications.

the light trapping nanostructures formed by the electroless deposition (see Figure 3.1.14) and the narrow Ni wires give rise to increased photo-absorption. Therefore, electrolessly deposited Ni network by crackle lithography can be conveniently employed as an alternative to conventionally made screen printed Ag electrode which not only increases the efficiency but is also highly inexpensive to fabricate. A simple estimation based on metal costs and fill factors shows that Ni electrodes should be at least two orders less expensive than the equivalent Ag electrodes (see Note 3.1.1).

3.1.4.3 Improving efficiency of commercial Si solar cell

The fabrication process of Si solar cells has been industrialized and in a commercial product, it is very difficult to incorporate or replace a fabrication step. Also, usually the cells are fully fabricated in one industry and then sent for panel fabrication in different industries. Therefore, it is difficult to get hold of prefinished cells and then deposit metal mesh on them to increase the efficiency. With this in mind, the fabrication of metal mesh was carried out on fully fabricated cells to achieve better efficiency. The commercial Si solar cell has a back electrode made up of Al, with Ag patches in order to connect with external circuits with the help of soldering. Then they have p-type Si and n-type Si layers with corrugation, covered with an anti-reflection coating of silicon nitride and finally have screen printed Ag electrodes (see Figure 3.1.15). As has been shown in the top-view schematic, the Ag electrodes usually consist of two busbars and several fingers perpendicular to the busbars which are ~ 3 mm apart. As the mean free path of the charge carriers before they recombine is 100 μm,
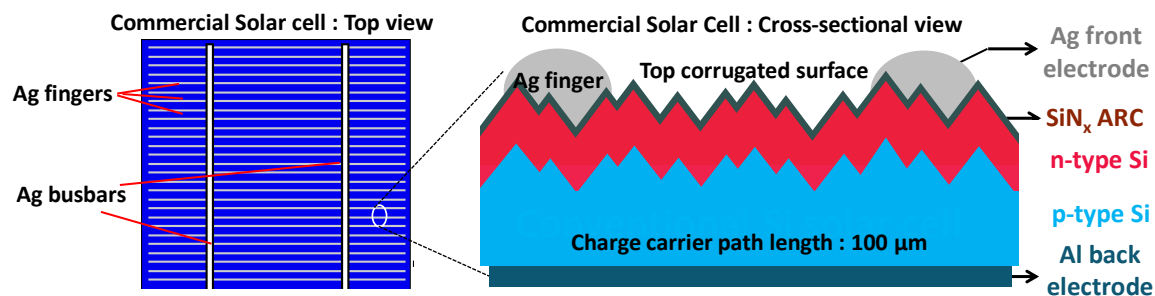
Figure 3.1.15 Top view (left) and cross-sectional view (right) of Commercial Si solar cell.

there is enough scope to increase the charge collection by introducing metal mesh in the area between the fingers. Also, as there is nitride coating on the top of Si, there should be some way to contact the metal mesh with the Si underneath. For this purpose a nitride coated Si substrate was taken and the nitride layer was tried to be etched away selectively by crack templating it and putting it BHF solution so that, in the cracks, Si is exposed to be finally deposited with metal mesh. 50% BHF gives selective etching, however, etching the corrugated surface of Si solar cell with the Ag fingers not getting affected needs further experiments. Therefore, a complete solution process for bringing an efficient metal mesh on a commercial Si solar cell is outside the scope of this work.
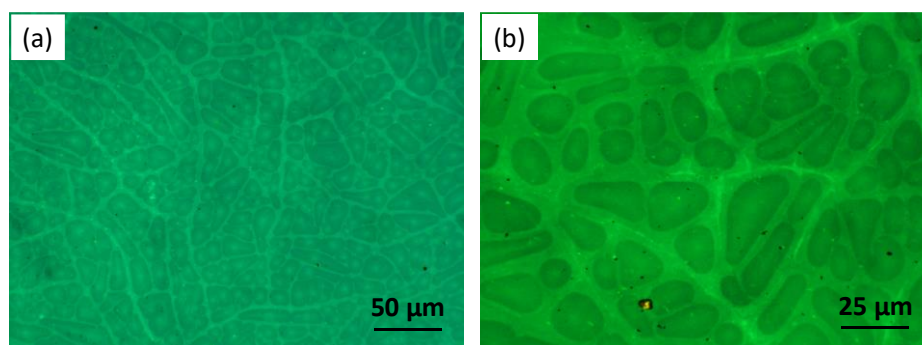
Figure 3.1.16 Optical micrographs of selectively etched silicon nitride layers on Si surface.

To improve the efficiency of commercial Si solar cells, cells were procured from three different sources (BHEL Bangalore, IIT Bombay, ENF solar Hyderabad) and were cut into small pieces. As the cells have Ag electrodes on top, it is not possible to always cut them into square shape. Also, it was not easy to make Ag paste contacts before depositing the metal mesh and then again making identical contacts without breaking the cell, after removing the metal mesh. For this purpose, a measurement set up was prepared (see Figure 3.1.17a). The measurement set up is made of Teflon which is unaffected by acetone. It has a Cu plate for making back contact, at the back side of which two Cu wires are contacted by soldering for external circuits. The front contacts are made by Cu foils on two opposite ends, which can be tightened using a screw. The contacts were made strong by tightening the screw of the holder with white teflon cap. To measure the area of cells having irregular shapes, a graph was drawn on a PET sheet. To measure the area, the full squares are counted, and the incomplete squares were halved and added to get the final area. The measurement was done by four-terminal sensing using Keithley 2300, in order to eliminate the resistance of leads.

A Si solar cell wafer was cut into small squares having area in the range 5 – 10 cm². The cells were cleaned by consecutively sonicating in isopropyl alcohol and water, followed by drying, by purging nitrogen. Solar cell parameters were measured for the pristine cells. An acrylic resin crackle precursor (CP) was mixed with diluter in the concentration 0.4 mg/mL and drop coated (10 µL/cm²) on the cut Si solar cell pieces.
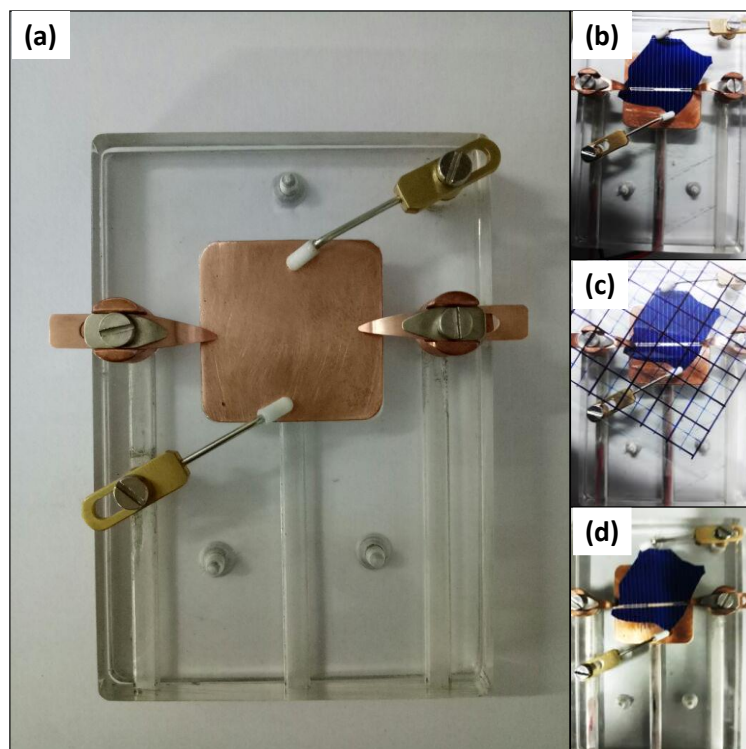
Figure 3.1.17 (a) Commercial solar cell measurement setup with Cu plate for back contact connected with a groove to insert back contact wire, two holders to make the cell stay in place, two top contacts made up of Cu foils in order to take four point contact. A commercial cell placed on the measurement set up (b) before bringing metal mesh, (c) before bringing metal mesh with area measuring transparent PET sheet and (d) after bringing metal mesh.

After drying in ambient condition, the CP coated Silicon solar cell was deposited with a thin coating of Ni (30 - 40 nm) by thermal evaporation. The CP was lifted off by dissolving in chloroform. The seed layer of Ni forming a highly interconnected network was annealed for 5 s at 420 °C in the ambient on the hot plate. Changing the time or temperature of annealing drastically reduced the efficiency of the cells. The Ni network is just adding to the shadowing by reducing the area of Silicon solar cell
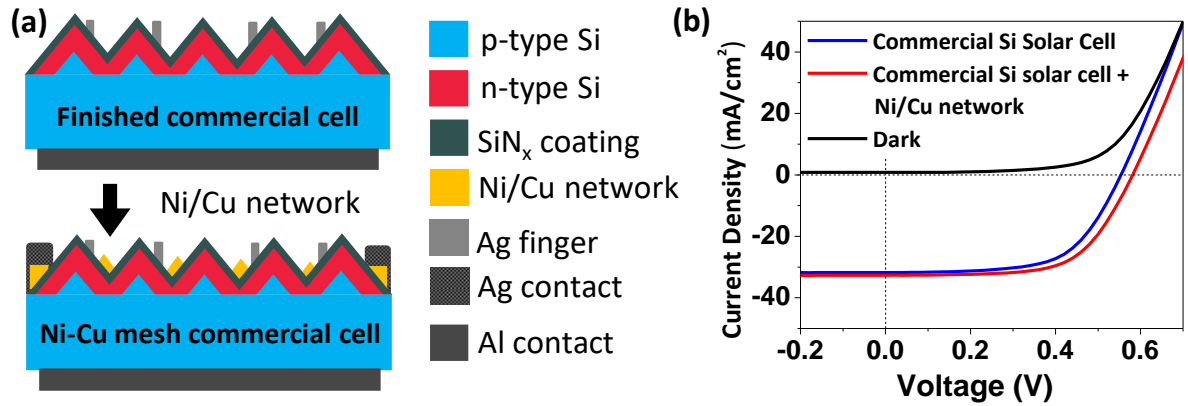
Figure 3.1.18 (a) Schematic of commercial Si solar cell before (top) and after (bottom) depositing Ni/Cu network by crackle lithography. IV characterization of commercial cells with and without Ni network.
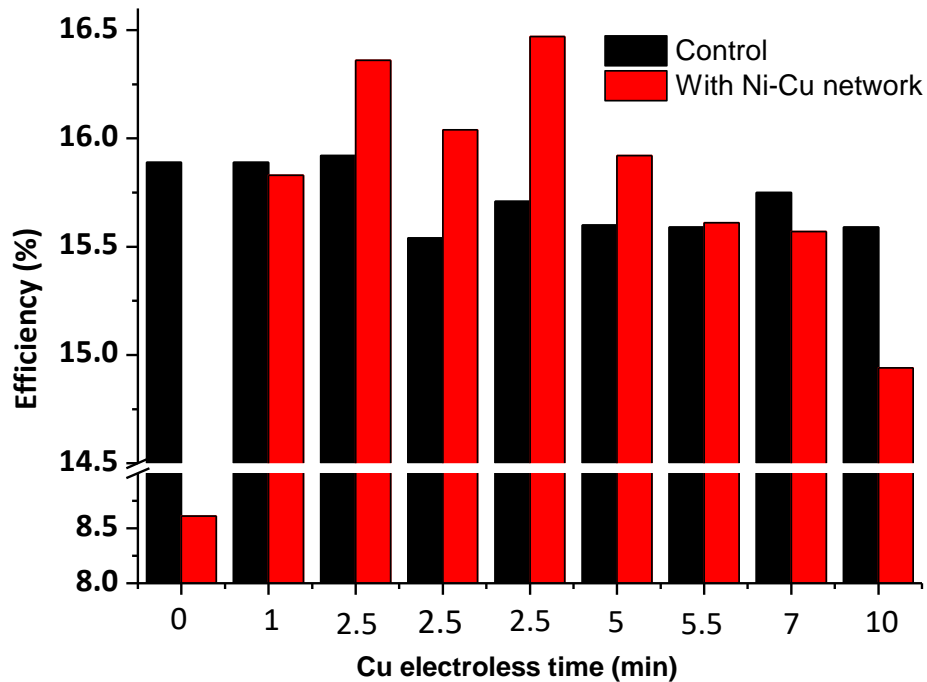
Figure 3.1.19 Optimization of Cu electroless deposition duration after deposition of Ni.

helping in photo-absorption, without adding to the current collection. To help in conduction through the wire network for current collection, Cu is electrolessly grown

on top of Ni network for various durations of time in Cu plating bath i.e. 10:1 ratio of Solution A (3 g of $CuSO_4$, and 14 g of sodium potassium tartrate mixed with 4 g of NaOH in 100 ml of distilled water) and Solution B (formaldehyde solution). Emery paper is rubbed on the edges to remove any Copper grown on the edges of as prepared Ni-Copper wire coated Silicon solar cells. The cells were connected with four Copper wires as done for control measurements to measure their solar cell parameters. Figure 3.1.18a shows the schematic of a commercial Si solar cell before and after deposition of the Ni/Cu wire. Copper electroless deposition time varied from 0 minutes to 10 minutes and it was found that the efficiency enhancement was maximum for Copper deposition of 2.5 minutes (see Figure 3.1.19), the J-V characteristic of which is shown in Figure 3.1.18b compared with the control. If the deposition is less than 2.5 minutes, the Ni/Cu wires are not conducting enough to pass the current and if the deposition is for longer duration, the Cu starts depositing on the sides of Ni wires as well, increasing the shadowing area and thus decreasing the absorption of photons. To further validate the results, cells from three different sources were used and were deposited with the Ni/Cu wire network to compare their performance. Figure 3.1.20 shows statistics of efficiency increment in 22 devices. All the cells show some improvement confirming that the process is generic and does not depend on the source. The source 2 is showing less efficiency increment because the control cells have appreciable efficiencies already, leaving less scope for further improvement.

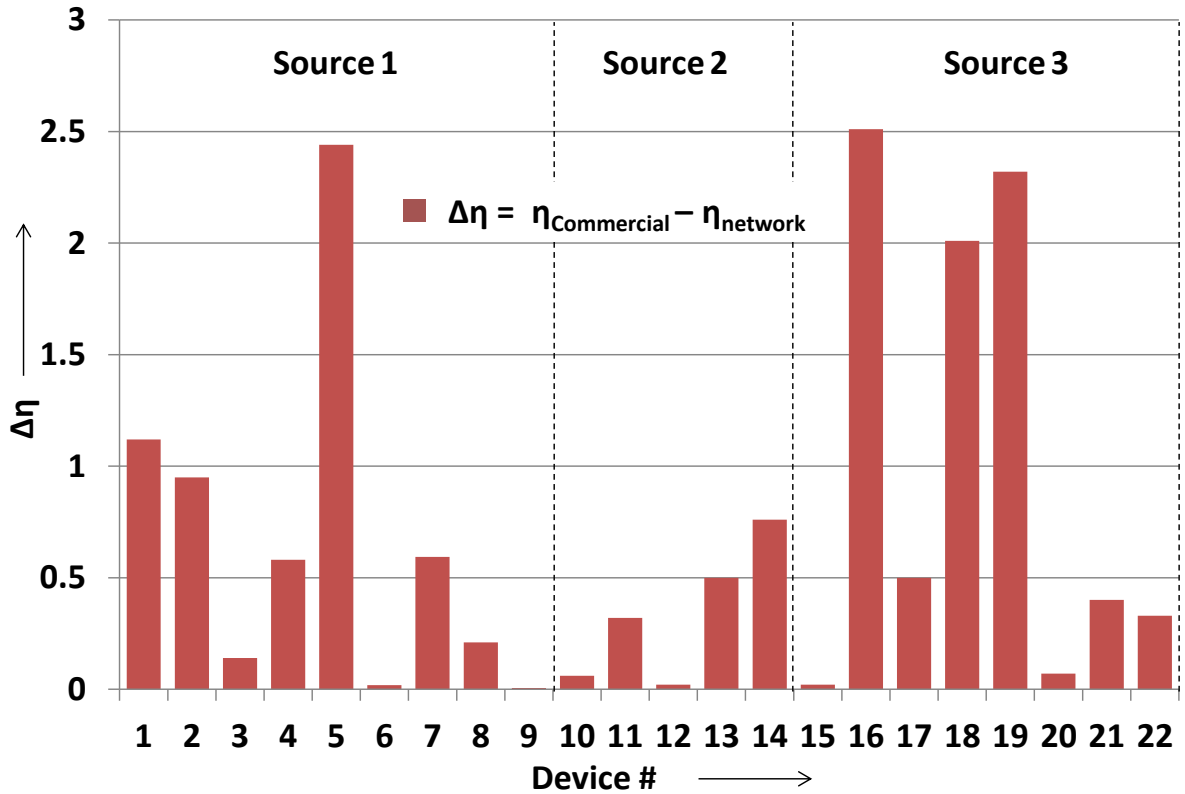**Figure 3.1.20** Statistics of efficiency increment in 22 cells from three different sources.
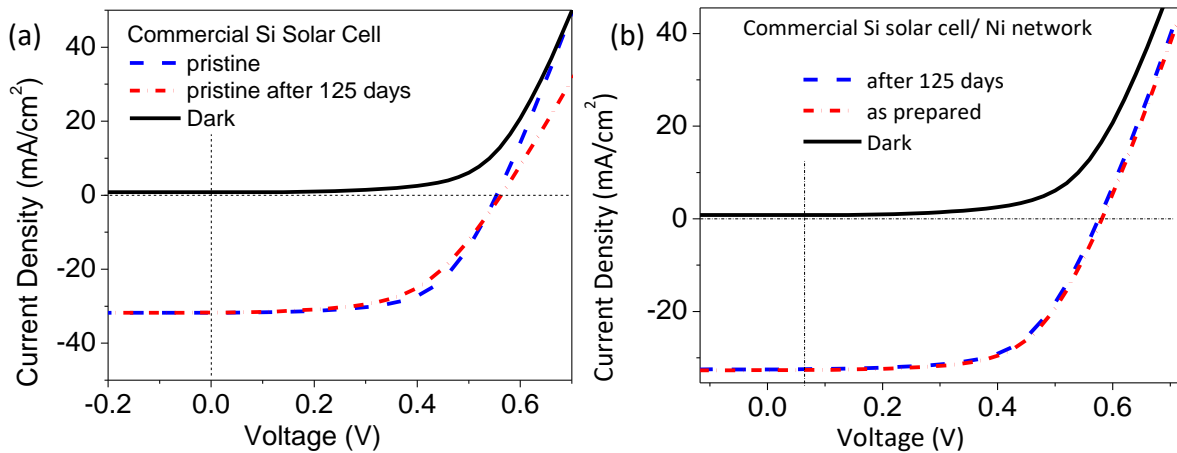
Figure 3.1.21 Stability of commercial solar cell in ambient condition. IV characteristic of (a) pristine and (b) cell with Ni/Cu network, as prepared and after keeping in ambient for 125 days.

Table 3.1.4 Performance parameters of Commercial Si solar cell with and without Ni-Copper wire network.

Standard Si solar cell with Ag electrodes and SiN$_x$ coating	Without Ni-Cu wire network		With Ni-Cu wire network	
Time in ambient conditions	As obtained	After 125 days	As prepared	After 125 days
Annealing time at 420°C (s)	0	0	30	30
Cu electroless time (min)	0	0	5.5	5.5
Area (cm²)	0.72	0.72	1.125	1.125
V$_{oc}$(V)	0.55	0.56	0.581	0.576
J$_{sc}$ (mA/cm²)	31.77	31.72	32.68	32.51
FF (%)	61.92	56.31	63.18	62.95
Efficiency (%)	10.89	10.05	12.01	11.79

To analyse the stability of Silicon solar cells after coating with Ni-Cu network, an aging test was performed by measuring the efficiency of a cell grown with Ni-Cu network on a regular basis. Figure 3.1.21a shows the J-V characteristics of a typical commercial Silicon solar cell after keeping it in ambient for 125 days. As clear from the curve shapes, the curve loses squareness (shown by FF comparison in the Table 3.1.3) as the cell ages, indicating degradation in the performance. Figure 3.1.21b shows the J-V characteristics of Silicon solar cells with Ni-Cu wire network on aging for 125 days. The blue curve (after 125 days) barely loses its shape and almost overlaps the curve (as prepared) indicating higher stability of this cell when compared to the pristine commercial Si solar cell. The Table 3.1.4 compares the performance parameters of pristine as well as that coated with Ni-Cu commercial Si solar cell before and after aging. The efficiency decrease is 7.7% for pristine compared to only 1.8% in the one with Ni-

Cu network. Therefore, metal wire network not only serves as a cost-effective substitute but also works to improve performance when brought in addition to the commercial screen-printed electrodes.

3.1.5 Conclusions

This study has successfully demonstrated the possibility of using a metal wire network as front electrode for crystalline Si solar cells, in place of the conventional silver finger patterns deposited using screen printing. The efficacy of the method was first examined on a bare Si wafer by electroless depositing an Au wire network using a crackle template. The inherent photoconductivity of Si was found enhanced by an order in presence of the fine wire network (widths < 2 μm, thickness ~ 200 nm) serving as current collecting grid, which also led to reduction in the reflectivity by 15%. Crackle lithographic technique was found to be effective also on highly rough surfaces of the Si solar cells. The Ni wire network acting as a top electrode for a prefinished cell showed an enhancement in efficiency of 20% compared to cells from the same batch with the silver finger electrodes. The former exhibited a respectable fill factor of 65.45% and a current density of 33.28 mAcm^{-2}. The electrolessly grown Ni wire network by crackle lithography holds great promise in replacing the conventional screen-printed silver top electrodes, making crystalline Si solar cell fabrication easier and even more cost effective. Ni-Cu metal network was deposited on commercial Si solar cell by first depositing Ni seed layer using thermal evaporation and then growing Cu electrolessly,

to show 10.3% increment in efficiency. The cells also become stable after the Ni-Cu network incorporation.

3.1.6 References

1.   Saga, T., Advances in crystalline silicon solar cell technology for industrial mass production. *NPG Asia Mater.* **2010,** *2* (3), 96-102.

2.   Beaucarne, G.; Schubert, G.; Hoornstra, J.; Horzel, J.; Glunz, S. W., Summary of the Third Workshop on Metallization for Crystalline Silicon Solar Cells. *Energy Procedia* **2012,** *21*, 2-13.

3.   Green, M. A.; Ho-Baillie, A.; Snaith, H. J., The emergence of perovskite solar cells. *Nat. Photon.* **2014,** *8* (7), 506-514.

4.   Liu, M. Z.; Johnston, M. B.; Snaith, H. J., Efficient planar heterojunction perovskite solar cells by vapour deposition. *Nature* **2013,** *501* (7467), 395-398.

5.   Zhou, H. P.; Chen, Q.; Li, G.; Luo, S.; Song, T. B.; Duan, H. S.; Hong, Z. R.; You, J. B.; Liu, Y. S.; Yang, Y., Interface engineering of highly efficient perovskite solar cells. *Science* **2014,** *345* (6196), 542-546.

6.   Li, W. W.; Hendriks, K. H.; Wienk, M. M.; Janssen, R. A. J., Diketopyrrolopyrrole Polymers for Organic Solar Cells. *Acc. Chem. Res.* **2016,** *49* (1), 78-85.

7.   Facchetti, A., Polymer donor-polymer acceptor (all-polymer) solar cells. *Mater. Today* **2013,** *16* (4), 123-132.

8.   Hunger, C.; Rao, K. D. M.; Gupta, R.; Singh, C. R.; Kulkarni, G. U.; Thelakkat, M., Transparent Metal Network with Low Haze and High Figure of Merit applied to Front

and Back Electrodes in Semitransparent ITO-free Polymer Solar Cells. *Energy Technol.* **2015,** *3* (6), 638-645.

9. Gur, I.; Fromer, N. A.; Geier, M. L.; Alivisatos, A. P., Air-stable all-inorganic nanocrystal solar cells processed from solution. *Science* **2005,** *310* (5747), 462-465.

10. Habas, S. E.; Platt, H. A. S.; van Hest, M. F. A. M.; Ginley, D. S., Low-Cost Inorganic Solar Cells: From Ink To Printed Device. *Chem. Rev.* **2010,** *110* (11), 6571-6594.

11. Shejale, K. P.; Laishram, D.; Sharma, R. K., High-performance dye-sensitized solar cell using dimensionally controlled titania synthesized at sub-zero temperatures. *RSC Adv.* **2016,** *6* (28), 23459-23466.

12. Nozik, A. J., Quantum dot solar cells. *Physica E-Low-Dimens. Syst. Nanostruct.* **2002,** *14* (1-2), 115-120.

13. Chuang, C. H. M.; Brown, P. R.; Bulovic, V.; Bawendi, M. G., Improved performance and stability in quantum dot solar cells through band alignment engineering. *Nat. Mater.* **2014,** *13* (8), 796-801.

14. Kamat, P. V., Quantum Dot Solar Cells. The Next Big Thing in Photovoltaics. *J. Phys. Chem. Lett.* **2013,** *4* (6), 908-918.

15. Huynh, W. U.; Dittmer, J. J.; Alivisatos, A. P., Hybrid nanorod-polymer solar cells. *Science* **2002,** *295* (5564), 2425-2427.

16. Wenham, S. R.; Green, M. A., Silicon solar cells. *Prog. Photovoltaics* **1996,** *4* (1), 3-33.

17. Oh, J.; Yuan, H. C.; Branz, H. M., An 18.2%-efficient black-silicon solar cell achieved through control of carrier recombination in nanostructures. *Nat. Nanotechnol.* **2012,** *7* (11), 743-748.

18. Savin, H.; Repo, P.; von Gastrow, G.; Ortega, P.; Calle, E.; Garin, M.; Alcubilla, R., Black silicon solar cells with interdigitated back-contacts achieve 22.1% efficiency. *Nat. Nanotechnol.* **2015,** *10* (7), 624-628.

19. Untila, G. G.; Kost, T. N.; Chebotareva, A. B.; Zaks, M. B.; Sitnikov, A. M.; Solodukha, O. I.; Shvarts, M. Z., Bifacial concentrator Ag-free crystalline n-type Si solar cell. *Prog. Photovoltaics* **2015,** *23* (5), 600-610.

20. Lee, Y.; Park, C.; Balaji, N.; Lee, Y. J.; Dao, V. A., High-efficiency Silicon Solar Cells: A Review. *Isr. J. Chem.* **2015,** *55* (10), 1050-1063.

21. Rudolph, D.; Olibet, S.; Hoornstra, J.; Weeber, A.; Cabrera, E.; Carr, A.; Koppes, M.; Kopecek, R., Replacement of silver in silicon solar cell metallization pastes containing a highly reactive glass frit: Is it possible? *Proceedings of the Fourth Workshop on Metallization for Crystalline Silicon Solar Cells* **2013,** *43,* 44-53.

22. Kim, N.; Um, H. D.; Choi, I.; Kim, K. H.; Seo, K., 18.4%-Efficient Heterojunction Si Solar Cells Using Optimized ITO/Top Electrode. *ACS Appl. Mater. Inter.* **2016,** *8* (18), 11412-11417.

23. Drabczyk, K.; Panek, P., Influence of screen printing parameters on the front metallic electrodes geometry of solar cells. *Circuit World* **2014,** *40* (1), 23-26.

24. Horteis, M.; Glunz, S. W., Fine Line Printed Silicon Solar Cells Exceeding. *Prog. Photovoltaics* **2008,** *16* (7), 555-560.

25. Teng, K. F.; Vest, R. W., Application of Ink Jet Technology on Photovoltaic Metallization. *IEEE Electron Device Lett.* **1988,** *9* (11), 591-593.

26. Raabe, B.; Huster, F.; McCann, M.; Fath, P. In *High aspect ratio screen printed fingers*, 20th European Photovoltaic Solar Energy Conference, WIP Renewable Energies Barcelona, Spain: **2005**; pp 931-933.

27. Hannebauer, H.; Dullweber, T.; Falcon, T.; Brendel, R., Fineline printing options for high efficiencies and low Ag paste consumption. *Proceedings of the 3rd International Conference on Crystalline Silicon Photovoltaics (Siliconpv 2013)* **2013,** *38,* 725-731.

28. Chen, X.; Church, K.; Yang, H.; Cooper, I. B.; Rohatgi, A. In *Improved front side metallization for silicon solar cells by direct printing*, Proc. 37th IEEE PVSC, IEEE: **2011**; pp 003667-003671.

29. Mette, A.; Richter, P.; Hörteis, M.; Glunz, S., Metal aerosol jet printing for solar cell metallization. *Prog. Photovoltaics Res. Appl.* **2007,** *15* (7), 621-627.

30. Zhao, J. H.; Wang, A. H.; Altermatt, P. P.; Wenham, S. R.; Green, M. A., 24% efficient PERL silicon solar cell: Recent improvements in high efficiency silicon cell research. *Sol. Energ. Mater. Sol. Cells* **1996,** *41-2,* 87-99.

31. Glunz, S. W.; Knobloch, J.; Hebling, C.; Wettling, W., The range of high-efficiency silicon solar cells fabricated at Fraunhofer ISE. *Ieee Phot Spec Conf* **1997**, 231-234.

32. Cui, T.; Lv, R.; Huang, Z.-H.; Chen, S.; Zhang, Z.; Gan, X.; Jia, Y.; Li, X.; Wang, K.; Wu, D., Enhanced efficiency of graphene/silicon heterojunction solar cells by molecular doping. *J. Mater. Chem. A* **2013,** *1* (18), 5736-5740.

33. Li, X. M.; Zhu, H. W.; Wang, K. L.; Cao, A. Y.; Wei, J. Q.; Li, C. Y.; Jia, Y.; Li, Z.; Li, X.; Wu, D. H., Graphene-On-Silicon Schottky Junction Solar Cells. *Adv. Mater.* **2010,** *22* (25), 2743-2748.

34. Jeong, S.; Garnett, E. C.; Wang, S.; Yu, Z. G.; Fan, S. H.; Brongersma, M. L.; McGehee, M. D.; Cui, Y., Hybrid Silicon Nanocone-Polymer Solar Cells. *Nano Lett.* **2012,** *12* (6), 2971-2976.

35. Wang, H.; Wang, J.; Rusli, Hybrid Si nanocones/PEDOT: PSS solar cell. *Nanoscale Res Lett* **2015,** *10* (1), 1-8.

36. Tune, D. D.; Flavel, B. S.; Krupke, R.; Shapter, J. G., Carbon Nanotube-Silicon Solar Cells. *Adv. Energy Mater.* **2012,** *2* (9), 1043-1055.

37. Miao, X. C.; Tongay, S.; Petterson, M. K.; Berke, K.; Rinzler, A. G.; Appleton, B. R.; Hebard, A. F., High Efficiency Graphene Solar Cells by Chemical Doping. *Nano Lett.* **2012,** *12* (6), 2745-2750.

38. Shi, E. Z.; Li, H. B.; Yang, L.; Zhang, L. H.; Li, Z.; Li, P. X.; Shang, Y. Y.; Wu, S. T.; Li, X. M.; Wei, J. Q.; Wang, K. L.; Zhu, H. W.; Wu, D. H.; Fang, Y.; Cao, A. Y., Colloidal Antireflection Coating Improves Graphene-Silicon Solar Cells. *Nano Lett.* **2013,** *13* (4), 1776-1781.

39. Polat, E. O.; Balci, O.; Kakenov, N.; Uzlu, H. B.; Kocabas, C.; Dahiya, R., Synthesis of Large Area Graphene for High Performance in Flexible Optoelectronic Devices. *Sci. Rep.* **2015,** *5*.

40. Jia, Y.; Cao, A. Y.; Bai, X.; Li, Z.; Zhang, L. H.; Guo, N.; Wei, J. Q.; Wang, K. L.; Zhu, H. W.; Wu, D. H.; Ajayan, P. M., Achieving High Efficiency Silicon-Carbon Nanotube Heterojunction Solar Cells by Acid Doping. *Nano Lett.* **2011,** *11* (5), 1901-1905.

41. Shi, E. Z.; Zhang, L. H.; Li, Z.; Li, P. X.; Shang, Y. Y.; Jia, Y.; Wei, J. Q.; Wang, K. L.; Zhu, H. W.; Wu, D. H.; Zhang, S.; Cao, A. Y., TiO2-Coated Carbon Nanotube-Silicon Solar Cells with Efficiency of 15%. *Sci. Rep.* **2012,** *2,* 1-5.

42. Angmo, D.; Krebs, F. C., Flexible ITO-Free Polymer Solar Cells. *J. Appl. Polym. Sci.* **2013,** *129* (1), 1-14.

43. Rao, K. D. M.; Hunger, C.; Gupta, R.; Kulkarni, G. U.; Thelakkat, M., A cracked polymer templated metal network as a transparent conducting electrode for ITO-free organic solar cells. *Phys. Chem. Chem. Phys.* **2014,** *16* (29), 15107-15110.

44. Alturaif, H. A.; Alothman, Z. A.; Shapter, J. G.; Wabaidur, S. M., Use of Carbon Nanotubes (CNTs) with Polymers in Solar Cells. *Molecules* **2014,** *19* (11), 17329-17344.

45. Mette, A.; Pysch, D.; Emanuel, G.; Erath, D.; Preu, R.; Glunz, S., Series resistance characterization of industrial silicon solar cells with screen-printed contacts using hotmelt paste. *Prog. Photovoltaics Res. Appl.* **2007,** *15* (6), 493-505.

46. Khatri, I.; Hoshino, A.; Watanabe, F.; Liu, Q. M.; Ishikawa, R.; Ueno, K.; Shirai, H., Self-assembled silver nanowires as top electrode for poly(3,4-ethylenedioxythiophene): poly(stylenesulfonate)/n-silicon solar cell. *Thin Solid Films* **2014,** *558,* 306-310.

47. Chen, T. G.; Huang, B. Y.; Liu, H. W.; Huang, Y. Y.; Pan, H. T.; Meng, H. F.; Yu, P. C., Flexible Silver Nanowire Meshes for High-Efficiency Microtextured Organic-Silicon Hybrid Photovoltaics. *ACS Appl. Mater. Inter* **2012,** *4* (12), 6856-6863.

48. Jorgensen, M.; Norrman, K.; Krebs, F. C., Stability/degradation of polymer solar cells. *Sol. Energ. Mater. Sol. Cells* **2008,** *92* (7), 686-714.

49. Raval, M. C.; Solanki, C. S., Characterization of electroless nickel as a seed layer for silicon solar cell metallization. *Bull Mater. Sci.* **2015,** 38(1), 197-201

50. Rao, K. D. M.; Gupta, R.; Kulkarni, G. U., Fabrication of Large Area, High-Performance, Transparent Conducting Electrodes Using a Spontaneously Formed Crackle Network as Template. *Adv. Mater. Inter.* **2014,** *1* (6), 1-7.

51. Rao, K. D. M.; Kulkarni, G. U., A highly crystalline single Au wire network as a high temperature transparent heater. *Nanoscale* **2014,** *6* (11), 5645-5651.

52. Gupta, R.; Rao, K. D. M.; Kulkarni, G. U., Transparent and flexible capacitor fabricated using a metal wire network as a transparent conducting electrode. *RSC Adv.* **2014,** *4* (59), 31108-31112.

53. Goehring, L.; Nakahara, A.; Dutta, T.; Kitsunezaki, S.; Tarafdar, S., Patterns of Crack Networks in Homogeneous Media. *Desiccation Cracks and their Patterns*, 145-205.

54. Cai, J. G.; Qi, L. M., Recent advances in antireflective surfaces based on nanostructure arrays. *Mater. Horiz.* **2015,** *2* (1), 37-53.

55. Liu, Y. S.; Ji, G. B.; Wang, J. Y.; Liang, X. Q.; Zuo, Z. W.; Shi, Y., Fabrication and photocatalytic properties of silicon nanowires by metal-assisted chemical etching: effect of H_2O_2 concentration. *Nanoscale Res Lett* **2012,** 7, 663-672.

56. Wu, K. H.; Li, C. W., Light Absorption Enhancement of Silicon-Based Photovoltaic Devices with Multiple Bandgap Structures of Porous Silicon. *Materials* **2015,** *8* (9), 5922-5932.

57. Boumaour, M.; Sali, S.; Bahfir, A.; Kermadi, S.; Zougar, L.; Ouarab, N.; Larabi, A., Numerical Study of TCO/Silicon Solar Cells with Novel Back Surface Field. *J. Electron. Mater.* **2016,** *45* (8), 3929-3934.

58. Raval, M. C.; Solanki, C. S., Review of Ni-Cu based front side metallization for c-Si solar cells. *J. Sol. Energy* **2013,** *2013*.

59. Graff, K., *Metal impurities in silicon-device fabrication*. Springer Science & Business Media: **2013**; Vol. 24.

60. Williams, E. W., Gold in solar cells. *Gold Bulletin* **1980,** *13* (3), 90-97.

61. Delalamo, J. A.; Swanson, R. M., Modeling of Minority-Carrier Transport in Heavily Doped Silicon Emitters. *Solid-State Electron.* **1987,** *30* (11), 1127-1136.

62. Kumar, A., Predicting efficiency of solar cells based on transparent conducting electrodes. *J. Appl. Phys.* **2017,** *121*(1), 014502.

Chapter 3.2

A Cosmetically Adaptable Transparent Strain Sensor

for Sensitively Delineating Patterns in Small

Movements of Vital Human Organs

Summary: In this chapter, the fabrication of a wearable strain sensor made of an Au micromesh partially embedded in polydimethylsiloxane (PDMS) substrate is described. The sensor exhibits a high optical transmittance of 85%. The sensor has a gauge factor of over 10^8 for a strain range of 0.02% to 4.5%. *In situ* scanning electron imaging and infrared thermal microscopy analysis have revealed that nanometric break junctions form throughout the wire network under strain; strain increases the number of such junctions, leading to a large change in the sheet resistance of the mesh. The wire segments break successively with increasing strain and resistance increases linearly for lower values of strain and non-linearly at higher values of strain due to formation of current bottlenecks. These experimental findings lend support from computational studies. The semi-embedded nature of these Au microwires allow the broken wires to retract to the original positions, thus closing the nanogaps and regaining the original low resistance state. High repeatability as well as cyclic stability have been demonstrated in live examples involving human body activity, importantly while

mounting the sensor in strategic remote locations away from the most active site where strains are highest. The instantaneous formation of numerous nanometric break-junctions was utilized to observe field evaporation at applied voltages, later confirmed by scanning electron microscopy.

3.2.1 Introduction

There is a growing demand for multi-functional wearable electronic devices[1-3] in the context of smart textiles,[4-6] soft robotics,[7,8] roll-up displays[9] and electronic skins.[10,11] Integrating the device with the human body, internally or externally, places certain requirements on device architecture[12] and therefore, sensors must be designed to be ergonomic.[13,14] Typically wearable sensors can monitor temperature, sweat, expressions and movements. The latter is monitored using strain sensors which measure mechanical deformations in an object via change in the property of the sensor element, expressed as the gauge factor for a given strain. While sensors based on optical properties are in use,[15] electrical resistance or capacitance-based sensors have the advantage of easy integration.[16,17] Although these sensors are built to work with a high strain, even larger than 100%, high sensitivity (gauge factor $> 10^4$) is achieved typically at lower strains (~2%).[18] Considering large movements typically associated with body parts, a wearable sensor operable at lower strains is often sufficient. Conversely, because of lower sensitivity and possible damage due to the range of movement, measurements aimed at higher strains are not favorable. Instead, a sensor of high sensitivity can be mounted in a strategic position on a muscle controlling the movement where the displacements are reduced in magnitude yet representative of the movement of

interest. Thus, for example, eye movements are accurately reflected at the canthus[19] away from the eyeball, and similarly, the nerve movements at the opisthenar are reduced versions of the actions carried out by fingers.[20] In this way not only the sensor can be concealed but its life is prolonged because of the reduced exposure to outside agents. Thus, there is greater emphasis on sensors with high sensitivity working at low strain ranges (<5%).[21]

Conventional strain sensors made of metals with wavy or spring geometries exhibit poor strain sensing because of low gauge factors of approximately 1 to 5.[22] An alternative approach is to fabricate strain sensors that incorporate nanomaterials with large aspect ratios exhibiting extraordinary mechanical and electrical properties. For example, strain sensors with improved performance have been realized with carbon threads[23] and graphene.[24] Although such sensors offer desired strain range and sensitivity, the sensing area is typically limited to a few mm^2. For application on body parts, sensor areas in the range of a few cm^2 would minimize ambiguity in placement and ensure longevity, which is crucial for wearable devices.[25] The present work addresses such design issues. Another desirable property is the optical transparency of the device as it provides an extra degree of freedom for integration on an exposed body part. Several transparent strain sensors have been realized covering certain strain ranges (see Table 3.2.1) that include active elements based on ZnO nanowires,[26] carbon nanotubes,[27] graphene[28] and In$_2$Se$_3$ nanosheets.[29] Although Ag nanowire networks and graphene are known for their visible transparency, the associated strain sensors made of them demand thicker active layers that in the end, render the device opaque. Recently, spray coated carbon

nanotubes embedded in PDMS were used for the fabrication of a capacitive strain sensor, where the active material is transparent but the use of two such films makes it appear semitransparent.[30,31]

Table 3.2.1 Literature of high-performance transparent strain sensors. (R: Resistive, C: Capacitive, Mod.: Moderate, V. low: Very low).

Sr. no	Gauge factor	Strain values (%)	T (%)	Hyste -resis	Resp. time (ms)	Type	Material used	Reference
1	2- 14	~ 70	--	High	-	R	AgNW's with PDMS	*ACS Nano,* **2014**, *8,* 5154-5163
2	10^3	2 – 6	--	-	-	R	Graphene with PDMS	*Sci. Rep.,* **2012**, *2,* 870
	10^6	> 7				R		
3	11.5	≤ -2	--	Mod.	100	R	Pt coated, polymeric nanofibers, on PDMS	*Nat. Mater.,* **2012**, *11,* 795-801.
	0.75	≤ -4				R		
	8.53	≤ -5				R		
4	20	~ 35	--	V. low	-	R	Ag NW with PDMS	*Nano Lett.,* **2015**, *15,* 5240-5247
5	2×10^4	~ 100	--	-	-	R	CNT and graphene with PDMS	*ACS Appl. Mater. Interfaces,* **2015**, *7,* 4463-4470
6	10^3	2-6	--	-	-	R	GWFs on PDMS	*Adv. Funct. Mater.,* **2014**, *24,* 4666-4670
	10^6	>7				R		
	35	0.2				R		
7	0.7	~ 50	--	V. low	40	C	AgNW and PDMS	*Nanoscale,* **2014**, *6,* 2345-2352
8	62	~100	62	-	-	R	SWNT and PU	*ACS Nano,* **2015**, *9,* 6252-6261
9	12.4	~100	75	Low	-	R	AgNW	*ACS Nano,* **2015**, *9,* 8801-8810
10	27.8	0 – 40	--	Mod.	-	R	Piezoresistive interlocked microdome arrays	*ACS Nano,* **2014**. *8,* 12020-12029
	1084	40 - 90				R		
	9617	90 - 120				R		
11	0.56	0- 200	--	-	12	R	CNT fibre	*ACS Nano,* **2015**, *9,* 5929-5936
12	30	0.2	--	-	-	R	Piezoresistive doped Nano crystalline Si	*Non-Crystalline Solids,* **2008**, *354,* 2585-2589.
13	20	3	--	-	-	R	Si nanowire	*ACS Nano,* **2011**, *5,* 1556-1563
14	1250	1.2	--	-	10	R	ZnO nanowire	*Nano Lett,* **2008**, *8,* 3035-3040
15	6.7×10^8	1.4	--	-	≤ 100	R	ZnO nanorod	*J. Phys. Chem. C,* **2011**, *115,* 570-575
16	10	1.5	--	-	-	R	Piezoresistive carbon Filament	*Smart Mater. Struct.,* **1996**, *5,* 243-246
17	75	2	--	Mod.	-	R	MWCNT/epoxy composite	*Nanotechnology,* **2008**, *19,* 475503
18	210	0.08	--	-	-	R	SWNT	*Nano Lett.,* **2006**, *6,* 233-237

19	269	0.24	--	-	-	R	SWNT	*Appl. Phys. Lett.*, **2008**, 92, 063501
20	290	0.22	--	-	-	R	Pd μ-strips	*ACS Appl. Mater. Interfaces*, **2011**, 3, 2173-2178
21	35	6	--	-	-	R	Graphene- rubber composite	*ACS Nano*, **2014**, 8, 8819-8830
22	0.99	100	--	High	-	R	CNT based percolation n/w	*Nano Lett.*, **2012**, 12, 1821-1825
23	3740	0.32	--	-	-	R	ZnSnO$_3$ nanowires/microwires	*ACS Nano*, **2012**, 6, 4369-4374
24	~ 1	300	90	V. Low	≤ 100	R	CNT	*Sci. Rep.*, **2013**, 3, 3048
25	0.82	0 - 40	--	-	14	R	SWNT	*Nat. Nanotechnol.*, **2011**, 6, 296-301
	0.06	60 - 200				R		
26	14	5-10	--	-	-	R	Nanocarbon Nanocomposites	*Sens. Actuator A-Phys.*, **2015**. 221, 33-40
27	2.35	0- 17	--	-	-	R	Cu NW ink	*ACS Appl. Mater. Interfaces*, **2015**, 7, 16760-16766
	13.17	18- 30	--			R		
	54.38	40 - 90	--			R		
28	100	50	6	Mod.	-	R	Ag NW on PDMS	*ACS Appl. Mater. Interfaces*, **2015**, 7, 13467-13475.
29	7.38	0-14	--	Low	≤ 17	R	Au NW PDMS	*Nat. Commun.*, **2014**. 5, 3132
	1.82	14-25	--			R		
30	60.6	~ 0.22	--	-	110	R	Graphite	*Adv. Funct. Mater.*, **2015**, 25, 2395-2401
	150.5	0.22 – 0.32	--			R		
	536.6	0.32- 0.62	--			R		
31	150	0.08 – 0.2	--	Mod.	-	R	VO$_2$ nano beam	*Adv. Mater.*, **2010**, 22, 5134
32	2.05	20	--	Low	1000	R	Ag NP on PDMS	*Nanoscale*, **2014**, 6, 11932-11939
33	1.5	1.75	--	Low	-	R	CNT	*Sensor Rev.*, **2014**, 34, 209-219
34	233.5	2	--	Mod.	-	R	Graphene PDMS composite	*Sci. Instrum.*, **2013**, 84, 105005.
35	389	0.05 – 0.12	--	--	--	C	Piezoelectric nano-generators and coplanar-gate graphene transistors.	*Adv. Mater.*, **2015**, 27, 3411-3417
36	7	50	--	Mod.	--	R	Graphene/AgNPs	*J. Mater. Chem. C*, **2016**, 4. 4304-4311
	476	500				R		
37	237	-0.5- 0.5	--	--	--	R	2D In$_2$Se$_3$ films	*Chem. Mater.*, **2016**, 28, 4278-4283
	92	0.5- 1.5				R		
38	12	410	--	Low	500	R	CNT-array double helix	*Sci. Rep.*, **2015**. 5, 15554
39	12	200	--			R	CNT	*ACS Appl. Mater. Interfaces*, **2015**. 7, 26195-26205
	25	530				R		

40	39	0.1-3	--	Low	--	R	CPC@PU yarn	*ACS Appl. Mater. Interfaces*, **2016**, 8. 9936-9945
41	0.045	0-85	--	Low	--	R	PANI/PVDF	*Nanoscale*, **2016**, 8, 2944-2950
	0.840	85- 110				R		
42	522.6	≥ 50	--	Mod.	--	R	Graphitic thin films on elastomer	*ACS Appl. Mater. Interfaces*, **2016**, 8, 618-5626
	11344	≤50						
43	2	0.15	--	-	-	R	Ni wire (commercial)	IPA Pvt Ltd, Bangalore (http://ipaindia.com/)
44	200-1100	0-2	67	V. low		R	DMSO doped PEDOT:PSS	*ACS Appl. Mater. Interfaces*, **2018**, 10, 3895-3901
45	1	300	90	V. low	100	C	CNT	*Sci. Rep.* **2013**, 3048, 1-8
46	62	100	62	-		R	PU-PEDOT/SWCNT/PU-PEDOT:PSS	*ACS Nano*, **2015**, 9, 6252-6261
47	2	30	83	-	-	C	AgNWs	*ACS Appl. Mater. Interfaces*, **2017**, 9, 26407-26416
48	3.3	30	92	Mod.	-	R	CNT- solution processing	*ACS Appl. Mater. Interfaces*, **2017**, 9, 26279-26285
49	2.9×10¹⁰	2.75	85	Low	30	R	**Present work (Au NW on PDMS)**	
	30-180	0.2-2.5	85			R		
	0.1-50	0.08-0.2	85			R		

3.2.2 Scope of the present investigation

Monitoring live movements of human body parts is becoming increasingly important in the context of biomedical and human machine technologies. The development of wearable strain sensors with high sensitivity and fast response is critical to addressing this need. In this work, a crackle based Au network is fabricated by semi-embedding in PDMS. As the device is stretched, the network breaks into millions of fragments, being held together by PDMS. The contact between these fragments varies sensitively with strain giving rise to an exceptionally high gauge factor and a fast response. This property allows the device to be used for monitoring various bodily movements while being mounted away from the most active location where strains are the highest. In present

work, the device has been successfully used for monitoring hand movements, eye blinking and chewing. Owing to its sensitivity, it can be used for pulse analysis (by studying pulse width, frequency, and amplitude) for diagnosing various ailments. Incorporating the device into smart watches can also be explored because of its high reproducibility and accuracy. The second part of the work deals with making break junctions. Break junctions are highly effective tools for studying electrical transport through molecules such as C_{60}, thiols, pyridyl, carboxylic acid, isothiocyanate and so on. The stronghold of the Au network in PDMS allows instant formation and closing of several break junctions. The property of field-induced surface migration at the nano-constrictions can be utilized for self-healing in e-skin applications.

3.2.3 Experimental Section

Crackle Template Formation: 80 μL of the mixture of diluter (chloroform) and the crackle precursor (colloidal dispersion of an acrylic resin available commercially as crackle nail polish (Ming Ni Cosmetics Co., Guangzhou, China) at concentration of 0.55 g/mL is spin coated at RPM 1000 for about 100 sec on to a silicon substrate of area 3 cm × 1.5 cm.

Electroless Deposition: A solution of 17 mg of chloroauric acid ($HAuCl_4$) in 2 mL of water is prepared and similarly, a solution of 1.9 mL of water and 1.1 mL of Hydrofluoric acid (HF) is prepared. Both the solutions are mixed to be used as Au electroless solution having a concentration of 10 mM. Similarly, a solution having 20 mM concentration, is prepared by using 34 mg of chloroauric acid ($HAuCl_4$). After the development of interconnected crackles, the Si substrate is dipped in gold solution for a period of 2-4

minutes to deposit the gold in the interconnected crackle pattern. Then the substrate is cleaned with chloroform to remove the sacrificial layer.

Transfer Process to PDMS: Commercially available PDMS (10:1 ratio of elastomer and curing agent)[32] is sonicated for 8 min at a power of 50 W and a frequency of 37 Hz. The mixture is degassed in a desiccator for 20 min. Then, the PDMS is coated on the gold deposited silicon substrate. Specifically, 5 mL of uncured PDMS is poured, and it is kept for 2-4 minutes, so that PDMS can settle down on the surface, and fill in between the gold networks properly. The substrate is then heated for 45 minutes at 80 °C and the PDMS layer is peeled to obtain the sensor material, *i.e.*, PDMS embedded with the gold wire network.

Sample preparation: The samples are cut into a rectangular size of 2 cm × 1.5 cm. Copper wires along with the silver epoxy are applied on to the PDMS layer to form electrodes and dried in a hot air oven at 90 °C for 45 minutes. Finally, a digital multimeter (MS8218, Mastech) with RS232 port is used to monitor continuous changes in the resistance of the sensory device.

Electrical measurements: The strain sensor device was mounted on a screw gauge to provide strain in a controlled way. The electrical contacts were formed outside the stretchable area in order to prevent it from lifting off. The electrical measurements were made using Keithley 2300 using I-V and I-t modes.

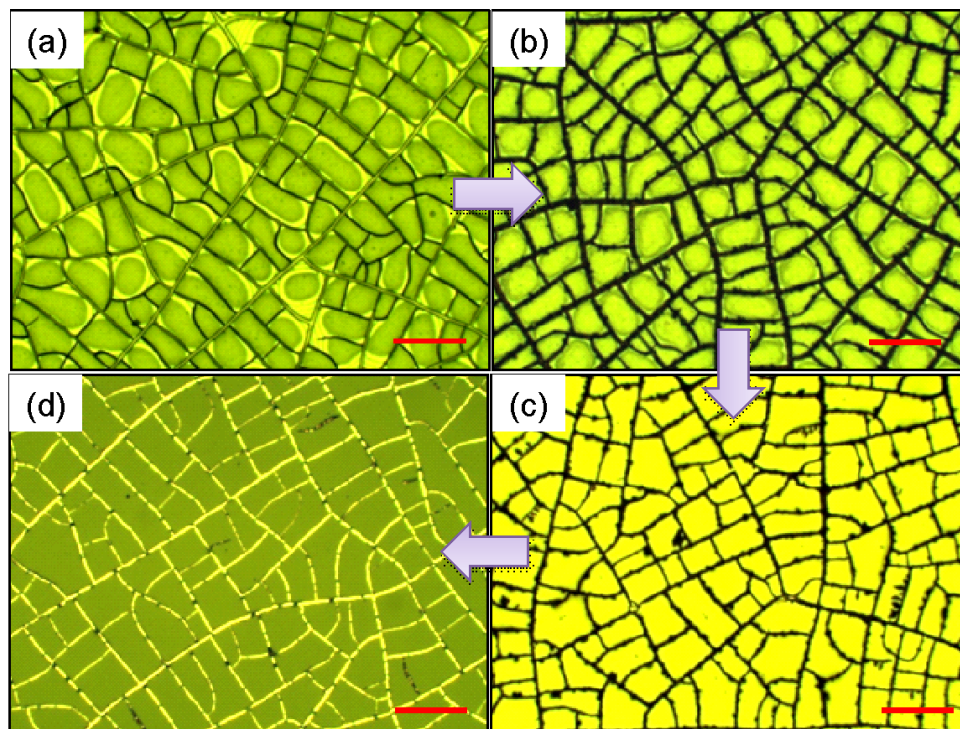## 3.2.4 Results and Discussion

Figure 3.2.1 Optical micrographs of (a) crackle template on Si substrate, (b) crackle template after electroless Au deposition, (c) Au wire network on Si substrate following lift-off and (d) transferred Au wire network on PDMS substrate. Scale bar, 50 μm.

The strain sensor fabrication combines template formation using crackle lithography,[33,34] metal deposition by a solution based electroless process, and a process to transfer the metal wire mesh onto a PDMS substrate. Briefly, a crackle dispersion consisting of acrylic resin nanoparticles in water was spin coated on a Si substrate to produce a network of fine crackles upon drying. This crackle template on Si substrate was then dipped in an Au electroless plating solution and following lift-off in chloroform, a continuous Au microwire mesh was formed on the substrate (see Figure 3.2.1 for the optical micrographs of each step). The reliability of the crackle lithography can be clearly seen, as moving along the process steps. The highly interconnected Au
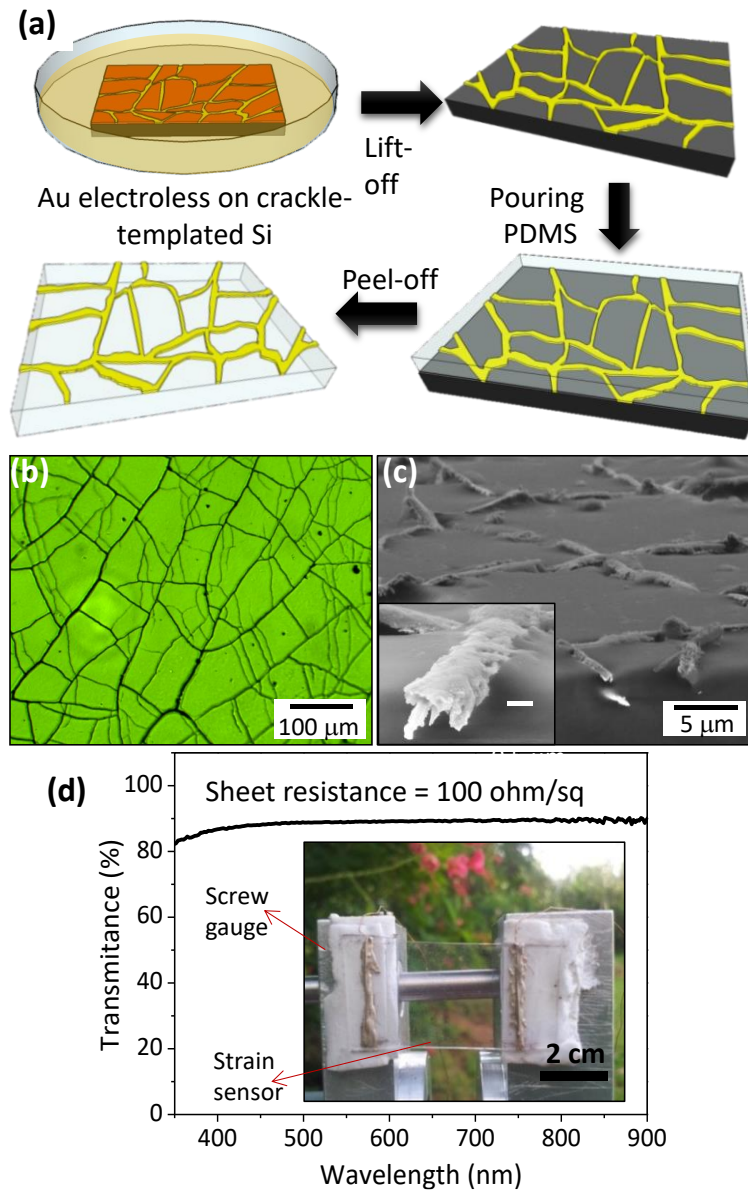
Figure 3.2.2 (a) Process flow of strain sensor fabrication involving crackle templating, lift-off, PDMS casting and peel off. (b) Transmission mode optical micrograph of Au micro wire network embedded in PDMS showing high interconnectivity. (c) Scanning electron micrograph of Au micro wire network embedded in PDMS. (d) Absorption spectrum in the visible range along with a photograph of the sensor mounted on a screw gauge (in the inset).

wire network on PDMS is achieved even after the transfer process. In electroless deposition, Si is etched away from the exposed regions to produce nanometric trenches as the Au growth begins.[35] Depending on the deposition conditions, the growth continues eventually projecting the Au wire thickness well above the substrate surface. Following the mesh formation, the desired volume (~2 mL) of pre-mixed PDMS was poured on the micro mesh/Si and cured. In the final step, the cured PDMS film carrying the Au wire mesh was gently peeled-off from the Si substrate. Figure 3.2.2a shows the schematic of the process for making a strain sensor device. Figure 3.2.2b clearly shows that the network was transferred onto PDMS without any breakage or discontinuity and that the transferring process is spotless. This is not surprising as the adhesion of Au wires on Si is rather poor; a drop of water can also dislodge the network from the substrate. In the SEM image in Figure 3.2.2c, the Au wires are seen to be partially embedded, which is expected as PDMS is known to conform closely to the surface topography which in this case is the exposed thickness of the wire above the Si substrate. A magnified view (see the inset of Figure 3.2.2c) shows that nearly half the wire thickness (~ 250 nm) is embedded in PDMS. The transmittance spectrum in Figure 3.2.2d is featureless with the overall transmittance being around ~85% (also evident from the photograph in the inset), and the measured sheet resistance is 100 $\Omega/\square$.

In order to examine the stretchability of the wire network, the device was attached to a screw gauge (least count, 10 μm) as shown in the inset of Figure 3.2.2d, with Ag epoxy contacts attached outside of the strain area. The device resistance was monitored while stretching it in increments of 50 μm. The strain was calculated as

$$\text{Strain} = \varepsilon = \Delta L/L \ \times 100\% \tag{1}$$

where ΔL is the change in length and L is the original length. As shown in Figure 3.2.3a, the resistance was observed to increase in steps with increasing strain, gradually from the initial 800 Ω at 0% strain to 4 kΩ at 1.7% strain, marked as region 1 (the low resistance regime where the I-V is linear) in Figure 3.2.2b. Beyond 1.7%, the device resistance jumped to 2 GΩ and eventually to ~ 6 GΩ under 2.6% strain, which is marked as region 2 (high resistance regime where the I-V is non-linear). Importantly, when the strain was gradually withdrawn, the resistance of the device decreased and reached its original value (see Figures 3.2.3a and b). To see the isotropicity of the strain sensor, strain was applied from two directions, namely longitudinal (along the length) and transverse (along the width). In the case of longitudinal strain, the strain direction and applied electric fields are parallel whereas in transverse strain both are perpendicular. Figure 3.2.4 clearly demonstrates the versatility of the strain sensor while responding to longitudinal and transverse strain and hence may be qualified as an 'isotropic' strain sensor.

The gauge factor was calculated using the following equation,

$$\text{Gauge factor} = (\Delta R/R)/\varepsilon \tag{2}$$

where ΔR is change in resistance, R is initial resistance. For R = 850 Ω, ΔR = 5.2× 10^9 Ω, and ε = 0.0275, the estimated gauge factor for this device is 2.2 × 10^8, which is among the best values reported in the literature (see Table 3.2.1).
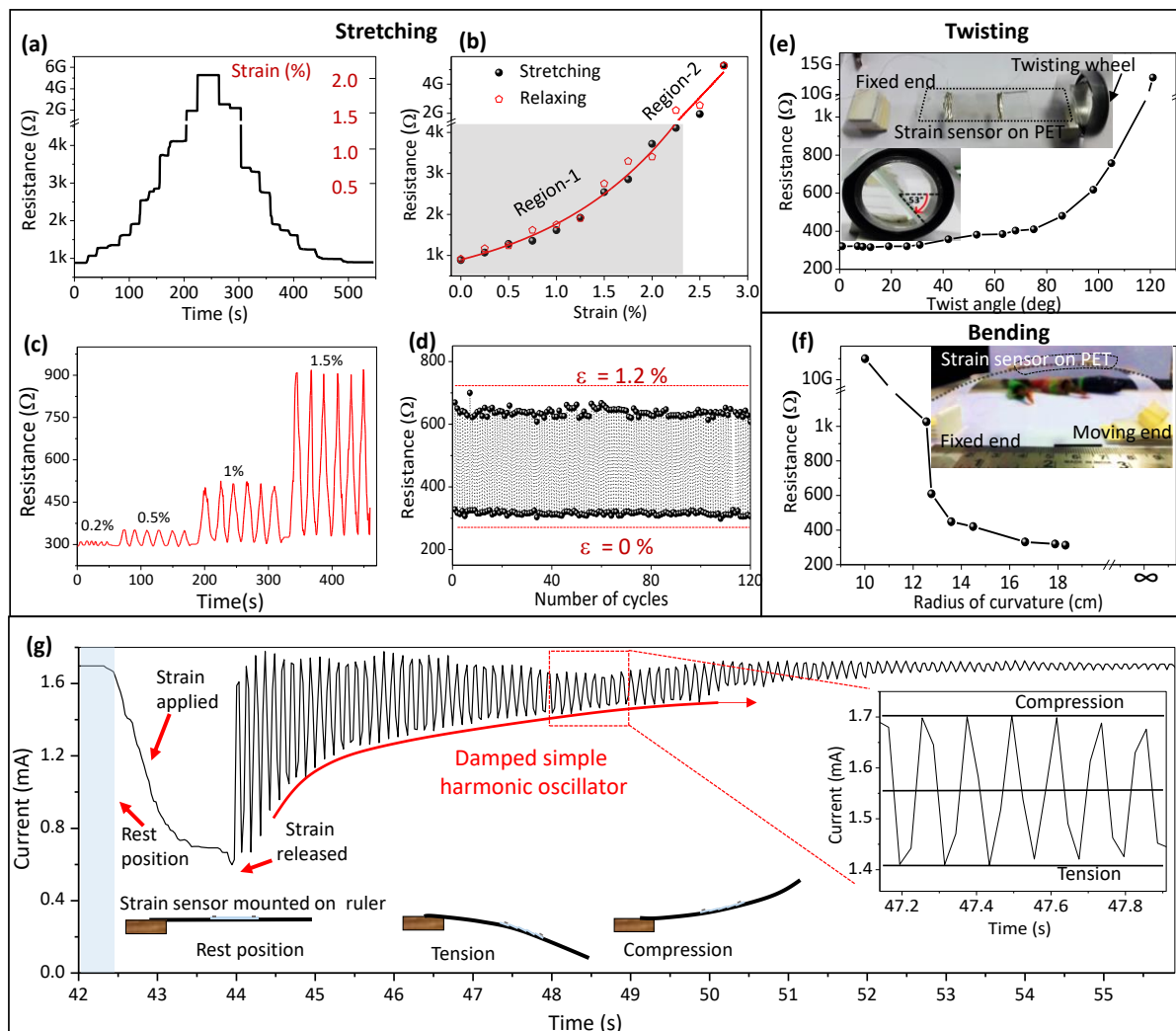
Figure 3.2.3 (a) Change in resistance with step by step increase in strain, (b) Resistance versus strain due to tension during stretching and relaxing the sample. Region 1 corresponds to the low resistance regime and region 2 to the high resistance regime. (c) Resistance versus time during cycling between 0 and a set value of strain to observe repeatability. The strain levels for each set of 6 cycles are indicated on the graph. (d) Resistance during 120 cycles of straining to 1.2% to check the reliability of the sensor. (e) Resistance versus twist angle for the case where the strain sensor is twisted along the axis between two electrodes. The front view shows 0° twist (flat), and the side view shows 53° twist. (f) Resistance versus the radius of curvature while bending the strain sensor with the setup shown in the inset. (g) Evolution of the current when the strain

sensor is mounted on a ruler and brought into simple harmonic oscillations as shown in the schematic. The inset depicts enlarged view of the oscillations.

The fabricated sensor was taken through several cycles of strain, while monitoring the resistance value. Six such cycles were performed at a given maximum value which was increased gradually from 0.2% to 1.5% for a total of 24 cycles (see Figure 3.2.3c). Further, the same device was taken through another 120 cycles at maximum strain of 1.2% (see Figure 3.2.3d). The device performance was consistent with variations within 5%.
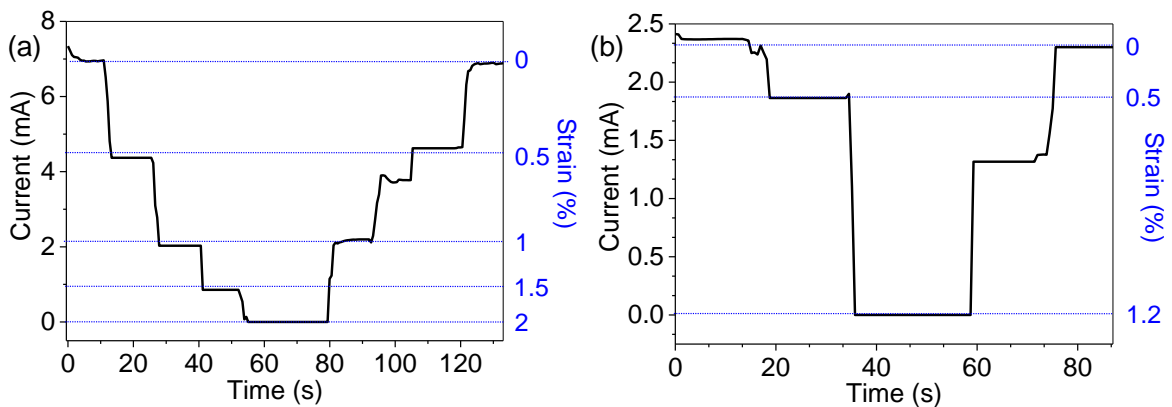
Figure 3.2.4 Change in the current of Au wire network/PDMS strain sensor with respect to applied strain along (a) longitudinal and (b) transverse directions, respectively.

The strain sensor was subjected to twisting and bending strains as well. The sensor was attached to a PET sheet that was twisted using a simple setup as shown in Figure 3.2.3e. The resistance of the strain sensor increased with increasing twist angle, exhibiting both low resistance (linear I-V) and high resistance regime (non-linear I-V). For bending measurement, the PET sheet mounted with a strain sensor was fixed on its left edge while its right edge was moved to different positions to achieve a range of

curvatures (see Figure 3.2.3f). The resistance increased with higher curvature showing a similar trend as that observed in stretching and twisting. Although stretching, bending and twisting demonstrate similar changes in resistance, twisting led to a gradual increase in resistance while bending showed a highly exponential increase in resistance. These aspects will be revisited later.

In order to determine the response time, the strain sensor was mounted atop a cantilever, a stainless-steel meter ruler with one end fixed on the edge of a table (see Figure 3.2.3g inset). When the ruler was pushed downward manually, it equaled to a strain 0.2% on the sensor. As a result, the current dropped to nearly one-third of its original value. When the ruler was released and oscillated freely, the signal took the form of the damped harmonic oscillations. When the ruler got bent in the downward direction, the sensor experienced mechanical stretching (i.e. tension) increasing resistance and reducing the current. Similarly, when the ruler got bent in the upward direction, the sensor experienced mechanical compression reducing resistance and increasing the current. Thus, each oscillation of the ruler consisted of a tension and compression cycle of the strain sensor. The same oscillations were reflected in the magnified view clearly depicting the compression and tension of the strain sensor. The current followed the oscillations until the strain was below the measurable limit of 0.04%. A response time of 30 ms was estimated using tension and compression cycles, which is one of the best values reported to date (See Table 3.2.1).
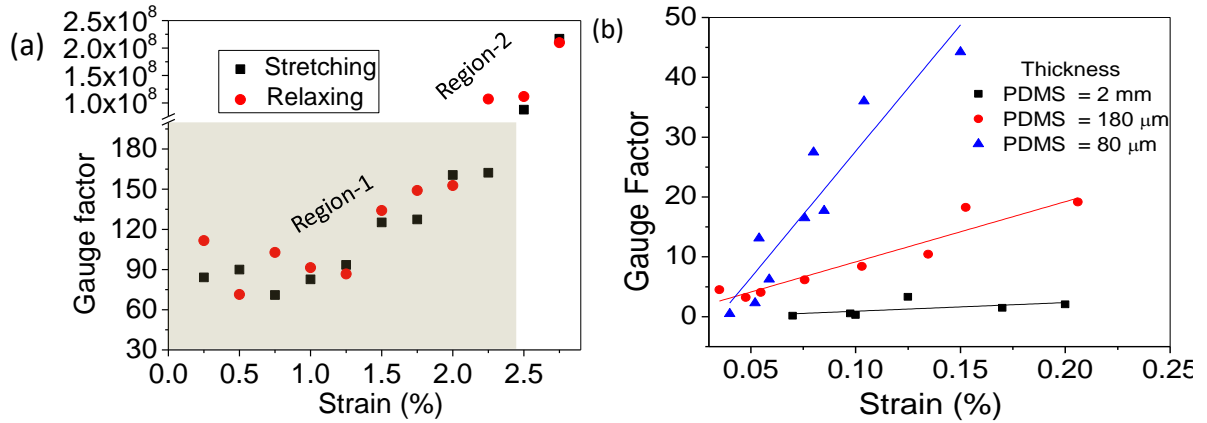
Figure 3.2.5 (a) A plot between gauge factor and applied strain of Au wire network/PDMS strain sensor. (b) A plot between gauge factor and applied strain for different thicknesses of PDMS.
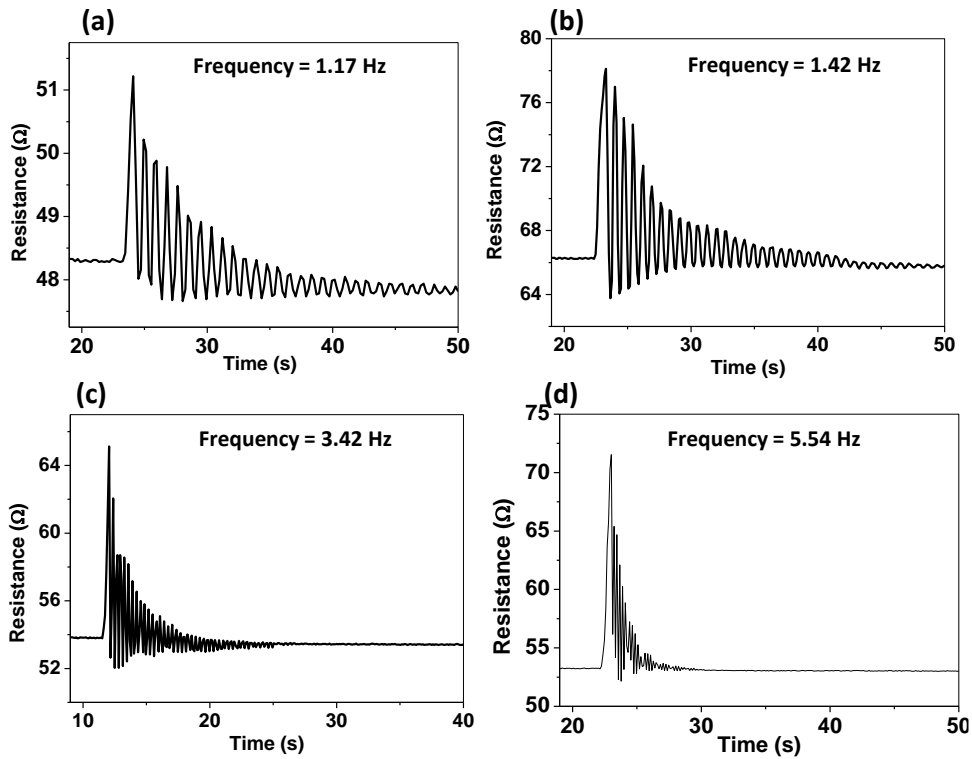

Figure 3.2.6 Resistance loading-unloading cycles of strain sensor mounted on an oscillator by applying various frequencies.
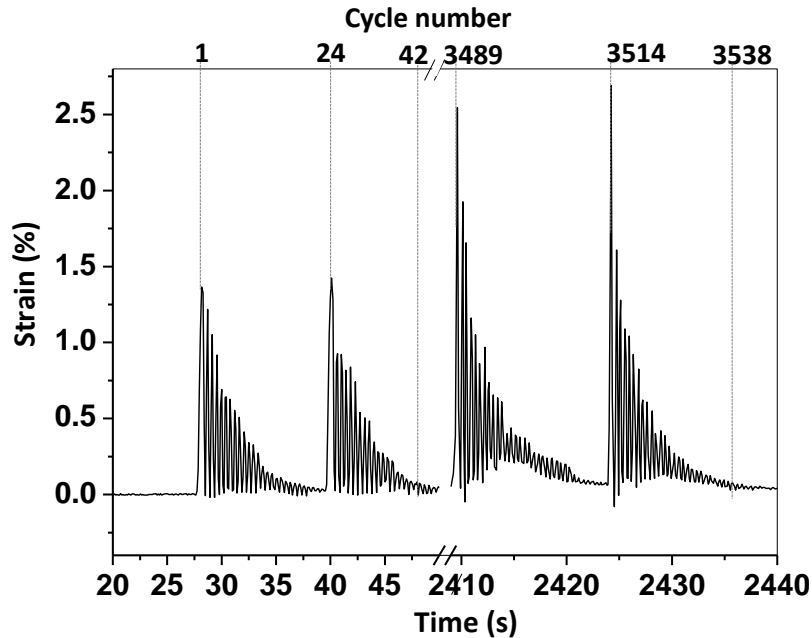
Figure 3.2.7 Stability test: Strain loading and unloading cycles of strain sensor by bringing repeated oscillation in the strain sensor.

The strain sensor detected 0.04% strain with 30 ms response time with a gauge factor of 0.1. The low gauge factor is attributed to the high thickness (~2 mm) of PDMS. The gauge factor varies with the applied strain, from 100 to 2.2×10^8. Figure 3.2.5a shows two regions of strain where in region-1, gauge factor is 60 – 200 and in region-2, gauge factor is 10^8. As the PDMS thickness decreases, the gauge factor increases. Figure 3.2.5b shows gauge factors for different thicknesses of PDMS. For a strain value of 0.1%, gauge factors for strain sensors having PDMS thicknesses of 2000, 180 and 80 μm are 0.3, 8.4 and 36 respectively. The slope between gauge factor and applied strain are 14, 100 and 422 for PDMS respective thicknesses. The strain transferred to the Au wire mesh increases when the PDMS thickness reduces. The strain sensor with a PDMS thickness of 80 μm, detects low strains of 0.04%, with a gauge factor of 46. Smaller thicknesses of PDMS

allow effective detection of lower strains with high gauge factors. Smaller thicknesses of PDMS effectively detect lower strains with high gauge factors. One such strain sensor was subjected to damped oscillations from a cantilever - a steel meter ruler, which was fixed to a table-top at one end while projecting the rest of the length freely for oscillations. The frequency of this cantilever was varied by simply changing the projected length. Thus, the applied frequency varied from 1.17 to 5.54 Hz. In each case, the resistance remained similar, before and once the oscillations subsided. Although the frequency was varied, similar bending angles (~ 45°) were used in each case. The sensor had excellent resistance's stability, before and after the decay of oscillations (see Figure 3.2.6). The device was also tested for its stability by oscillating it at a frequency of 2.44 Hz. As is clear from Figure 3.2.7, the sensor is highly stable. At a particular strain, the measured initial amplitude is the same. The bottom x axis shows time and the upper x axis shows the number of cycles. For observing the performance, the first two and the last two sets of damped oscillations are shown. The performance was found to be consistent even beyond 3500 cycles.

To facilitate the understanding of the strain sensing mechanism, *in situ* microscopy and electrical characterization were carried out. In the relaxed state (zero strain) of the device, the I-V characteristics were linear as shown in Figure 3.2.8a, indicating that conduction through the percolative wire network is Ohmic and diffusive. In this case, all the wires must be well connected as shown in Figure 3.2.2b. However, with 2.5% applied strain, the I-V characteristics became non-linear, with current decreasing more than three orders of magnitude as shown in Figure 3.2.8a. SEM images (see inset
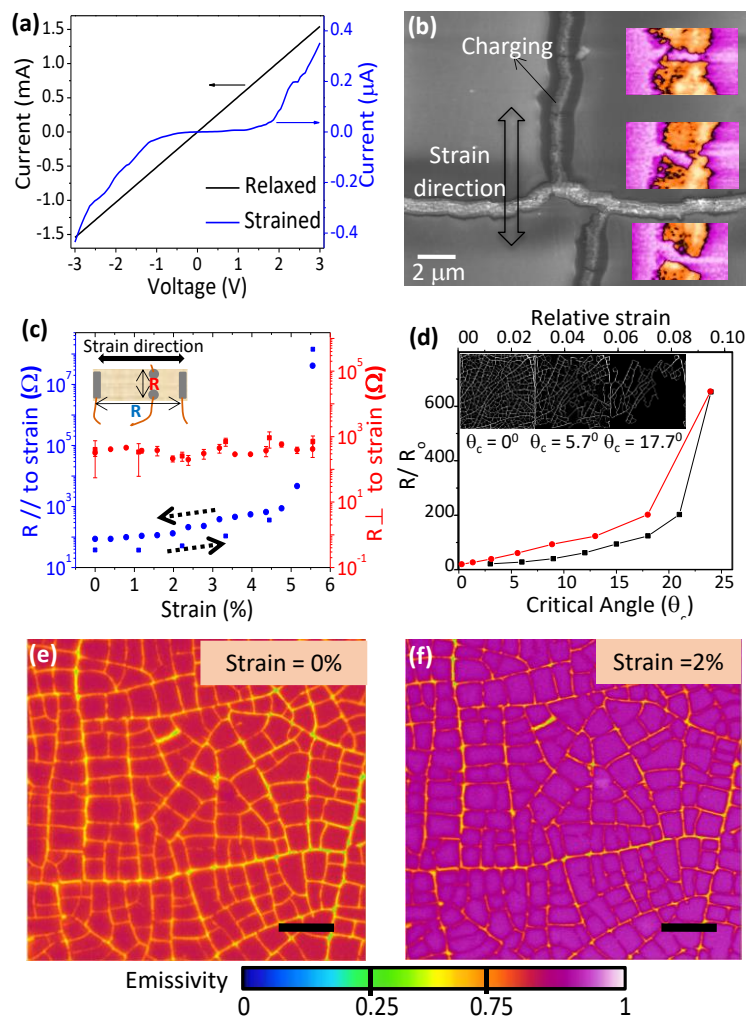
Figure 3.2.8 (a) Current-voltage plot for low resistance regime (black) and high resistance regime (blue), (b) SEM image of the Au micro wire network after applying 2.5% strain with insets showing the magnified view of a single Au micro wire with false colours, (c) Resistance variation perpendicular to the strain direction (red) compared with variation parallel to the strain direction (blue), while increasing the strain (circles) and while releasing the strain (squares). The inset shows the parallel and perpendicular electrodes with the same colour scheme, the black arrow shows the strain direction. Fresh contacts were made for every strain reading. (d) Relative change in resistance versus relative strain (upper x- axis) and relative change in resistance versus critical angle (lower x-axis). Apparent emissivity maps of the Au micro wire network surface in the (e) unstrained and (f) stretched (2%) conditions while 0.7 V DC was applied.

of Figure 3.2.8b) during *in situ* application of 2.5% strain clearly demonstrate the opening of nano-gaps in the wires along the strain. A magnified view of nano-gaps in Figure 3.2.8b reveals that the gaps are around a few nanometers to ~100 nm wide. Surprisingly, the wires in the direction perpendicular to the strain were intact, and no breakage was observed (see Figure 3.2.8b). Similar break junctions appear upon bending and twisting, the only difference being in the areas of breakage. On bending, the conducting path between electrodes suddenly breaks perpendicular to the strain direction, disconnecting the two ends, making the strain sensor reach the high resistance regime suddenly with an increase in curvature (see Figure 3.2.3f). On twisting, the network region away from the twisting axis stretches gradually with increased twist angle, and the network region near to the twisting axis changes negligibly with the increase in twisting angle. This makes the conducting path gradually increase its resistance with twist angle (see Figure 3.2.3e). Lastly, stretching leads to uniform breaking of the network throughout the strain sensor which makes the rate of resistance increase, intermediate to those of twisting and bending (see Figure 3.2.3b).

The non-linear I-V characteristics observed in the high resistance regime are attributable to tunneling or filamentary conduction across the nano-gaps in the network under high strain, which after release of the strain smoothly converted back to linear I-V characteristics (see Figure 3.2.8a). The SEM of a break junction before applying strain and after releasing strain (see Figure 3.2.9c) revealed that the gaps although uneven, close conformally leaving no gap, thanks to the stronghold of the
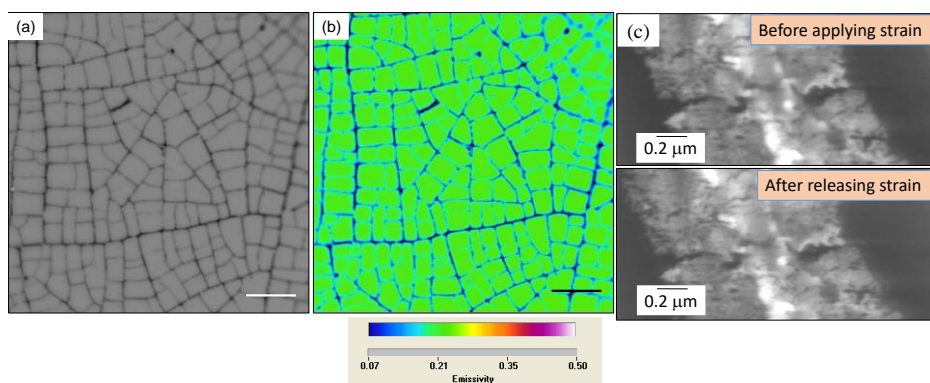
Figure 3.2.9 (a) The infrared microscope image of the Au wire network embedded in PDMS and corresponding (b) Emissivity map without applying bias. (c) SEM image of break junction in Au network before applying and after applying strain.

PDMS substrate on embedded wires (see Figure 3.2.2c). Its significance became apparent when compared with devices made using vacuum deposition of the metal instead of electroless deposition. In order to examine reproducibility and reliability of the fabrication process, various devices were fabricated using vacuum deposition and solution processed deposition of the metal, while keeping the rest of the process unchanged. In the case of vacuum deposition, the crackle templating, metal deposition and lift-off were carried out directly on the cured PDMS surface. The gauge factors of all devices fabricated in the study is shown in the form of a histogram (see Figure 3.2.10a). From the histogram, it is clear that there is more variation in the gauge factors of sensors obtained from vacuum deposition (red bars in Figure 3.2.10a), whereas solution processed devices showed consistent and high gauge factors (blue bars in Figure 3.2.10a). Out of the 8 devices made using vacuum deposition, only two showed gauge factors in the range of 10^9 while others were down to 10^7. When operated
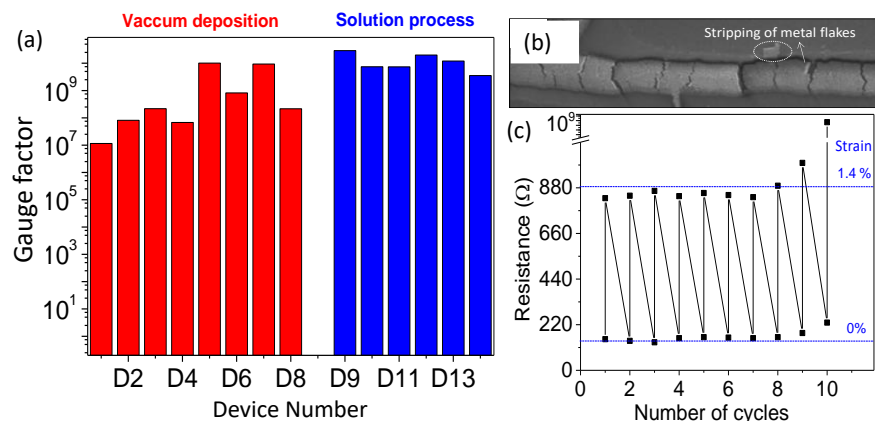
Figure 3.2.10 (a) Gauge factors in the form of histogram of various devices fabricated using electroless deposition (D1-D6) and by vacuum deposition of the metal over the crackle template. (b) SEM image of vacuum deposited Au wire after 30 stretching cycles. The marked region shows a metal flake stripped-off from a nanogap. (c) Change in the resistance of vacuum deposited Au wire network during stretching cycles between 0 and 1.4% strain.

beyond 10 cycles of 1.4% strain (see Figure 3.2.10c), the sensor became defective as metal from nano-gap regions was found to detach (see SEM image of stripping metal flakes in Figure 3.2.10b). On the contrary, those prepared with electroless deposition (D9 – D13) had the wire network well embedded in PDMS matrix and showed consistent gauge factors of $(1.32 \pm 0.9) \times 10^{10}$ and worked reproducibly over 2% to 4.6% strain. The inconsistency in vacuum deposited strain sensors may be attributed to permanent breakage of the interlock junctions, as depicted in the SEM image of Figure S5b. Both detachment and stripping of metal flakes from the wire network is clearly seen. The vacuum deposited Au wires tend to peel off after a few stretching cycles which is attributed to bad adhesion between Au wires and the PDMS surface. In solution processed Au wire network/PDMS, Au wires are embedded in the PDMS matrix. The

polycrystalline nature of the Au microwire network allows it to respond to small strain by creating break junctions. The embedding of Au micro wire network in PDMS matrix not only furnishes a tight hold but also provides a back-bone support during stretching and compression, resulting in complete recovery of the Au microwire network. Thus, solution processed crackle lithography is a promising method to fabricate consistent and reliable strain sensors (see Figure 3.2.11). The applied strain range can be increased with the increase in the active area of the device.
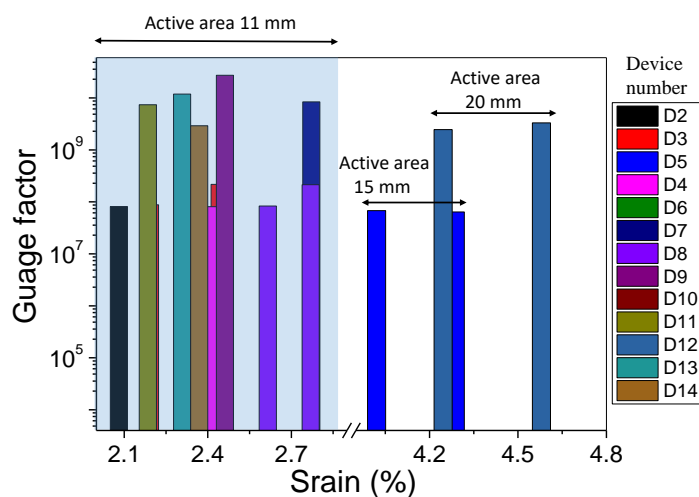

Figure 3.2.11 A plot between gauge factor and input strain for 13 strain sensors fabricated in this study. In the region-2, gauge factor is plotted with respect to applied strain. The applied strain range can be increased with the increase in the active area of the device.

The possibility of crosstalk in the direction perpendicular to the strain was assessed by recording IV data for both directions, parallel and perpendicular to strain at each strain value (Figure 3.2.8c). The inset shows the electrode configuration. The resistance along the strain direction increased monotonically as expected (see Figure 3.2.3b), while that measured perpendicular to the strain was independent of the strain. The trends

were similar for both increasing (squares) and decreasing (circles) strain sweeps. This behavior clearly indicates that the conduction paths break only in the direction of the strain, permitting the current to pass in the perpendicular direction. If the strain sensor is made to have two pairs of electrodes perpendicular to each other, the relative changes in resistance along the two electrodes can be used to identify the direction of strain as well. These aspects gave us clues to look into the possible mechanism. In a theoretical approach, metal mesh was modeled as a network and its resistance was calculated based on Kirchhoff's laws.[36] On applying strain, the network stretched, and wire segments broke successively with increasing strain based on their angle with respect to strain direction. The study showed two regimes for resistance increase; for lower values of strain, resistance increased linearly with a small slope; while at higher stain values, due to formations of bottlenecks in the percolative paths, resistance increased non-linearly with a larger slope (see Figure 3.2.8d). The theoretical model predicted two regimes, explaining the experimental observations (see Figure 3.2.3b).

In order to gain more insights into the strain sensing mechanism, the strain sensing was performed *in situ* under infrared microscope imaging. The Infrascope thermal microscope maps the mid wavelength IR radiation emitted by the sample. Here, a DC bias was applied to the sample and the spatial distribution of apparent emissivity was recorded. A 0.7 V DC was applied to the strain sensor while collecting the radiance data (see Figures 3.2.9a and b). Comparing the apparent emissivity map in Figure 3.2.8e with the transmission optical image in Figure 3.2.9a, the current paths in the network are easily distinguishable with complete wire connectivity. Under strain measurement

conditions (0.7 V, strain of 2% along the direction shown in Figure 3.2.8f), the change in apparent emissivity of the PDMS surface is uniform; however, the change in the apparent wire surface emissivity is non-uniform. Specifically, the thinner wires in the network emit much more IR energy compared to thicker wires due to their higher Joule heating, and, thus, higher temperatures.

Transparency of the strain sensor is an additional desirable attribute though it need not contribute functionally. In the context of therapeutics, it may add a great value, particularly in situations where the sensor is to be concealed while being attached to the outer parts of the body of an individual such as the face or hand with the goal of not affecting the aesthetic appearance. Further, transparency of the sensor plays an important role if the device should enable a physician to see through it while monitoring the underlying skin/body part for possible swelling, injuries or for rashes. Here, the utility of transparent strain sensors was examined in three contexts.

In the first context, the sensor was placed on opisthenar of a volunteer as shown in the photographs of Figure 3.2.12a. The current passing through the device was monitored as a function of hand gestures. From the relaxed position (gesture 1), the current decreased to nearly 50% in the partially stretched position (gesture 2), and to its minimal value (~2 nA) in completely stretched position (gesture 3), the latter presenting a near complete breakage of the wire network. The device performance was found reproducible over the 8 cycles tested for the strain range 0%-3% (see Figure 3.2.12a).
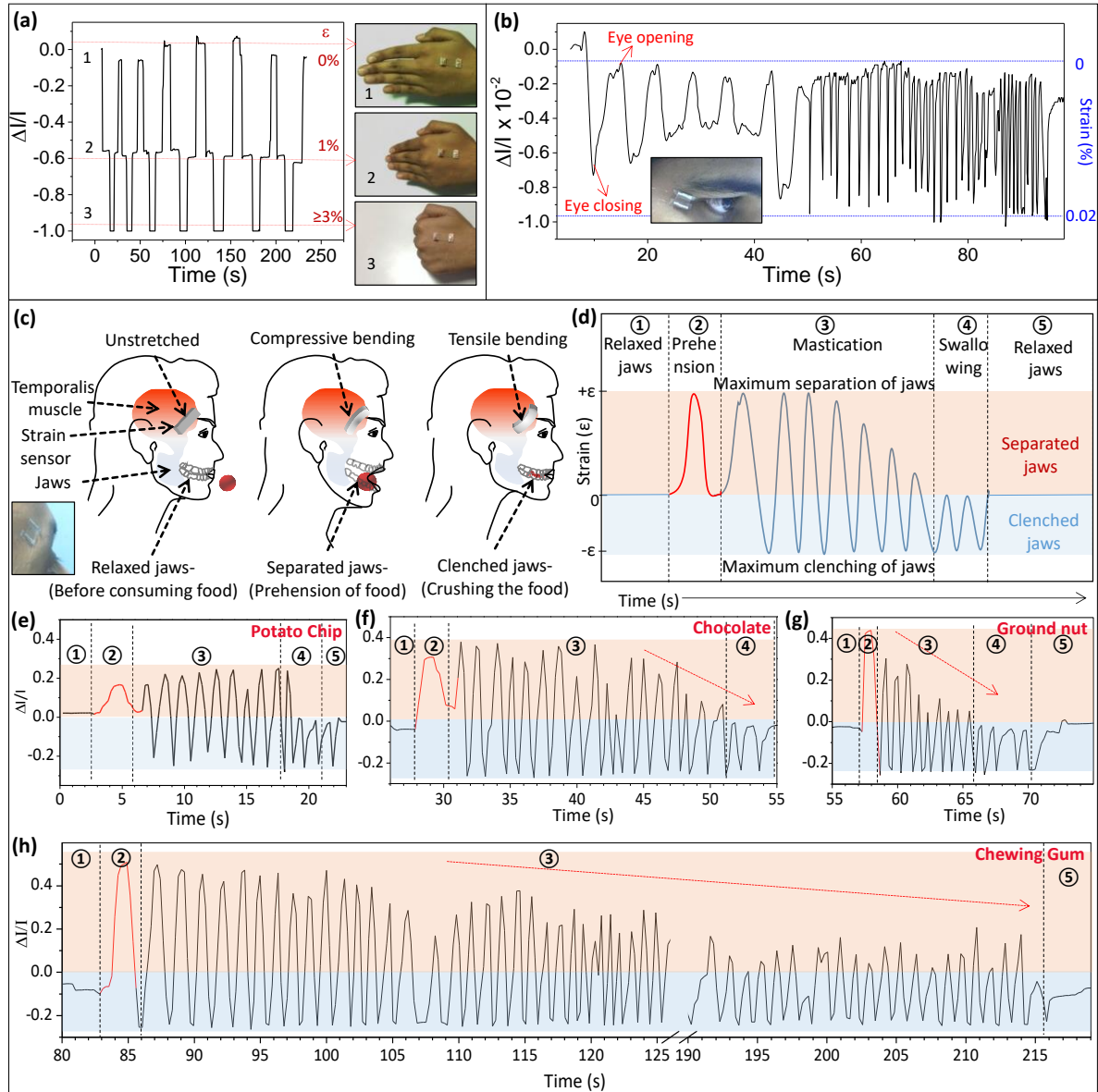
Figure 3.2.12 Relative change in current of Au mesh/PDMS, (a) while volunteer performs three gestures of hand with corresponding photographs of the sensor attached to the hand and, (b) while volunteer blinks his eye with different frequencies with the inset showing a photograph of the sensor struck to lateral canthus of eye. (c) Schematic showing the three states of jaws: relaxed, separated and clenched, and corresponding states of the strain sensor (attached in the region of temporalis muscle) while eating: relaxed, compression and tension. Inset shows the strain sensor mounted on the forehead of a volunteer near the location of temporalis muscle. (d) Representative plot

of strain with respect to time while eating having five stages: 1. Relaxed jaws, 2. Prehension, 3. Mastication, 4. Swallowing, 5. Relaxed muscle. Relative change in current while eating a (e) potato chip, (f) chocolate, (g) ground nut and (h) chewing gum. The stages are marked by their respective circled number. The red portions of the line indicate prehension of the food. On each graph, the light red zones indicate separated jaws and the light blue zones indicate clenched jaws. In each context, the strain is estimated using calibration plots (see Figure S9, Supporting Information).

In the second scenario, the device was adhered over a volunteer's lateral canthus of the eye to monitor the blinking of the eye (Figure 3.2.12b). Each blinking cycle involves a change in the current which was nearly two orders less compared to that of hand gestures and the corresponding strain developed was just 0.02%. The response of the device was remarkable with slow and fast blinking corresponding to frequencies of 0.15, 0.4 and 0.9 Hz, as depicted in Figure 3.2.12b. As illustrated, the strain sensor was able to detect such small strains with fast response.

Similarly, the sensor was placed on a volunteer's right temple in order to monitor the differential strain developed in the temporalis muscle while eating different kinds of foods (see inset of Figure 3.2.12c). Prehension of a food particle involves separation of the jaws which contracts the temporalis muscle, leading to compressive bending of the sensor as reflected by rise in current (see red portions of the curves in Figure 3.2.12c). As the jaws approach during mastication, the muscle pops up passing through its relaxed state, and finally, clenching of the jaws. This leads to tensile bending of the sensor leading to a decrement in the current. Thus, the mastication process in each case is marked by a pointed rise and fall cycles of the current. Following mastication, the

swallowing state is marked by current cycles below the rest value. During mastication of the soft food articles such as chocolate, the minimum current limit is reached immediately as the substance dissolves, allowing clenching of the mouth. The minimum current is reached immediately for chewing gum as well, the only change being in the value of the limit. During mastication of such an elastic food, the jaws cannot be clenched fully as there is always a certain amount of food between the jaws. The mastication of hard food articles such as potato chips and ground nuts, involve breaking down into smaller pieces in first few cycles requiring the jaws to separate widely thus giving rise to varying current maxima throughout the process. This is why the current minima is reached gradually as marked by green arrows. However, the clenched state of the jaws is same throughout the process which is clearly observed by the current always falling to the fixed minimum limit i.e. $\Delta I/I \sim 0.26$. For potato chips, the jaws may not always become clenched given their crispy nature, giving slight inconsistency in its current minima. In the case of chocolate mastication, the oscillation amplitude is higher due to a relatively larger size of the food article. Bigger food articles involve breaking down without clenching the jaws for accommodation in the mouth. During mastication of ground nuts, the current maxima decreases rapidly due to its powdery nature. The amplitude of the mastication cycles for chewing gum is higher for more cycles as the jaws have to be separated wider apart to allow the gum to change its shape. Also owing to negligible change in its volume and no involvement of particles breaking down, the amplitude of cycles decayed very slowly, and the mastication was forcefully brought to an end. Breaking down of food articles effectively demonstrates a

gradual decay from mastication to swallowing. Abrupt changes indicate the swallowing of bigger particles before making them into a fine paste. Sensing of such minute details can be utilized to monitor proper chewing of food by a dietitian. Hence, the strain sensor fabrication in this method is able to sense eating of various food articles with well differentiated signals. Such a device can be easily integrated on any part of the body, and highly local body movements can be monitored. This may be used in the automatic monitoring of hand gestures or body movements as a patient recovers from an injury.
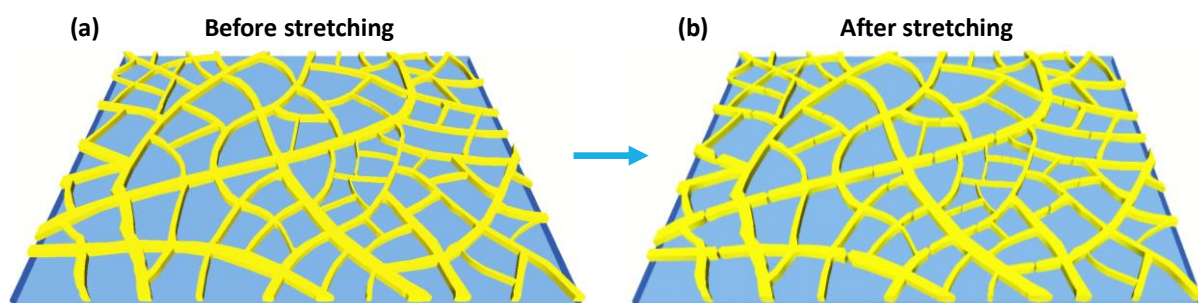
Figure 3.2.13 Schematic of strain sensor before and after stretching showing formation of numerous break junctions.

The strain sensor device, along with showing resistance changes on applying strain, also forms numerous break junctions when stretched (see Figures 3.2.13a and b). When the Au network/PDMS is stretched, the Au wires start to thin, forming constrictions, eventually leading to formation of nanogaps. As the Au wires are randomly distributed in a uniform PDMS matrix, even a strain as small as 0.1% leads to the formation of several nanometric breaks. This facilitates easy fabrication of mechanically controlled break junctions. When an electric field is applied to nanometric gap, it is possible to ionize the surface atoms of the protruding surface by field evaporation.[37] Lesser the
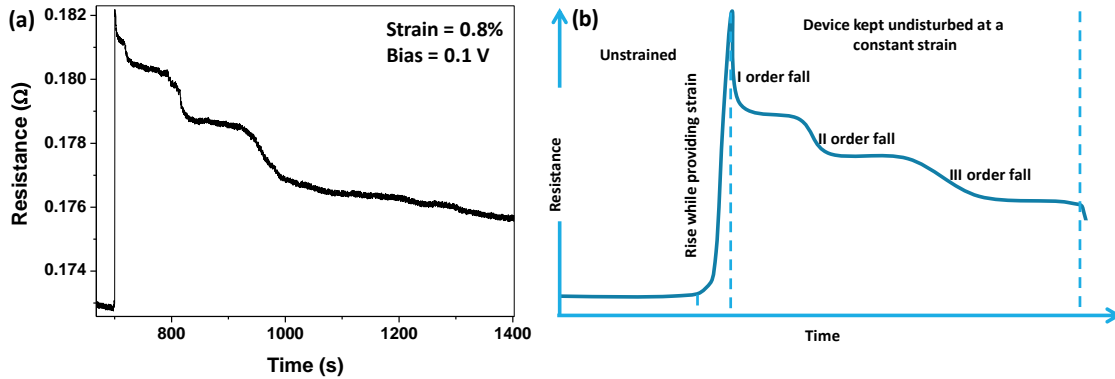
Figure 3.2.14 Electric transport through strain sensor at constant strain. (a) Change in resistance across the strain sensor while providing continuous bias of 0.1 V at a constant strain of 0.8%. (b) Schematic of resistance versus time plot of strain sensor at constant strain.

gap and more pointed the protrusion, easier is the thermal activation of the surface. This technique is usually required for preparing samples for field ion imaging, but it can be utilized to connect close enough surfaces especially when the surfaces are rough. Because of random stretching of the Au network, the break junctions that are formed have a rough surface. Therefore, the sensor was stretched to different strains in the steps of 0.2% and kept at that strain for ~20 minutes, while a constant bias of 0.1 V is applied, to observe any signature of field evaporation. For each of these strains, a sudden increase in resistance was observed while the strain is provided, followed by a sharp dip and then decrease in resistance in step like fashion as shown in Figures 3.2.14a and b. It is known from the literature that when gold quantum point contacts are stretched, linear strands of gold atoms forming the bridge get broken one by one leading to a step like decrease in conductance. However, for this strain sensor, there is a sudden jump in resistance because in a few seconds, numerous Au strands are getting broken. When left undisturbed in this stretched state, the breaks join together through the formation

of these strands, because of which the reduction in resistance has a step-like increase. When these strands keep joining, for a long enough time, gaps as large as tens of nanometers also may get closed leading to restructuration. This was observed by performing *in-situ* scanning electron microscopy while providing bias of 0.5 V. As shown by dotted red circles in Figures 3.2.15a-c, the gaps at one of the nodes of the Au wire network became smaller going through restructuring as the bias was provided for 10 minutes (see Figure 3.2.15b) and for another 10 minutes (see Figure 3.2.15c). Also, as the time progresses, the steps in I-t characteristics become more and more gentler, *i.e.* the rate of decrease in resistance becomes lesser (see Figure 3.2.16a). This behavior was observed for other strains as well.
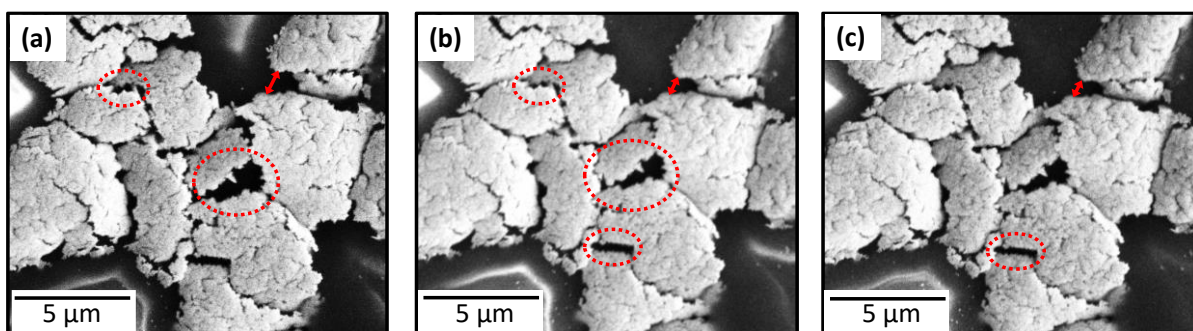

Figure 3.2.15 SEM images of Au wire network nodes (a) before healing, (b) after 10 minutes of providing 0.5 V bias and (c) after 20 minutes of providing 0.5 V.

As field induced surface migration is causing the gaps to close, different biases led to different extents of healing. The mean resistance while applying a bias of 0.2 V, was always higher as this is the lowest applied bias and therefore could heal the least number of junctions, irrespective of how much strain was provided. The higher biases (0.5 and 0.7 V) led to lower mean resistance for respective strains. However, when the

bias was higher than 0.7 V, the mean resistance rose again. The possible explanation for this behavior is that at such a high bias, the effects of Joule heating are more pronounced, which once the gaps are closed, only increase the temperature of the overall network thus increasing their mean resistance.[38] Thus, a bias of 0.7 V is optimum for bridging the break junctions. Importantly, all the measurements were done on the same device and were repeated thrice in order to have a statistical average. One device was taken through ~20 straining-healing cycles, which emphasizes repeatability of controlled straining and healing in the strain sensor device. Because the device is made up of PDMS, a skin friendly polymer, this property finds a natural use in the self-healing of e-skins, where any bruise may be healed by applying a bias.
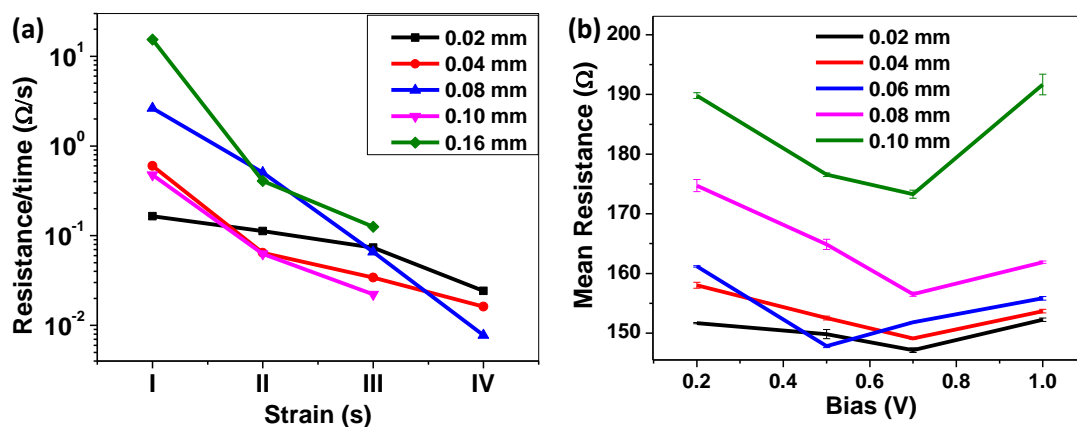

Figure 3.2.16 (a) The plot of rate of resistance change while keeping the strain constant for different biases and for different strain values. (b) Mean resistance while the strain was kept constant with increasing biases for different strain values.

3.2.5 Conclusions

In this work, a crackle templating method was employed to fabricate a solution processed Au microwire network embedded in an elastomeric matrix. PDMS not only

serves as a flexible substrate but also provides a robust matrix for the wire network via a transfer process. The strain sensor was investigated over a wide strain range from 0.02% to 4.5%, in both tension and compression cycles, and is reliable over many stretching cycles. The sensing mechanism was examined in detail using infrared microscopy and scanning electron microscopy (SEM), revealing formation of break junctions during the strain and complete recovery of the Au microwire network after release. The strain sensor with transmittance of over 90% is one of a kind having high sensitivity at both low and high strains along with ultra-fast response. These values are commendable compared to those reported for transparent sensors found in the literature. The strain sensor's application was evaluated with a test subject to monitor and capture sensitive human movements such as hand gestures, eye blinking and chewing. The strain sensing works in a range starting perfectly suited to these applications with a gauge factor exceeding 10^8. These strain sensors are safe to be placed on the skin with a minimum visibility for aesthetics and with sensing capabilities away from the sensitive organs.

3.2.6 References

1.   Lee, S.; Reuveny, A.; Reeder, J.; Lee, S.; Jin, H.; Liu, Q. H.; Yokota, T.; Sekitani, T.; Isoyama, T.; Abe, Y.; Suo, Z. G.; Someya, T., A Transparent Bending-Insensitive Pressure Sensor. *Nat. Nanotechnol.* **2016,** *11*, 472-478.

2.   Shi, G.; Zhao, Z. H.; Pai, J. H.; Lee, I.; Zhang, L. Q.; Stevenson, C.; Ishara, K.; Zhang, R. J.; Zhu, H. W.; Ma, J., Highly Sensitive, Wearable, Durable Strain Sensors and

Stretchable Conductors Using Graphene/Silicon Rubber Composites. *Adv. Funct. Mater.* **2016,** *26*, 7614-7625.

3.   Moon, H.; Lee, H.; Kwon, J.; Suh, Y. D.; Kim, D. K.; Ha, I.; Yeo, J.; Hong, S.; Ko, S. H., Ag/Au/Polypyrrole Core-shell Nanowire Network for Transparent, Stretchable and Flexible Supercapacitor in Wearable Energy Devices. *Sci. Rep.* **2017,** *7*, 41981.

4.   Wang, Y.; Wang, L.; Yang, T. T.; Li, X.; Zang, X. B.; Zhu, M.; Wang, K. L.; Wu, D. H.; Zhu, H. W., Wearable and Highly Sensitive Graphene Strain Sensors for Human Motion Monitoring. *Adv. Funct. Mater.* **2014,** *24*, 4666-4670.

5.   Lin, Z. M.; Yang, J.; Li, X. S.; Wu, Y. F.; Wei, W.; Liu, J.; Chen, J.; Yang, J., Large-Scale and Washable Smart Textiles Based on Triboelectric Nanogenerator Arrays for Self-Powered Sleeping Monitoring. *Adv. Funct. Mater.* **2018,** *28*, 1704112.

6.   Stoppa, M.; Chiolerio, A., Wearable Electronics and Smart Textiles: A Critical Review. *Sensors* **2014,** *14*, 11957-11992.

7.   Mosadegh, B.; Polygerinos, P.; Keplinger, C.; Wennstedt, S.; Shepherd, R. F.; Gupta, U.; Shim, J.; Bertoldi, K.; Walsh, C. J.; Whitesides, G. M., Pneumatic Networks for Soft Robotics that Actuate Rapidly. *Adv. Funct. Mater.* **2014,** *24*, 2163-2170.

8.   Polygerinos, P.; Correll, N.; Morin, S. A.; Mosadegh, B.; Onal, C. D.; Petersen, K.; Cianchetti, M.; Tolley, M. T.; Shepherd, R. F., Soft Robotics: Review of Fluid-Driven Intrinsically Soft Devices; Manufacturing, Sensing, Control, and Applications in Human-Robot Interaction. *Adv. Eng. Mater.* **2017,** *19*, 1700016.

9.   Yu, P.; Fu, W.; Zeng, Q. S.; Lin, J. H.; Yan, C.; Lai, Z. C.; Tang, B. J.; Suenaga, K.; Zhang, H.; Liu, Z., Controllable Synthesis of Atomically Thin Type-II Weyl Semimetal

WTe2 Nanosheets: An Advanced Electrode Material for All-Solid-State Flexible Supercapacitors. *Adv. Mater.* **2017,** *29*, 1701909.

10.	Kang, J. H.; Son, D.; Wang, G. J. N.; Liu, Y. X.; Lopez, J.; Kim, Y.; Oh, J. Y.; Katsumata, T.; Mun, J. W.; Lee, Y.; Jin, L. H.; Tok, J. B. H.; Bao, Z. N., Tough and Water-Insensitive Self-Healing Elastomer for Robust Electronic Skin. *Adv. Mater.* **2018,** *30*, 1706846.

11.	Nela, L.; Tang, J. S.; Cao, Q.; Tulevski, G.; Han, S. J., Large-Area High-Performance Flexible Pressure Sensor with Carbon Nanotube Active Matrix for Electronic Skin. *Nano. Lett.* **2018,** *18*, 2054-2059.

12.	Gao, W.; Emaminejad, S.; Nyein, H. Y. Y.; Challa, S.; Chen, K. V.; Peck, A.; Fahad, H. M.; Ota, H.; Shiraki, H.; Kiriya, D.; Lien, D. H.; Brooks, G. A.; Davis, R. W.; Javey, A., Fully Integrated Wearable Sensor Arrays for Multiplexed In Situ Perspiration Analysis. *Nature* **2016,** *529* , 509.

13.	Cheng, S.; Wu, Z. G., A Microfluidic, Reversibly Stretchable, Large-Area Wireless Strain Sensor. *Adv. Funct. Mater.* **2011,** *21*, 2282-2290.

14.	Scilingo, E. P.; Lorussi, F.; Mazzoldi, A.; De Rossi, D., Strain-Sensing Fabrics for Wearable Kinaesthetic-Like Systems. *IEEE Sens. J.* **2003,** *3*, 460-467.

15.	Hu, J.; Huang, H.; Bai, M.; Zhan, T. T.; Yang, Z. B.; Yu, Y.; Qu, B., A High Sensitive Fiber-Optic Strain Sensor With Tunable Temperature Sensitivity For Temperature-Compensation Measurement. *Sci. Rep.* **2017,** *7*, 42430.

16.	Cai, L.; Song, L.; Luan, P. S.; Zhang, Q.; Zhang, N.; Gao, Q. Q.; Zhao, D.; Zhang, X.; Tu, M.; Yang, F.; Zhou, W. B.; Fan, Q. X.; Luo, J.; Zhou, W. Y.; Ajayan, P. M.; Xie, S.

S., Super-stretchable, Transparent Carbon Nanotube-Based Capacitive Strain Sensors for Human Motion Detection. *Sci. Rep.* **2013,** *3*, 2173.

17.   Radha, B.; Sagade, A. A.; Kulkarni, G. U., Flexible and Semitransparent Strain Sensors Based on Micromolded Pd Nanoparticle-Carbon *µ*-Stripes. *ACS Appl. Mater. Interfaces*   **2011,** *3*, 2173-2178.

18.   Amjadi, M.; Kyung, K. U.; Park, I.; Sitti, M., Stretchable, Skin-Mountable, and Wearable Strain Sensors and Their Potential Applications: A Review. *Adv. Funct. Mater.* **2016,** *26* , 1678-1698.

19.   Prydal, J. I.; Kennard, D. W., Upper Eyelid Movement in Thyrotoxicosis. *Invest Ophth. Vis. Sci.* **2001,** *42*, S67.

20.   Wang, C. F.; Zhao, J.; Ma, C.; Sun, J. L.; Tian, L.; Li, X. Y.; Li, F. T.; Han, X.; Liu, C. T.; Shen, C. Y.; Dong, L.; Yang, J.; Pan, C. F., Detection Of Non-Joint Areas Tiny Strain And Anti-Interference Voice Recognition By Micro-Cracked Metal Thin Film. *Nano Energy* **2017,** *34*, 578-585.

21.   Pang, C.; Lee, G. Y.; Kim, T. I.; Kim, S. M.; Kim, H. N.; Ahn, S. H.; Suh, K. Y., A Flexible and Highly Sensitive Strain-Gauge Sensor Using Reversible Interlocking of Nanofibres. *Nat. Mater.* **2012,** *11*, 795-801.

22.   Kim, K. K.; Hong, S.; Cho, H. M.; Lee, J.; Suh, Y. D.; Ham, J.; Ko, S. H., Highly Sensitive and Stretchable Multidimensional Strain Sensor with Prestrained Anisotropic Metal Nanowire Percolation Networks. *Nano Lett.* **2015,** *15*, 5240-5247.

23.   Li, Y. Q.; Huang, P.; Zhu, W. B.; Fu, S. Y.; Hu, N.; Liao, K., Flexible Wire-Shaped Strain Sensor from Cotton Thread for Human Health and Motion Detection. *Sci. Rep.* **2017,** *7,* 45013.

24.   Bae, S. H.; Lee, Y.; Sharma, B. K.; Lee, H. J.; Kim, J. H.; Ahn, J. H., Graphene-Based Transparent Strain Sensor. *Carbon* **2013,** *51,* 236-242.

25.   Roh, E.; Hwang, B. U.; Kim, D.; Kim, B. Y.; Lee, N. E., Stretchable, Transparent, Ultrasensitive, and Patchable Strain Sensor for Human-Machine Interfaces Comprising a Nanohybrid of Carbon Nanotubes and Conductive Elastomers. *ACS Nano* **2015,** *9,* 6252-6261.

26.   Lee, T.; Lee, W.; Kim, S. W.; Kim, J. J.; Kim, B. S., Flexible Textile Strain Wireless Sensor Functionalized with Hybrid Carbon Nanomaterials Supported ZnO Nanowires with Controlled Aspect Ratio. *Adv. Funct. Mater.* **2016,** *26,* 6206-6214.

27.   Seo, J.; Lee, T. J.; Lim, C.; Lee, S.; Rui, C.; Ann, D.; Lee, S. B.; Lee, H., A Highly Sensitive and Reliable Strain Sensor Using a Hierarchical 3D and Ordered Network of Carbon Nanotubes. *Small* **2015,** *11,* 2990-2994.

28.   Tian, H.; Shu, Y.; Cui, Y. L.; Mi, W. T.; Yang, Y.; Xie, D.; Ren, T. L., Scalable Fabrication Of High-Performance And Flexible Graphene Strain Sensors. *Nanoscale* **2014,** *6,* 699-705.

29.   Feng, W.; Zheng, W.; Gao, F.; Chen, X. S.; Liu, G. B.; Hasan, T.; Cao, W. W.; Hu, P. A., Sensitive Electronic-Skin Strain Sensor Array Based on the Patterned Two-Dimensional alpha-In2Se3. *Chem. Mater.* **2016,** *28,* 4278-4283.

30.   Yan, T.; Wang, Z.; Wang, Y. Q.; Pan, Z. J., Carbon/Graphene Composite Nanofiber Yarns For Highly Sensitive Strain Sensors. *Mater. Design* **2018,** *143*, 214-223.

31.   Lipomi, D. J.; Vosgueritchian, M.; Tee, B. C. K.; Hellstrom, S. L.; Lee, J. A.; Fox, C. H.; Bao, Z. N., Skin-Like Pressure And Strain Sensors Based On Transparent Elastic Films Of Carbon Nanotubes. *Nat. Nanotechnol.* **2011,** *6*, 788-792.

32.   Xia, Y. N.; Whitesides, G. M., Soft Lithography. *Angew. Chem.* **1998,** *37*, 550-575.

33.   Rao, K. D. M.; Gupta, R.; Kulkarni, G. U., Fabrication of Large Area, High-Performance, Transparent Conducting Electrodes Using a Spontaneously Formed Crackle Network as Template. *Adv. Mater. Interfaces* **2014,** *1*, 1400090.

34.   Gupta, N.; Rao, K. D. M.; Gupta, R.; Krebs, F. C.; Kulkarni, G. U., Highly Conformal Ni Micromesh as a Current Collecting Front Electrode for Reduced Cost Si Solar Cell. *ACS Appl. Mater. Interfaces* **2017,** *9*, 8634-8640.

35.   Miyake, H.; Ye, S.; Osawa, M., Electroless Deposition Of Gold Thin Films On Silicon For Surface-Enhanced Infrared Spectroelectrochemistry. *Electrochem. Commun.* **2002,** *4*, 973-977.

36.   Kumar, A.; Kulkarni, G. U., Evaluating Conducting Network Based Transparent Electrodes from Geometrical Considerations. *J. Appl. Phys.* **2016,** *119*, 015102.

37.   Brandon, D. G. Field Evaporation BT - Field-Ion Microscopy; Hren, J. J., Ranganathan, S., Eds.; Springer US: Boston, MA, 1968; 28–52.

38.   Xiang, C.; Kim, J. Y.; Penner, R. M. Reconnectable Sub-5 Nm Nanogaps in Ultralong Gold Nanowires. *Nano Lett.* **2009,** *9* (5), 2133–2138.

Chapter 4

Twisted Multilayer Graphene

4.1 Twist dependent Raman and electron diffraction correlations in twisted multilayer graphene.

4.2 Highly sensitive and stretchable strain sensor based on intrinsically wrinkled twisted multilayer graphene.

Chapter 4.I

Twist Dependent Raman and Electron Diffraction Correlations in Twisted Multilayer Graphene

Summary: In this chapter, a twisted multilayer graphene with high 2D crystallinity was studied using selective area electron diffraction and Raman spectroscopy. The distribution and population of twist angles from distributed sextets in SAED patterns were investigated with the collective Raman behaviour at the same locations. A descriptor, termed as turbostratic factor was calculated based on angular spacings in SAEDs, to account for their distribution; higher the spread, higher the turbostratic factor. Raman spectra have revealed that the turbostratic factor remains low (~0°) for graphitic region with low 2D to G intensity ratio (I_{2D}/I_G) and increases rapidly at higher I_{2D}/I_G values saturating at 60° for highly turbostratic systems. Relating the intensities associated with the sextets and I_{2D}/I_G values, the maximum achievable value of I_{2D}/I_G was found to be 17.92.

4.1.1 Introduction

Twisted graphene, owing to twist angle dependent properties, has attracted a lot of attention over the last few years,[1,2] particularly since the observation of superconductivity in twisted bilayer graphene (tBLG), very recently.[3,4] While with AB

stacking, the pristine properties of single layer graphene (SLG) get gradually suppressed with increasing number of layers bringing modifications in the dispersion relation, in twisted graphene on the other hand, new energy modes arise due to twist angle dependent van Hove singularities (vHSs).[5,6] Further, the dispersion relation remains linear near the 'K' point as the layers remain electronically decoupled thus retaining the valuable properties of the SLG.[7] Studies on such twisted graphene systems have shown that the electronic band structure varies systematically with the twist angle[8,9] and the modified dispersion relation contains optical absorption bands in the visible region.[10–12]

There have been experimental efforts to produce twisted graphene in the form of tBLG[2,13,14] as well as tMLG.[15,16] These are primarily based on nanomanipulation methods wherein two layers are brought together with a predefined twist angle using nanomanipulator.[17] The use of prepatterned substrates with defined hydrophobicity to control the folding of graphene has also been employed to define the twist angle.[18] The AFM tip has been used to controllably fold the graphene layer onto itself with specific twist angles[19] and to rotate it.[20] However, the above lithography based techniques are inherently tedious, incidental and at best, doable for twisted stacks up to two or three layers. However, when it comes to studying diverse angular rotations among layers, a multilayer twisted system is desirable. Indeed, it is predicted recently that tMLGs can show superconductivity at a much higher T_c than the tBLGs.[21]

4.1.2 Scope of the present investigation

The literature of twisted multilayer graphene deals with using either selective area electron diffraction (SAED) or Raman spectroscopy to identify the system. However, both of these experimental techniques have limitations when used standalone. The present work aims to gain more insight into the twisted nature of tMLG, particularly the variation of the twist angles in the system by simultaneously analysing these experimental techniques at the same location of a sample. Also, the twisted multilayer system prepared by the method stated in this chapter, behaves like a single layer even when there is a high percentage (till ~85%) of AB stacking in the system, it has no measurable D band yet exhibiting high I_{2D}/I_G (>5) values, characteristic of the inherent 2D crystallinity of each layer with no interlayer coupling. Thus, it serves as a ready twisted stack but with a spread of twists over the exposed surface, making it a good system to study twisted multilayer system. Carefully relating SAED and Raman measurements at the same locations, the amount of turbostraticity can be quantified, which can further help in understanding such systems. If quantified in a generalised way, other twisted hexagonal multilayer systems can be explored as well.

4.1.3 Experimental Section

Details of sample preparation are described in the results and discussion section. Transmission electron microscopy (TEM) and selected area electron diffraction (SAED) were performed using Technai F30 UHR instrument at 200 kV. Graphene on Ni was etched overnight in $FeCl_3$ solution to get flakes of suspended tMLG which were

transferred onto Cu TEM grids with holey carbon film. Raman spectra were recorded in the backscattered geometry and three lasers were used having excitation wavelengths of 523, 630 and 785 nm (Horiba Raman spectrometer). The Raman scans were taken at 50X objective length with power of 3 mW at the sample surface. A set of markers were used to exactly locate the region for acquiring TEM, SAED and Raman spectra from the same regions.
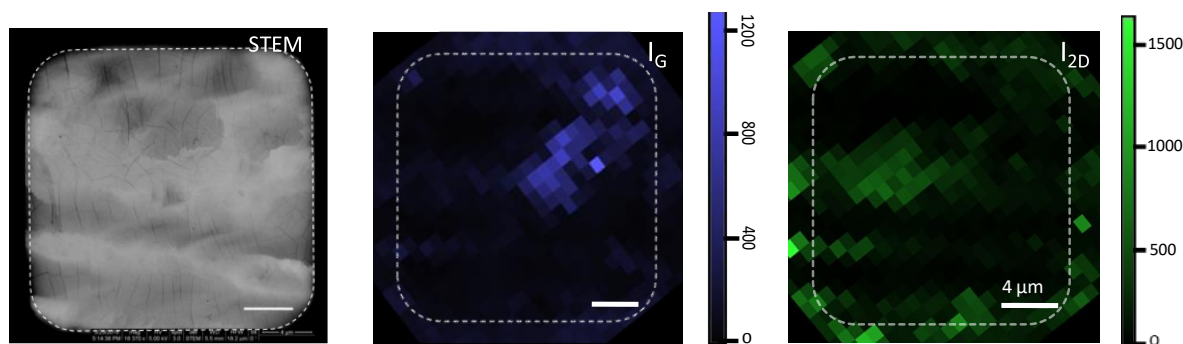
4.1.4 Results and Discussion

Figure 4.1.1 (a) Low magnification STEM image from a 15×15 μm² region of a tMLG flake supported by a TEM grid. Raman mapping was carried out on the same region while the flake continued to be on the grid. Maps of I_G (b) and I_{2D} (c) of the region shown in (a). Scale bar, 4μm.

The synthesis of tMLG follows previous reports,[15] involving rapid Joule heating and cooling of a Ni foil coated with aromatic hydrocarbons in vacuum, Ni serving as a metal catalyst. As Joule heating leads to heating the foil locally (vacuum chamber being at room temperature), the foil could be cooled rapidly within seconds from ~900 °C to below 500 °C during which the dissolved carbon precipitates to form graphene layers on the Ni surface. Due to rapid quenching, the layers tend to stack randomly forming a

non-AB stacked tMLG, conventionally referred to as a turbostratic system.[23] One such tMLG flake was transferred to a TEM grid and scanning transmission electron microscopy (STEM) survey scan imaging was performed, as shown in Figure 4.1.1, to select different regions for further study.

On performing Raman spectral map in the region marked by the white dotted square (area ~200 μm^2, see Figure 4.1.1), the I_{2D}/I_G ratio was found to vary throughout the region (see Figure 4.1.2a), implying that the tMLG has varying extents of AB and twisted stacking. In general, higher values of I_{2D}/I_G can be related to high purity or lower defects or doping concentration[24] in a single layer graphene or to the greater degree of twist between the layers for a tBLG.[25] For a multilayer graphene system such as graphite, the I_{2D}/I_G ratio is typically less than one[26] and a value higher than one is expected to arise due to some degree of rotation between the layers.[27] Accordingly, the three regions, 1-3, having I_{2D}/I_G of ~ 0.6, 3 and 13 respectively (see Raman spectra in Figure 4.1.2b) were identified and termed as graphitic, medium turbostratic and highly turbostratic regions, respectively. In some locations, I_{2D}/I_G as high as ~16 has also been observed (see Figure 4.1.3). In region 1, the 2D peak is split with peaks centred around 2690 and 2720 cm^{-1} (see curve fitting in SI Figure 4.1.4a), implying a significant portion of AB stacked layers in the region (the fitting values are given in Table 4.1.1). On the other hand, the 2D peaks from regions 2 and 3 appear symmetric and centred around 2700 cm^{-1}. A small shoulder is seen at higher wavenumbers in the peak obtained from region 2 but was absent in region 3. Thus, both AB stacked and turbostratic contributions are present in region 2, whereas in region 3, the contribution of AB stacking is negligible.
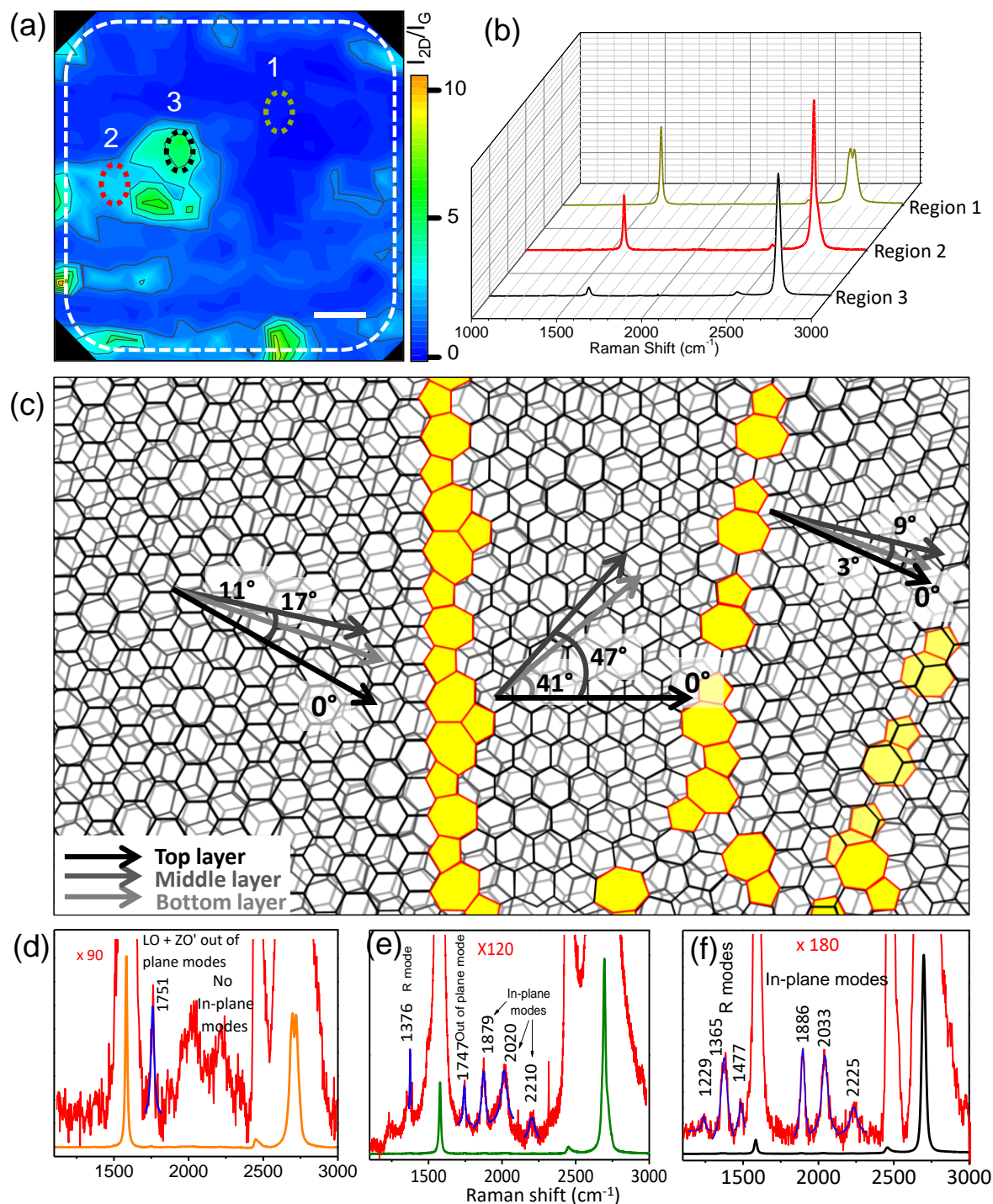
Figure 4.1.2 Landscape of turbostraticity in tMLG. (a) Raman map of I_{2D}/I_G ratio of a twisted multilayer graphene (tMLG) region. Scale bar, 4 μm. (b) Corresponding Raman spectra at region 1 (I_{2D}/I_G ~0.6, graphitic), region 2 (I_{2D}/I_G ~3, medium turbostratic), and region 3 (I_{2D}/I_G ~13, highly turbostratic). The curve fittings are shown in Figure 4.1.4. (c)

Schematic of rotated three graphene layers with varied twist angles. Top, middle, and bottom layers are shown by black, dark grey and light grey colours respectively. Axis along the zig-zag direction (black arrow) are considered as a reference for angle calculation. In the top graphene layer, three regions, I-III, with different rotations are separated by grain boundaries (yellow regions), the middle layer has a grain boundary at the right whereas the bottom layer has the same orientation all over. The twist angles of the middle and bottom layers with respect to three regions of the top layer are indicated with arrows following the same colour scheme as that in layers. The rotations of the middle and bottom layers with respect to the top layer are $17°$ and $11°$ in region I, $47°$ and $41°$ in the region II and $9°$ and $3°$ in the region III respectively. Magnified low lying Raman modes of (d) region 1, (e) region 2 and (f) region 3 respectively marked in (a).
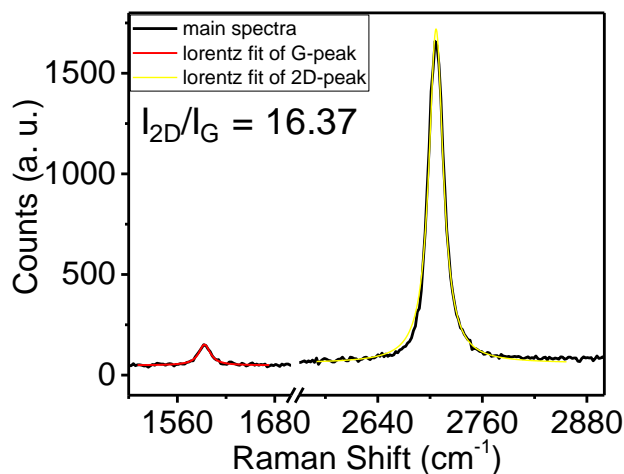
Figure 4.1.3 Raman spectrum of a region with I_{2D}/I_G of ~16. This is the maximum I_{2D}/I_G observed experimentally for our tMLG sample.

The D peak, which is expected to be around 1350 cm^{-1} was not at all observed in any of the regions indicating a high 2D crystallinity of the tMLG. It is well known that

graphene grown by CVD methods are generally polycrystalline in nature with domains separated by line defects. When stacked, the relative orientation of a layer with respect to the adjacent layers is a local quantity and can be highly varied across the area as schematically shown for a 3-layer twisted system (see Figure 4.1.2c). A variation in the twist within a layer, gives rise to a change in mutual twists among the participating layers, thereby leading to varied I_{2D}/I_G. Figure 4.1.2c shows a stack of three layers where the top, middle and bottom layers are shown in black, dark grey and light grey
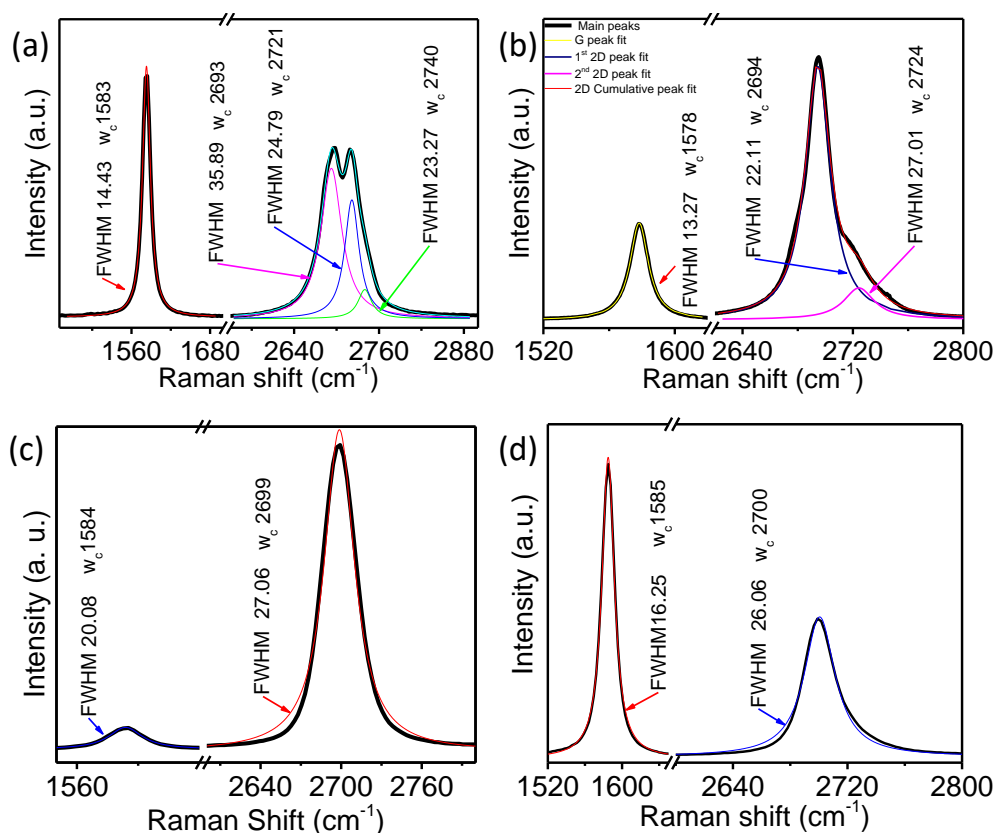
Figure 4.1.4 Curve fitting of G and 2D peaks of Raman of region 1(a), 2(b), 3(c) marked respectively in Figure 1a and G-enhanced(d) region, studied in Figure 6.

Table 4.1.1 Fitting values for G and 2D peaks shown in Figure 4.1.4. Fitness factors are above 0.992.

Type	G cm^{-1}	Width cm^{-1}	2D 1 cm^{-1}	Width cm^{-1}	2D 2 cm^{-1}	Width cm^{-1}	2D 3 cm^{-1}	Width cm^{-1}
Graphitic	1583	14.43	2693	35.89	2421	27.79	2740	23.27
Medium turbostratic	1578	13.27	2694	22.11	2424	27.01		
High tubrotratic	1584	20.08	2699	27.06				
G enhanced	1585	16.25	2700	26.06				

respectively. The top layer hosts three domains separated by line defects marked by yellow regions consisting of seven and five membered rings. The middle layer contains a small line defect towards the right edge while the bottom layer has no line defects. This arrangement gives three possible scenarios marked by sets of arrows, where each arrow is along the zig-zag axis of the respective layer (see Figure 4.1.2c). Although, the illustration emphasises how there is frequent change in the relative rotations giving rise to varying I_{2D}/I_G as seen from the Raman map in Figure 4.1.2a. However, in these tMLG samples, the changes are not frequent and occur over a length scale of μm, despite it being multi-layered and the twists may originate from any of the evolving layers. This is corroborated by the absence of D peak in all over spectrum.

To further ascertain the nature of graphene, deep low-lying Raman modes were examined. The zoomed-in spectra shown in Figures 4.1.2d-f reveal the presence of various low-lying modes. For the graphitic region 1 shown in Figure 4.1.2d, an out-of-plane mode was observed around 1750 cm^{-1} while for a moderately turbostratic region 2, a weak out-of-plane and several in-plane modes were observed, as shown by the red curve in Figure 4.1.2e. The rotational modes termed as R-modes in the literature such as the one at ~1376 cm^{-1} appear due to decoupling among layers which is a signature of twisting and is usually accompanied with high I_{2D}/I_G values.[28] On the other hand, the out-of-plane modes, signifying interaction among the layers, occur when the layers are AB stacked which exhibit a I_{2D}/I_G value less than 1.[26] The presence of both in-plane and out of plane modes gives rise to a moderate I_{2D}/I_G as observed for region 2. In the highly turbostratic region 3, various R modes at around 1477, 1365 and 1229 cm^{-1} were observed (see Figure 4.1.5 for the comparison of intensities of in-plane modes).[28,29] No observable out-of-plane mode was observed in this region as expected for a highly turbostratic system.[30] Instead, the in-plane modes appear distinctly at 1800-2300 cm^{-1} and are highly prominent.

In order to understand how an SAED pattern evolves when a system moves from AB stacked to turbostratic, an SAED pattern of a single layer graphene was considered, i.e. six spots separated by 60° into a sextet. As more layers are AB stacked as in graphite, the sextet becomes brighter progressively. However, in a tMLG, the sextet can also have contributions from layers which may be positioned distantly in the stack but with basis vectors being parallel to the reference, henceforth referred to as substack. On the other

hand, any layer that is twisted with respect to the reference, leads to a new sextet, whose intensity would depend on the number of layers parallel to the former, all together forming another substack. Thus, the presence of several sextets in the SAED pattern represents several possible twists among the substacks with the relative intensities corresponding to their populations. Higher the intensity of a sextet, higher would be the corresponding number of layers oriented parallelly with each other (not necessarily AB stacked adjacent layers) because there is a finite possibility of occurrence of layers that are remotely located avoiding any van der Waals interaction and at the same time are not rotated with respect to each other. Therefore, high intensity of SAED spots need not necessarily mean high AB stacking in the tMLG system. It can be generalised that
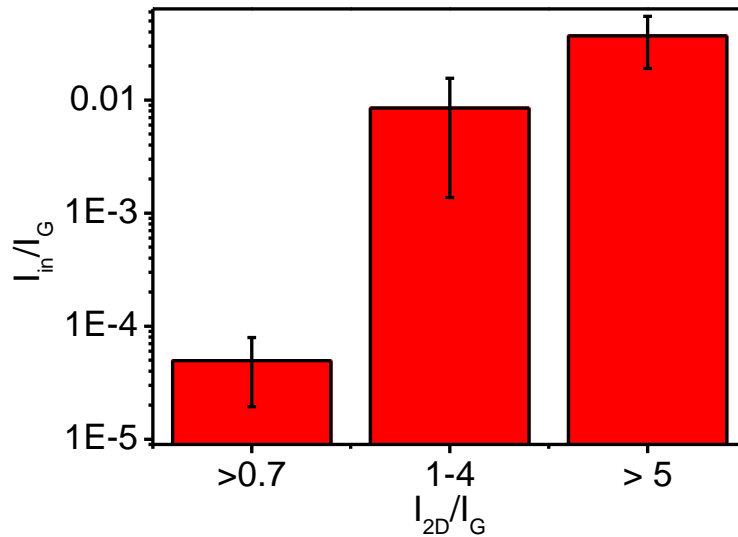
Figure 4.1.5 Intensities of in-plane modes normalised with intensity of G-peak plotted for the graphitic, medium turbostratic and highly turbostratic regions. The histogram was plotted taking 8 samples. As soon as twists are introduced in the system (I_{2D}/I_G), the in-plane mode intensity exponentially increases.
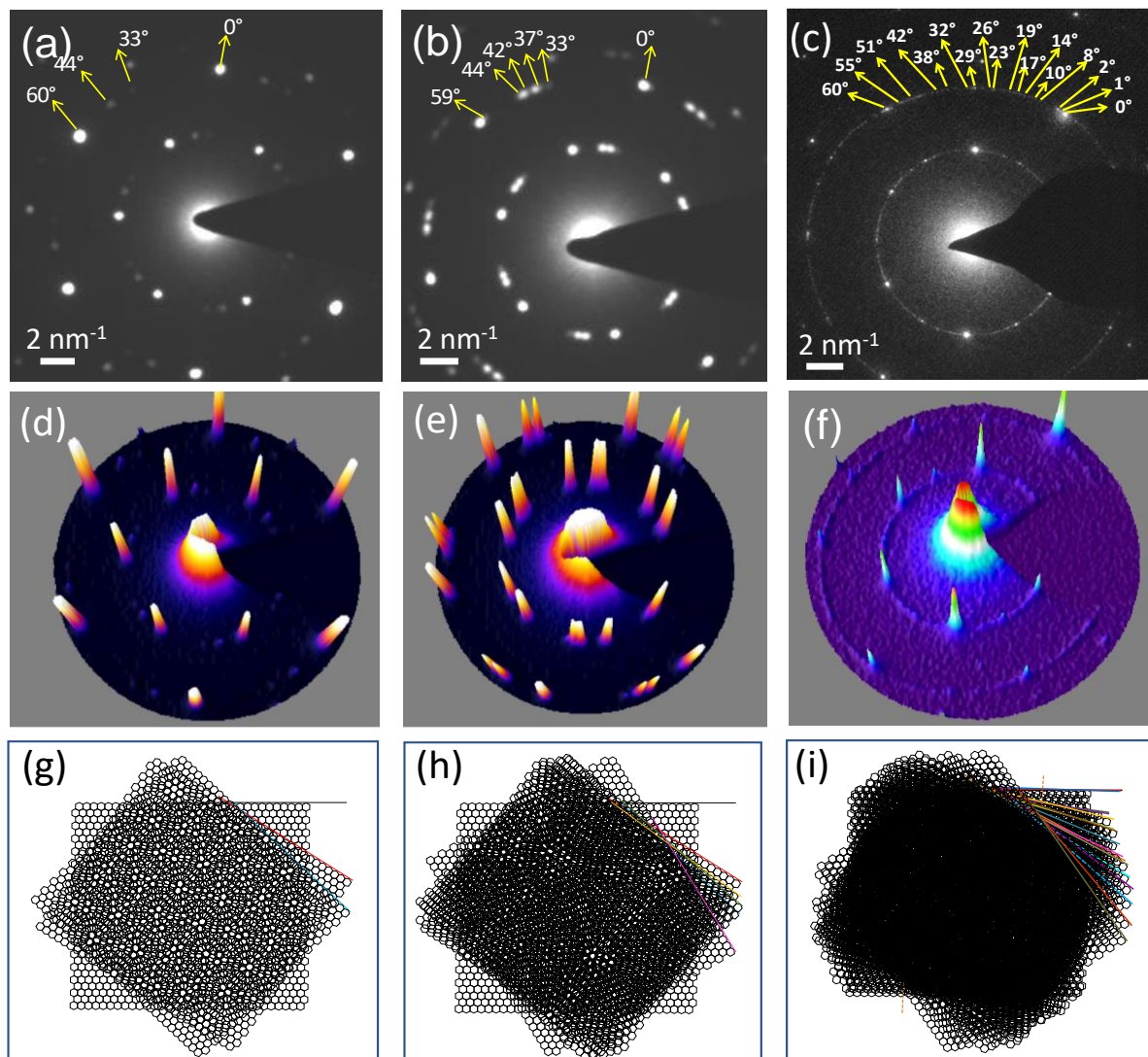
Figure 4.1.6 Diffraction study of tMLG. (a-c) SAED pattern of graphitic, medium turbostratic and highly turbostratic regions respectively as marked by regions 1-3 in Figure 4.1.2a, where arrows represent spots from 0° to 60° with their angles marked. (d-f) 3D profiles of the respective SAED patterns in (a-c). (g-i) Possible layer arrangement of graphene layers for SAEDs in (a-c) where each layer can also be an AB stack.

increased twists (rotations) among the layers may lead to a greater number of sextets, thereby indicating higher turbostraticity. Therefore, for a highly turbostratic system with many layers, the SAED pattern should appear more like a ring, yet with distinct spots.

To correlate the Raman spectra of three different regions of the tMLG to the respective angular spacings, the SAED patterns were acquired by identifying the regions in TEM where Raman measurements had been done (Figures 4.1.6a-c). At region 1 with $I_{2D}/I_G \sim 0.6$, the SAED spots other than the prominent sextet, are associated with negligible intensities and therefore, this region contains mainly the graphitic species (all AB stacked). At region 2 with $I_{2D}/I_G \sim 3$, the SAED shows many in-between spots, which corresponds to a wide range of angles. While in the case of region 3 with $I_{2D}/I_G \sim 13$, the SAED pattern looks more diffuse, the in-between spots exhibit intensities comparable to that of the intense sextet, thus indicating that the contributions to intensity come from nearly equal numbers of layers. A similar SAED pattern for another highly turbostratic region is shown in Figure 4.1.7. The distribution of SAED spots is clearer in the 3D profiles shown in Figures 4.1.6d-f. The profile from region 1 exhibits significant intensity of only one sextet, the others being close to the noise level
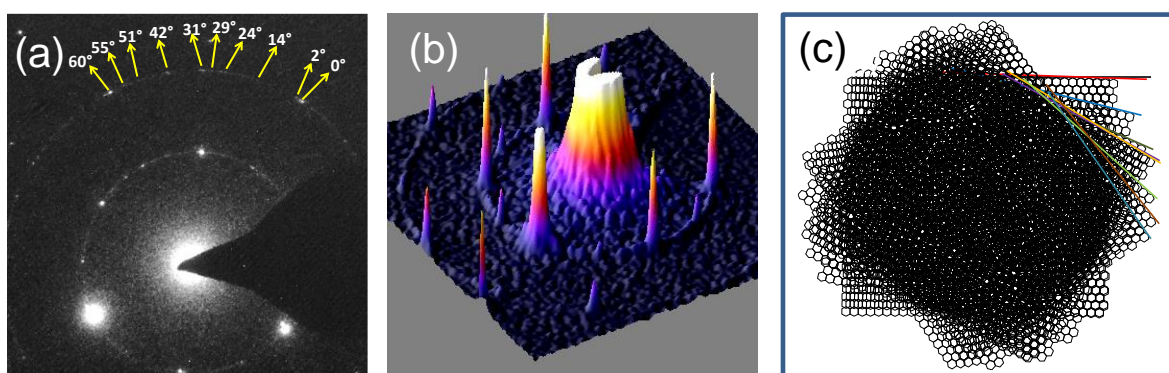
Figure 4.1.7 (a) SAED pattern of region having I_{2D}/I_G of 8 (highly turbostratic), (b) 3D profile of SAED and (c) a possible layer arrangement for the given spots in the SAED pattern. Just like observed in Figure 4.1.6c, the SAED looks like a ring with numerous spots.

representing a graphitic system while that from region 2 shows significant intensities associated with all the twisted sextets. Notably, the profile from region 3 is essentially a ring of spots with little differences in the intensities. Possible arrangements of graphene layers in regions 1-3 are shown in Figures 4.1.6g-i, where each sheet can either be a single layer of graphene or an AB stack, so that the total number of layers remains the same for each region.
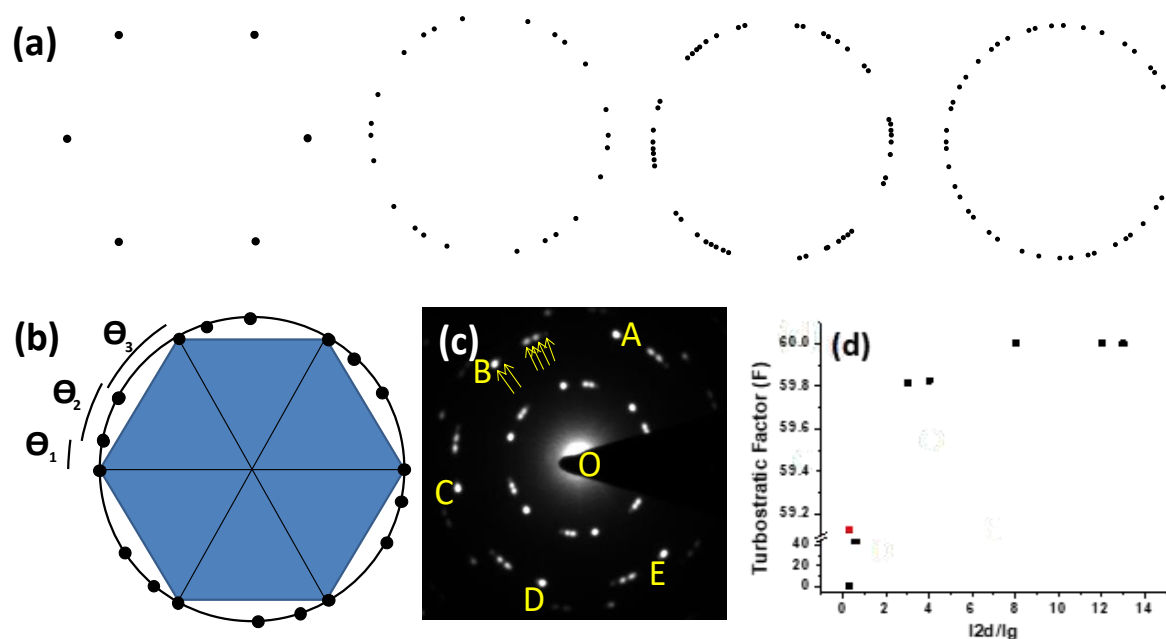

Figure 4.1.8 Defining turbostratic factor. (a) Schematic of SAED patterns for tMLG with increasing number of twist angles. (b) Schematic of SAED having three angular spacings namely Θ_1, Θ_2 and Θ_3. (c) SAED pattern of tMLG having I_{2D}/I_G of 3, with spots in one sextet marked with arrows. The sextets are marked as AOB, BOC, COD and DOE. Angular spacings were calculated and were used to calculate the value of the turbostratic factor, F, for all the SAED patterns. (d) Plot of turbostratic factor versus I_{2D}/I_G. The data point in red is discussed in Figure 6.

It is understood that each graphene layer contributes to six spots in the SAED such that the total number of spots is a multiple of 6 (see Figure 4.1.8a). The SAED of a tBLG system has two sextets and the angle between them can be any of the infinite values between 0° and 60°. A twisted trilayer system on the hand has two twist angles, each of them having infinite possibilities of assuming an angle. When a multilayer system is arrived at, the possibilities of arrangement of the sextets in SAED become numerous and a way is needed to describe the extent of diversity of the twist from region to region. In order to quantify such SAEDs, the number of sextets are considered to be n i.e. there are n number of angular spacings present in a 60° arc such as θ_1, θ_2 and θ_3 as shown in Figure 4.1.8b. Turbostraticity increases with n. For a particular n, the average angular spacing will be the sum of angular spacings of all adjacent spots divided by n.

Turbostraticity increases with decrease in average angular spacing between the neighbouring spots. However, for a constant n, there can be different arrangements of spots. The average angular spacing is constant because the spacings of adjacent spots always add up to 60°. So, a parameter is needed that varies with different arrangements and the twist factor varies consistently with increasing number of spots. It is known that the root mean square of a distribution is zero when all the numbers of distribution are equal and is highest when the numbers are greatly different from each other. Therefore, the root mean square of the spacings of adjacent spots is a parameter which for a constant n, decreases with increase in randomness of spots. More the randomness of spot spacing, more probable it is to have angular spacings closer to the average spot spacing and hence more is the turbostraticity. As the unit of root mean square is same

as angular spacings (degrees), the addition of angular spacing and root mean square is inversely related to the turbostraticity. To make sure that the factor representing the amount of turbostraticity varies consistently with increase in number of spots irrespective of their arrangement, the factor has a denominator of $(n-1)!$. Taking these points into consideration, the following twist factor was arrived at:

$$F = 60° - \frac{\theta_{Avg} + \theta_{RMS}}{(n-1)!} \, ,$$

where θ_{Avg} is the average of spot spacings in a 60° arc, θ_{RMS} is the root mean square value of the spot spacings and n is the number of spot spacings.

There are two limiting cases. For the graphitic (completely AB stacked) and SLG systems, n is 1 and F works out to be 0°. For the other limiting case of a highly turbostratic system, where there are large number of layers having SAED of evenly distributed sextets between 0º to 60º, F tends to 60°. Keeping n constant, the factor maximises when RMS is 0, which is possible when all the spot spacings are equal. And the factor minimises when RMS is maximum which is the case when all the spots are seen concentrated in a narrow angular window.

Calculation of maxima and minima of F for n number of sextets

Suppose in a 60° arc, there are "n" spots, each having angular spacing from its nearest anti-clockwise spot as θ_1, θ_2, θ_3, ... θ_n.

$\therefore \theta_1 + \theta_2 + \theta_3 + ... + \theta_n = 60°$

From this the average spot spacing can be obtained to be $\frac{\theta_1 + \theta_2 + \cdots + \theta_n}{n} = \frac{60}{n}$

Standard deviation of angular spacing of *n* spots from the average (RMS value):

$$= \sqrt{\frac{(\Theta_1-X)^2 + (\Theta_2-X)^2 + (\Theta_3-X)^2 + \cdots + (\Theta_n-X)^2}{n}} \text{ , where } X \text{ is the average i.e. } 60/n$$

Now substituting the values of average spacing and standard deviation in the formula (see Eq. 1), we get

$$\mathcal{F} = 60 - \frac{\frac{60}{n} + \sqrt{\frac{(\Theta_1-X)^2 + (\Theta_2-X)^2 + (\Theta_3-X)^2 + \cdots + (\Theta_n-X)^2}{n}}}{(n-1)!} \qquad \ldots \text{Eq. 2}$$

In order to prove that the value of $\mathcal{F}$ varies consistently and there exists a unique value of $\mathcal{F}$ for every spot arrangement, $\mathcal{F}$ for higher number of spots should always be higher than for lesser number of spots irrespective of their arrangement.

For this, it needs to be proved that,

$$max\mathcal{F}_n > min\mathcal{F}_{n+1} \qquad \ldots \text{ Eq. 3}$$

Maximum of $\mathcal{F}_n$:

The value of $\mathcal{F}_n$ depends on average spot spacing, standard deviation of spot spacings, and number of spots or *n*. For a fixed n, the average spot spacing, and number of spots are fixed.

It is known that, $\mathcal{F}_n = 60 - \frac{(Avg + RMS)}{(n-1)!}$

$\therefore max\, \mathcal{F}_n = 60 - min\, \frac{(Avg + RMS)}{(n-1)!}$

$\Rightarrow max\, \mathcal{F}_n = 60 - \dfrac{Avg\, +\, min(RMS)}{(n-1)!}$ [because for a fixed number of spots, the average and

n are fixed]

Therefore, for $\mathcal{F}_n$ to be maximum, the value of standard deviation should be zero as it cannot be negative.

When $\theta_1 = \theta_2 = \theta_3 = \cdots = \theta_{n+1} = X$, the standard deviation is zero as explained below:

Average spot spacing $= \dfrac{60}{n+1} = \dfrac{(n+1)X}{(n+1)} = X$ $\qquad$ ... Eq. 4

Standard deviation of "n" spots from the average $=$

$\dfrac{1}{n+1}\sqrt{(n + 1)(X^2 + X^2 + X^2 + \cdots + X^2) - 60^2}$

$= \dfrac{1}{n+1}\sqrt{(n + 1)^2 X^2 - 60^2}$

$= \dfrac{1}{n+1}\sqrt{60^2 - 60^2}$

$= 0$

$max\, \mathcal{F}_n = 60 - \dfrac{\frac{60}{n}+0}{(n-1)!} = 60 - \dfrac{60}{n!}$ $\qquad$ .. substituting in Eq. 1

Minimum of $\mathcal{F}_{n+1}$:

Now, because, $\mathcal{F}_{n+1} = 60 - \dfrac{(Avg\, +\, RMS)}{n!}$

$\therefore\ min\ \mathcal{F}_{n+1} = 60 - max\,\dfrac{(Avg\, +\, RMS)}{n!}$

$$\Rightarrow min\ \digamma_{n+1} = 60 - \frac{Avg + max(RMS)}{n!}$$

The maximum standard deviation for a set of spots will occur when all the spots instead of randomly distributed all over the arc are concentrated at one point. This can be expressed by considering all the spots to be closely spaced (at $a°$ each) at the anti-clock end of the arc, where "a" can be minimised for calculating maximum *RMS*.

$\therefore$For *n+1* such spots, $\theta_1 = \theta_2 = \theta_3 = \cdots = \theta_n = a$

$$\Rightarrow \theta_1 + \theta_2 + \theta_3 + \cdots \theta_n + \theta_{n+1} = 60°$$
$$\Rightarrow an + \theta_{n+1} = 60°$$
$$\Rightarrow \theta_{n+1} = 60° - an$$

$$\text{RMS} = \sqrt{\frac{(a-X)^2 + (a-X)^2 + \ldots + (a-X)^2 + (60-an-X)^2}{n}}$$

$$= \sqrt{\frac{(a^2 + X^2 - 2aX)n + 60^2 + a^2 n^2 + X^2 - 120an - 120X - 2anX}{n+1}}$$

$$= \sqrt{\frac{a^2 n + X^2 n - 2aXn + 60^2 + a^2 n^2 + X^2 - 120an - 120X - 2anX}{n+1}}$$

$$= \sqrt{\frac{a^2 n + X^2 n + 60^2 + a^2 n^2 + X^2 - 120an - 120X}{n+1}}$$

$$= \sqrt{\frac{a^2 n + \frac{60^2}{n+1} + 60^2 + a^2 n^2 - 120an - 120\cdot\frac{60}{n+1}}{n+1}}, \text{ substituting } X = \frac{60}{n+1}$$

$$= \sqrt{\frac{a^2 n - \frac{60^2}{n+1} + 60^2 + a^2 n^2 - 120an}{n+1}}$$

$$= \sqrt{\frac{a^2n^2 + a^2n + a^2n^3 + a^2n^2 - 60^2 - 120an^2 - 120an + 60^2n + 60^2}{(n+1)^2}}$$

$$= \frac{\sqrt{n}}{n+1}\sqrt{a^2n^2 + 2a(a-60)n + (a-60)^2}$$

$$= \frac{\sqrt{n}}{n+1}|an + a - 60|$$

For maximising RMS, a should be minimised which can be achieved when a tends to

0.

$$\therefore \ min \ F_{n+1} = 60 - \frac{Avg + max(RMS)}{n!}$$

$$= 60 - \frac{\frac{60}{n+1} + \frac{\sqrt{n}}{n+1}|an + a - 60|}{n!}$$

$$= 60 - \frac{60 + \sqrt{n}\,|an + a - 60|}{(n+1)!}$$

To prove the uniqueness of F, it needs to be proved that

$$60 - \frac{60}{n!} < 60 - \frac{60 + \sqrt{n}\,|an + a - 60|}{(n+1)!} \ , \text{ by substituting in eq. 3}$$

Or, $\dfrac{60 + \sqrt{n}\,|an + a - 60|}{(n+1)!} < \dfrac{60}{n!}$

Or, $\dfrac{60 + \sqrt{n}\cdot 60}{(n+1)!} < \dfrac{60}{n!}$

Or, $1 + \sqrt{n} < n + 1$

Or, $\sqrt{n} < n$

Which is always true for any value of n.

Hence proved that $max \mathcal{F}_n > min \mathcal{F}_{n+1}$

Therefore, for any possible arrangement of ED spots $\mathcal{F}_n > \mathcal{F}_{n+1}$ and there exists a unique value of the turbostratic factor.
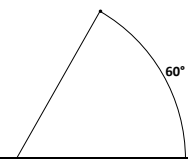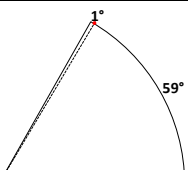
Table 4.1.2 Spot angles and their angular spacings with adjacent ones in the SAED pattern of Figures 4.1.8c-d.

	Spots in AOB (°)	Spots in BOC (°)	Spots in COD (°)	Spots in DOE (°)	Common spots (°)	Spot spacings (°)
A/B/C/D	0	0	0	0	0	33
I	33	34	33	33	33	5
II	37	38	38	38	38	4
II	42	43	42	42	42	2
IV	44	45	44	44	44	15
V	59	59	-	59	59	1
B/C/D/E	60	60	60	60	60	
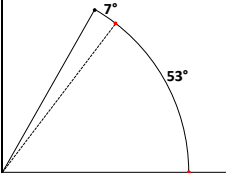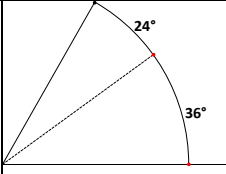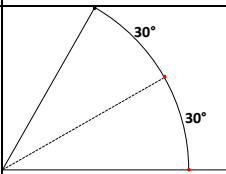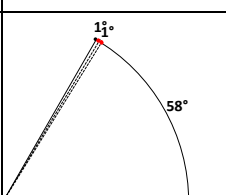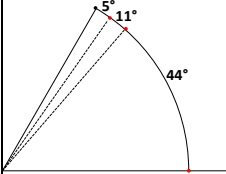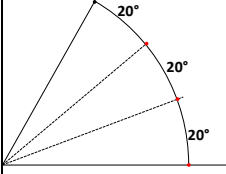
Calculating the minimum and maximum values of $\mathcal{F}$ for various n, it was observed that the maximum value of $\mathcal{F}$ for n sextets is always smaller than the minimum value for $n + 1$ sextets, hence allowing $\mathcal{F}$ to be unique for any arrangement of spots. For the SAED in Figure 4.1.8c, $n = 6$, with angular spacings of 33°, 5°, 4°, 2°, 15° and 1° (details in Table 4.1.2). The sector COD does not show the spot at 59° may be because it is merged with the intense spot at D and is difficult to resolve. The angular spacings were calculated by subtracting the positions of adjacent spots i.e. $\theta_{II} - \theta_I$, $\theta_{III} - \theta_{II}$, etc. From these spot
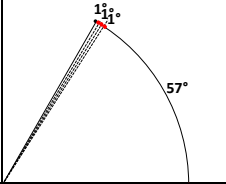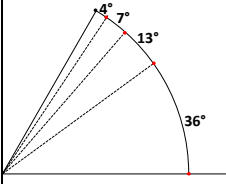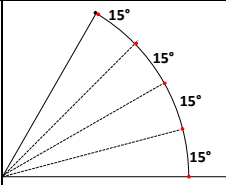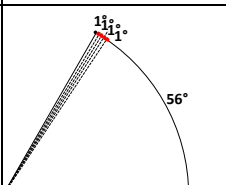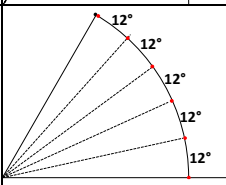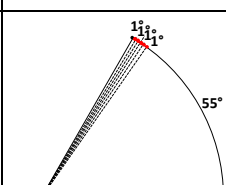
spacings, the average and the RMS values were calculated to be 10° and 12.33° respectively. Dividing their sum by the 6!, the value was obtained to be 59.82°. Similarly, the values of F were calculated for several other SAED patterns and these values have been plotted against the corresponding I_{2D}/I_G as shown in Figure 4.1.8d. As is evident from this plot, F rises monotonically with I_{2D}/I_G except for the data point at I_{2D}/I_G of 0.3 (discussed further in Figure 4.1.12). In other words, the I_{2D}/I_G increases with increase in turbostraticity of the system. While this observation pertains to an excitation wavelength of 532 nm, it may be the case with other wavelengths as well. Monotonic variation of the I_{2D}/I_G has been reported for SLG systems.[31] Table 4.1.3 shows the value of F calculated for various possible arrangements of spots. It is remarkable that F truly stands for the twisted nature of the system.

Table 4.1.3 Calculating manually the Turbostratic factor for few possible spot arrangements.
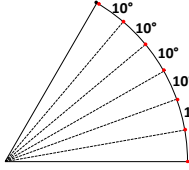
Sr. #	# layers	# spots spacings	Spot angular separation	Schematic of spots on 60° arc	Average	RMS	F
1	2	1	60°		60°	0°	0°
2	3	2	1°, 59°		30°	29.0°	1°

3	3	2	7°, 53°		30°	23.0°	7.00°
4	3	2	24°, 36°		30°	6.0°	24.00°
5	3	2	30°, 30°		30°	0°	30.00°
6	4	3	1°, 1°, 58°		20°	26.9°	36.57°
7	4	3	5°, 11°, 44°		20°	16.2°	41.43°
8	4	3	20°, 20°, 20°		20°	0°	50.00°

9	5	4	1°, 1°, 1°, 57°		15°	24.2°	53.46°
10	5	4	4°, 7°, 13°, 36°		15°	12.5°	56.98°
11	5	4	15°, 15°, 15°, 15°		15°	0°	57.50°
12	6	5	1°, 1°, 1°, 1°, 56°		12°	58.0 °	58.58°
13	6	5	12°, 12°, 12°, 12°, 12°		12°	0°	59.50°
14	7	6	1°, 1°, 1°, 1°, 1°, 55°		10°	20.1°	59.75°

15	7	6	10°, 10°, 10°, 10°, 10°, 10°		10°	0°	59.92°
16	61	60	{1°, 1°..... 1°} 60 times		1°	0°	60°

Explanation by examples:

Example 1. A set of five twisted layers gives us four spots in a 60° arc that are repeated 6 times in the ring of spots of ED. There are many ways in which these four spots can be arranged in the ring. Two possible arrangements of four spots as mentioned in Sr #10 and #11 of Table 4.1.3 are shown schematically below:
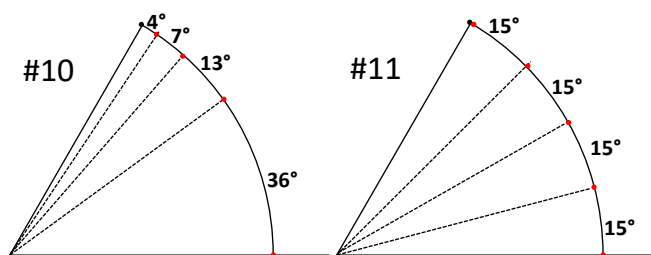
In arrangement shown in Sr #10, the spots are little clustered towards anticlockwise end of the arc compared to that shown in Sr #11 which is evenly spaced. This is reflected by the higher RMS of the spot spacings in Sr #10 (12.5°) compared to that in Sr# 11 (0°). As a result, Ƒ or turbostraticity is higher for Sr# 10 (56.98°) than that for Sr #11 (57.50°).
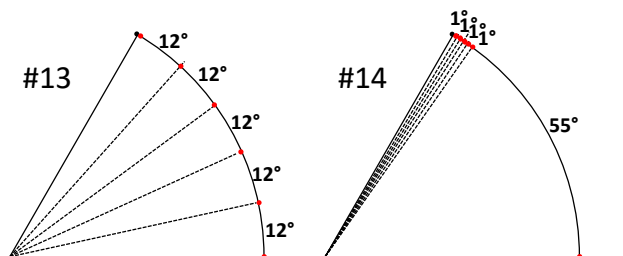
Example 2. The turbostraticity factor increases with increase in number of spots in the SAED irrespective of the evenness or clustering. For example, comparing the arrangements shown in Sr #13 and 14, it is found that the arrangement in Sr# 14 is highly clustered but because it contains a single extra spot compared to that in Sr# 13, the value of F is higher for the arrangement in Sr# 14 (59.75°) than in Sr# 13 (59.50°). This is taken care by the denominator of (n-1)! term in the turbostraticity factor definition for the arrangement in Sr#14.

Having illustrated experimental examples of arriving at F values, it remains to be seen, what are the ranges of F values for varying numbers of sextets. Figure 4.1.9 represents the aspect of angular arrangements, where for each n, few possible sextet arrangements are expressed as arcs of different radii and the angular spacings for each are marked as arc segments on a 60° arc. The radius of the arc increases with increasing value of F. Higher the radius, higher is the turbostraticity in the system. As can be seen in Figure 4a, the centre of the arc, which has essentially zero radius, is the case of AB stacked graphene corresponding to $F = 0°$. If there is a slight twist of 1° in at least one of the layers, which gives rise to angular spacings of 1° and 59°, F rises to 1° (see red arc in Figure 4.1.9a). As the spot spacings become more evenly spread (approaching the purple arc), the *RMS* approaches 0° and F maximises at 30° for $n = 2$. Similarly, as expressed in

Figures 4.1.9b and c, *F* varies from 35.86° to 50° for *n* = 3 and from 53.17° to 57.5° for *n* = 4 respectively. The ranges for different values of *n* are shown in Figure 4.1.9d. The formulation of *F* ensures that each spot arrangement has its unique value.

Another aspect of the SAED pattern is the relative intensities of the sextets, which as noted earlier, represent the relative population of layers corresponding to a particular twist. Given this, the most intense sextet representing maximum layers in AB stacking may be treated as the reference system against which stacks hosting lesser number of AB stacked layers could be compared. The relative intensities of all such
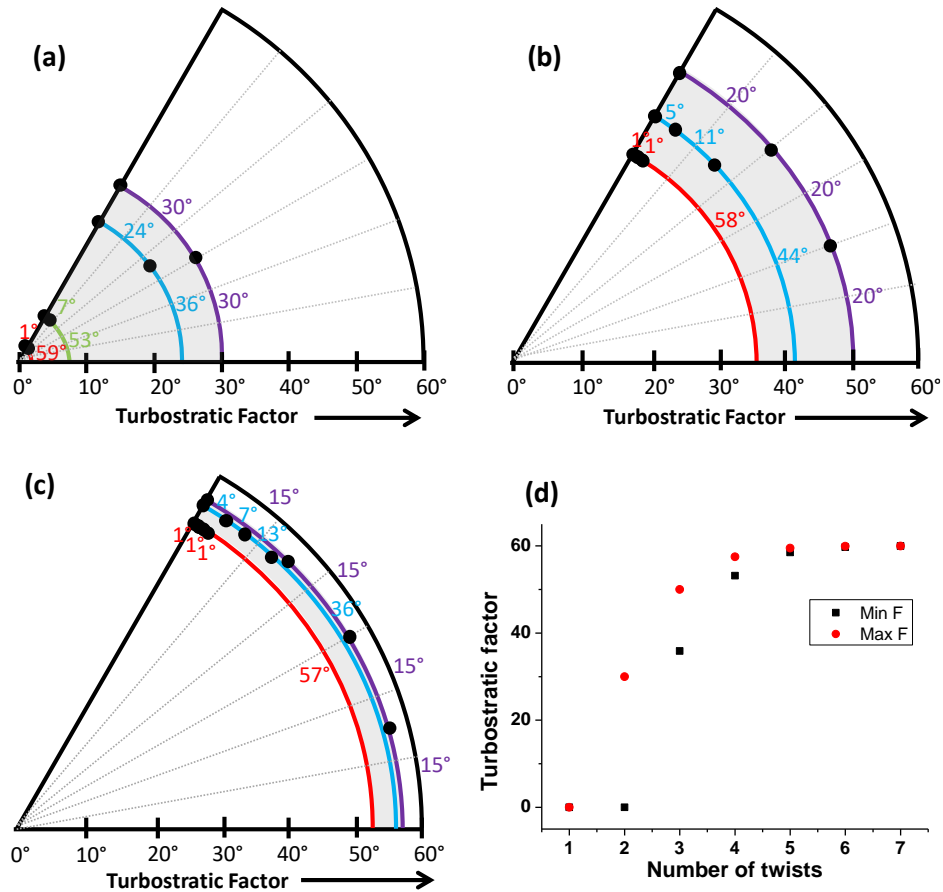

Figure 4.1.9 Angular spread analysis of SAEDs. Representation of possible variations in angular separation for a particular value of *n*, where turbostratic factor is shown on the radius of a pie and the angular separation on the arc segments of the pie for (a) *n*=2,

(b) $n=3$ and (c) $n=4$. The radial lines are graduations at the interval of 10. (d) Plot showing the minimum and maximum value of F plotted for values of n (number of twists or spot spacings). The minimum values for each n, are calculated by the formula, $\frac{60}{n}\left(1+\sqrt{n-1}\right)$ and the minimum values are calculated by the formula, $60-\frac{60}{n!}$.

.
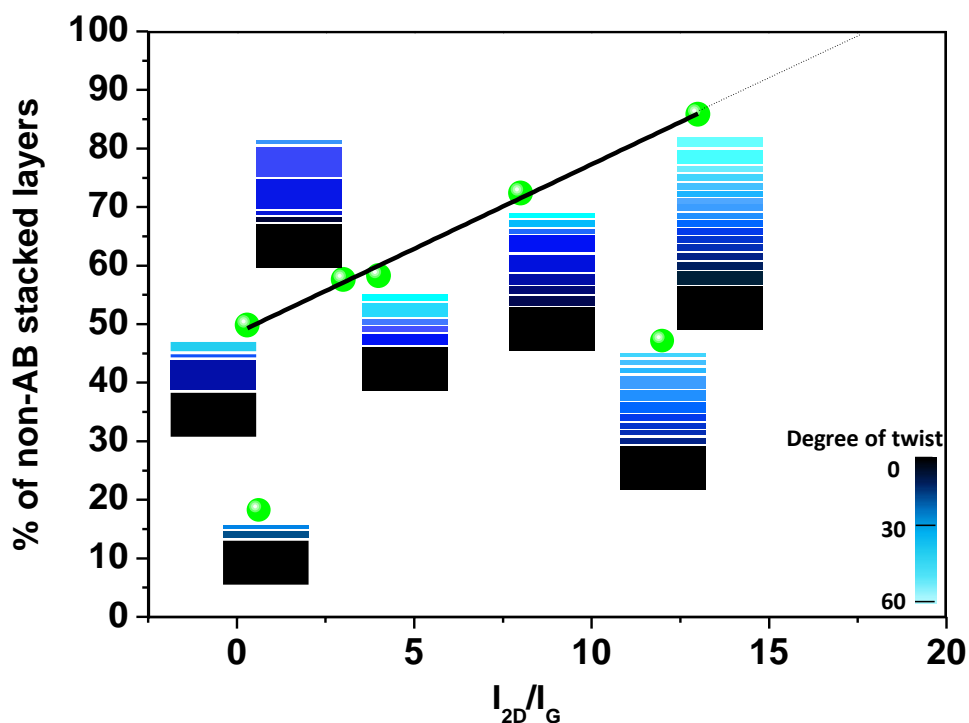
Figure 4.1.10 Intensity analysis of SAEDs. Plot of percentage of non-AB stacked layers in the tMLG sample (in relation to the control) calculated from the intensities of SAED spots, versus the I_{2D}/I_G values from their corresponding Raman maps. Inset shows 2D schematics of layer arrangement in tMLG where the bottom most slab is black in colour having a fixed thickness, the number of slabs above should correspond to number of twisted sextets, width of a slab built up is relative to relative intensities of its sextets, the colour of the other slabs corresponds to the twist of the sextet with respect to the other slabs. The position of the slabs in the stack goes with the twist estimated in clockwise fashion.

sextets twisted with respect to the reference were added and expressed as percentage of the total intensity in SAED which is essentially the percentage of non-AB stacked layers with respect to the reference substack. This value is plotted against the I_{2D}/I_G values as shown in Figure 4.1.10. Most systems lie on a straight line with a positive slope meaning that for a higher I_{2D}/I_G, there are a greater number of twisted layers in the tMLG.

Therefore, a higher I_{2D}/I_G value not only corresponds to a wider spread of twists but also to a higher number of twisted layers in the system. There are two ways in which the layers could be stacked, either following the linear relation or corresponding to a data point below the line. The first one refers to a scenario where several AB substacks with comparable thicknesses stack, involving different twists as shown schematically in the insets of Figure 4.1.10. As can be seen from the trend in Figure 4.1.10, as the I_{2D}/I_G value increases, the colour gradient, from black to cyan, becomes smoother, indicating a good spread of twists in the stack while the variation in the thickness of substacks decreases. The second scenario relates to a thick AB sub-stack with all adjacent twisted substacks having fewer layers compared to the reference substack. This system is majorly an AB stacked system but because of a variety of twists, it exhibits high I_{2D}/I_G. Extrapolating the linear fit, it is observed that the percentage of non-AB stacked layers reaches the highest value of 100% for I_{2D}/I_G value of 17.92 representing a system with highest turbostraticity, where every substack is only one layer thick and is twisted. Importantly, this is a limiting case of I_{2D}/I_G, being reported for the first time. Experimentally, highest I_{2D}/I_G of 16 has been achieved (see Figure 4.1.3). Recently, Luong

et. al. have reported I_{2D}/I_G of 17 in their best tMLG sample prepared by flash joule heating method, which is in good agreement with prediction made in Figure 4.1.10.[32] At the lower end, *i.e.* for low turbostratic system ($I_{2D}/I_G < 1$), the percentage of AB stacked layers can be anywhere between 50% - 100% but not less than 50%, or in other words, at least half of the layers in a system remain AB stacked for a weakly turbostratic system with I_{2D}/I_G close to 0. The Raman spectrum is extremely sensitive to the presence of the twisted layers. Even 10% of the twisted layers can make the feature due to AB stacking disappear in the background due to relatively lower intensity associated with the 2D features (see Figure 4.1.11).
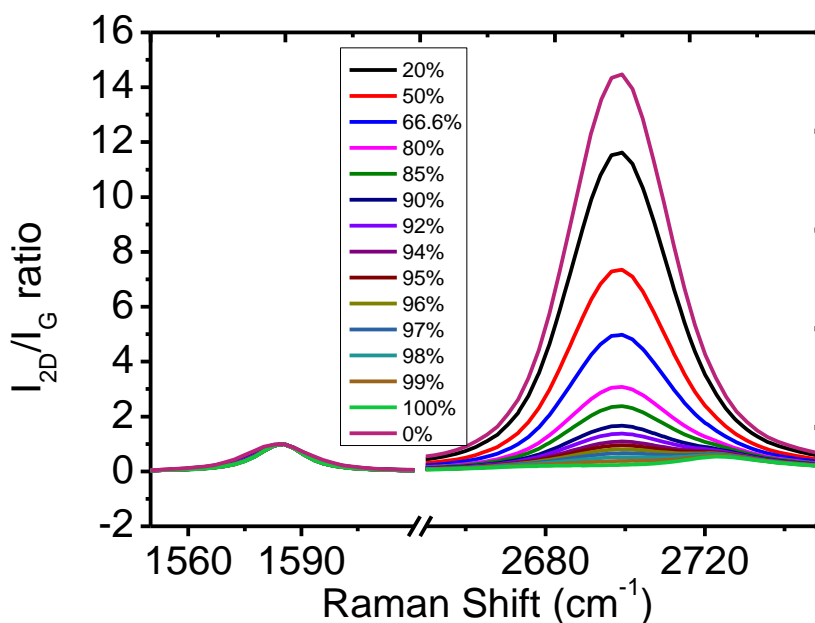

Figure 4.1.11 Raman spectra of a graphitic region and a highly turbostratic region (I_{2D}/I_G = 14) were normalised and added with different percentages of the turbostratic one to understand how much contribution from 2D peak of graphitic Raman is required to show a shoulder.
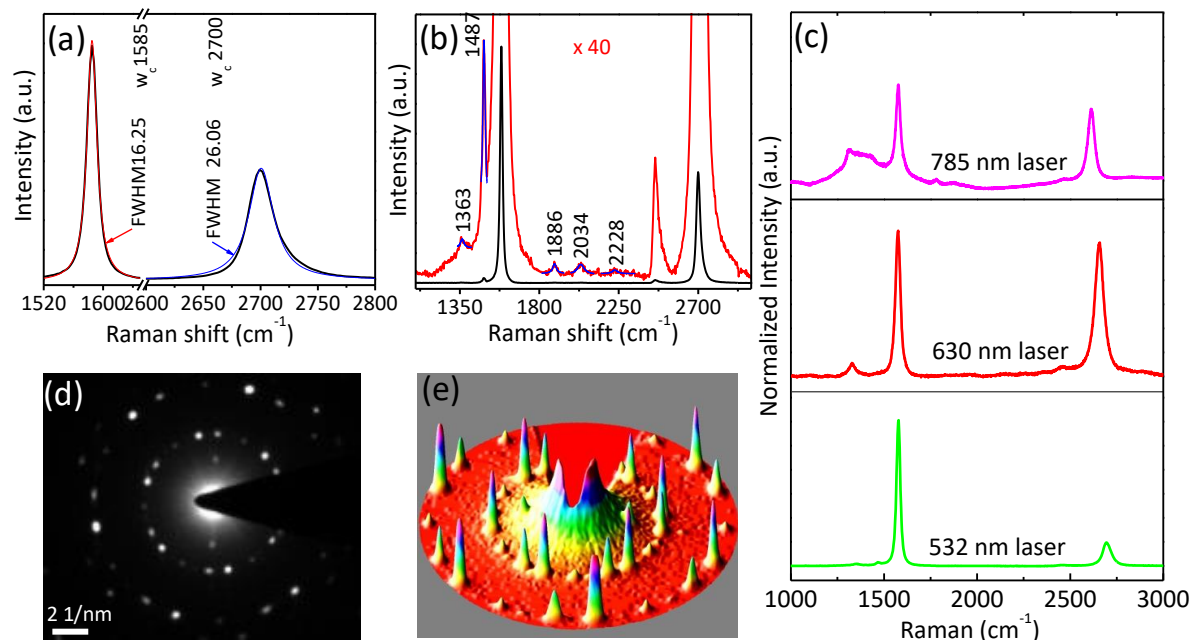
Figure 4.1.12 Study of G-enhancement. (a) Raman spectra of G-enhancement region with Lorentzian fitting. (b) Magnified low lying Raman mode of the spectra given in (a). (c) The Raman spectra in the same region with different Raman laser wavelengths. The SAED image and its 3D profile is shown in (d) and (e) respectively.

It was noted from Figure 4.1.8d that the SAED corresponding to $I_{2D}/I_G \sim 0.3$, does not follow the trend of values varying with the I_{2D}/I_G. The Raman spectrum from this region (Figure 4.1.12a), shows an unusually strong G peak relative to the 2D peak, which is not graphitic in origin as the 2D peak is a single Lorentzian (FWHM ~ 26 cm^{-1}). It arises due to G enhancement via a van Hove singularity.[12,15] Such an enhancement is expected if the layers involved are twisted by an angle of ~13° and if green laser ($\lambda = 532$ nm) is used as the excitation source. In the enhancement region, the G peak intensity is much higher than that compared to other regions. A prominent peak at 1487 cm^{-1} was found, assigned to the R mode, along with other low-intensity peaks (Figure 4.1.12b). Further,

the absence of any out-of-plane modes in the region ensures that the lesser I_{2D}/I_G value is not because of graphitic interaction. Recently, it has become customary to use different laser wavelengths to ascertain the presence of G-enhancement.[27] From Figure 4.1.12c, we observe that for wavelengths of 630 and 785 nm, the G counts decreased gradually relative to the 2D counts.[33] There are other examples of SAEDs, where in spite of angular spacings of 13°, no G-enhancement is observed. This is possible if the participating layers, related by 13° twist, get placed not being adjacent but being far from each other in the tMLG stack.

4.1.5 Conclusions

In conclusion, the study has provided insights into a tMLG system, in particular about the landscape of twists, among and within its layers. By carrying out Raman spectroscopy and SAED in the same locations, the I_{2D}/I_G values were able to be related with the twist angles. A means of treating the twists in tMLG was discovered by defining a new descriptor termed as, turbostratic factor, f, which signifies the various ways of ordering the angular spacings in a SAED. When plotted against I_{2D}/I_G, f shows a monotonic increase which signifies that the SAED of a system with higher turbostraticity has a higher number of spots that are randomly spaced. Thus, this study has provided a clear trend hitherto not known and it is widely applicable to other 2D systems, particularly to the samples produced by techniques such as CVD, where the spread of twists is an inherent nature of the process. The intensity analysis of SAEDs confirms that the turbostraticity of a system is higher not only when there is a range of

twists, but also when the number of twisted layers is greater. Through this analysis, maximum achievable value of I_{2D}/I_G for a tMLG system (and perhaps applicable even for SLG) was predicted for the first time, which is 17.92. At certain twists, G-enhancement was observed which stands out from the trend between f and I_{2D}/I_G indicating the other phenomena involved in a twisted multilayer system, later confirmed by using lasers of various wavelengths.

4.1.6 References

(1)   Ohta, T.; Robinson, J. T.; Feibelman, P. J.; Bostwick, A.; Rotenberg, E.; Beechem, T. E. Evidence for Interlayer Coupling and Moire' Periodic Potentials in Twisted Bilayer Graphene. *Phys. Rev. Lett.* **2012**, *109* (18), 186807.

(2)   Mogera, U.; Kulkarni, G. U. A New Twist in Graphene Research: Twisted Graphene. *Carbon* **2020**, *156*, 470–487.

(3)   Cao, Y.; Fatemi, V.; Fang, S.; Watanabe, K.; Taniguchi, T.; Kaxiras, E.; Jarillo-Herrero, P. Unconventional Superconductivity in Magic-Angle Graphene Superlattices. *Nature* **2018**, *556*, 43.

(4)   Lian, B.; Wang, Z.; Bernevig, B. A. Twisted Bilayer Graphene: A Phonon-Driven Superconductor. *Phys. Rev. Lett.* **2019**, *122* (25), 257002.

(5) Li, G.; Luican, A.; Lopes dos Santos, J. M. B.; Castro Neto, A. H.; Reina, A.; Kong, J.; Andrei, E. Y. Observation of Van Hove Singularities in Twisted Graphene Layers. *Nat. Phys.* **2010**, *6* (2), 109–113.

(6) Yan, W.; Liu, M.; Dou, R.-F.; Meng, L.; Feng, L.; Chu, Z.-D.; Zhang, Y.; Liu, Z.; Nie, J.-C.; He, L. Angle-Dependent van Hove Singularities in a Slightly Twisted Graphene Bilayer. *Phys. Rev. Lett.* **2012**, *109* (12), 126801.

(7) Lopes dos Santos, J. M. B.; Peres, N. M. R.; Castro Neto, A. H. Graphene Bilayer with a Twist: Electronic Structure. *Phys. Rev. Lett.* **2007**, *99* (25), 256802.

(8) Brihuega, I.; Mallet, P.; González-Herrero, H.; Trambly de Laissardière, G.; Ugeda, M. M.; Magaud, L.; Gómez-Rodríguez, J. M.; Ynduráin, F.; Veuillen, J.-Y. Unraveling the Intrinsic and Robust Nature of van Hove Singularities in Twisted Bilayer Graphene by Scanning Tunneling Microscopy and Theoretical Analysis. *Phys. Rev. Lett.* **2012**, *109* (19), 196802.

(9) MacDonald, A. H.; Bistritzer, R. Graphene Moiré Mystery Solved? *Nature* **2011**, *474* (7352), 453–454.

(10) Moon, P.; Koshino, M. Optical Absorption in Twisted Bilayer Graphene. *Phys. Rev. B* **2013**, *87* (20), 205404.

(11) Nair, R. R.; Blake, P.; Grigorenko, A. N.; Novoselov, K. S.; Booth, T. J.; Stauber, T.; Peres, N. M. R.; Geim, A. K. Fine Structure Constant Defines Visual Transparency of Graphene. *Science (80-.).* **2008**, *320* (5881), 1308 LP – 1308.

(12) Mak, K. F.; Sfeir, M. Y.; Wu, Y.; Lui, C. H.; Misewich, J. A.; Heinz, T. F. Measurement of the Optical Conductivity of Graphene. *Phys. Rev. Lett.* **2008**, *101* (19), 196405.

(13) Ni, Z.; Liu, L.; Wang, Y.; Zheng, Z.; Li, L.-J.; Yu, T.; Shen, Z. G-Band Raman Double Resonance in Twisted Bilayer Graphene: Evidence of Band Splitting and Folding. *Phys. Rev. B* **2009**, *80* (12), 125404.

(14) Ni, Z.; Wang, Y.; Yu, T.; You, Y.; Shen, Z. Reduction of Fermi Velocity in Folded Graphene Observed by Resonance Raman Spectroscopy. *Phys. Rev. B* **2008**, *77* (23), 235403.

(15) Mogera, U.; Dhanya, R.; Pujar, R.; Narayana, C.; Kulkarni, G. U. Highly Decoupled Graphene Multilayers: Turbostraticity at Its Best. *J. Phys. Chem. Lett.* **2015**, *6* (21), 4437–4443.

(16) Wu, J.-B.; Zhang, X.; Ijäs, M.; Han, W.-P.; Qiao, X.-F.; Li, X.-L.; Jiang, D.-S.; Ferrari, A. C.; Tan, P.-H. Resonant Raman Spectroscopy of Twisted Multilayer Graphene. *Nat. Commun.* **2014**, *5* (1), 5309.

(17) Chen, X.-D.; Xin, W.; Jiang, W.-S.; Liu, Z.-B.; Chen, Y.; Tian, J.-G. High-Precision Twist-Controlled Bilayer and Trilayer Graphene. *Adv. Mater.* **2016**, *28* (13), 2563–2570.

(18) Wang, B.; Huang, M.; Kim, N. Y.; Cunning, B. V; Huang, Y.; Qu, D.; Chen, X.; Jin, S.; Biswal, M.; Zhang, X.; et al. Controlled Folding of Single Crystal Graphene. *Nano Lett.* **2017**, *17* (3), 1467–1473.

(19) Carozo, V.; Almeida, C. M.; Fragneaud, B.; Bedê, P. M.; Moutinho, M. V. O.; Ribeiro-Soares, J.; Andrade, N. F.; Souza Filho, A. G.; Matos, M. J. S.; Wang, B.; et al. Resonance Effects on the Raman Spectra of Graphene Superlattices. *Phys. Rev. B* **2013**, *88* (8), 85401.

(20) Chari, T.; Ribeiro-Palau, R.; Dean, C. R.; Shepard, K. Resistivity of Rotated Graphite–Graphene Contacts. *Nano Lett.* **2016**, *16* (7), 4477–4482.

(21) Shen, C.; Li, N.; Wang, S.; Zhao, Y.; Tang, J.; Liu, J.; Tian, J.; Chu, Y.; Watanabe, K.; Taniguchi, T.; et. al. Observation of superconductivity with Tc onset at 12K in electrically tunable twisted double bilayer graphene. *arXiv:1903.06952* **2019**,

(22) Mogera, U.; Kurra, N.; Radhakrishnan, D.; Narayana, C.; Kulkarni, G. U. Low Cost, Rapid Synthesis of Graphene on Ni: An Efficient Barrier for Corrosion and Thermal Oxidation. *Carbon* **2014**, *78*, 384–391.

(23) Xu, R.; Su, Q. Chapter 2 - High-Temperature Synthesis; Xu, R., Pang, W., Huo, Q. B. T.-M. I. S. C., Eds.; Elsevier: Amsterdam, 2011; pp 9–38.

(24) Casiraghi, C. Doping Dependence of the Raman Peaks Intensity of Graphene Close to the Dirac Point. *Phys. Rev. B* **2009**, *80* (23), 233407.

(25) Wang, Y.; Su, Z.; Wu, W.; Nie, S.; Lu, X.; Wang, H.; McCarty, K.; Pei, S.; Robles-Hernandez, F.; Hadjiev, V. G.; et al. Four-Fold Raman Enhancement of 2D Band in Twisted Bilayer Graphene: Evidence for a Doubly Degenerate Dirac Band and Quantum Interference. *Nanotechnology* **2014**, *25* (33), 335201.

(26) Ferrari, A. C. Raman Spectroscopy of Graphene and Graphite: Disorder, Electron–Phonon Coupling, Doping and Nonadiabatic Effects. *Solid State Commun.* **2007**, *143* (1), 47–57.

(27) Kim, K.; Coh, S.; Tan, L. Z.; Regan, W.; Yuk, J. M.; Chatterjee, E.; Crommie, M. F.; Cohen, M. L.; Louie, S. G.; Zettl, A. Raman Spectroscopy Study of Rotated Double-Layer Graphene: Misorientation-Angle Dependence of Electronic Structure. *Phys. Rev. Lett.* **2012**, *108* (24), 246103.

(28) He, R.; Chung, T.-F.; Delaney, C.; Keiser, C.; Jauregui, L. A.; Shand, P. M.; Chancey, C. C.; Wang, Y.; Bao, J.; Chen, Y. P. Observation of Low Energy Raman Modes in Twisted Bilayer Graphene. *Nano Lett.* **2013**, *13* (8), 3594–3601.

(29) Chung, T.-F.; He, R.; Wu, T.-L.; Chen, Y. P. Optical Phonons in Twisted Bilayer Graphene with Gate-Induced Asymmetric Doping. *Nano Lett.* **2015**, *15* (2), 1203–1210.

(30) Cong, C.; Yu, T.; Saito, R.; Dresselhaus, G. F.; Dresselhaus, M. S. Second-Order Overtone and Combination Raman Modes of Graphene Layers in the Range of 1690–2150 cm^{-1}. *ACS Nano* **2011**, *5* (3), 1600–1605.

(31) Liu, H.-L.; Siregar, S.; Hasdeo, E. H.; Kumamoto, Y.; Shen, C.-C.; Cheng, C.-C.; Li, L.-J.; Saito, R.; Kawata, S. Deep-Ultraviolet Raman Scattering Studies of Monolayer Graphene Thin Films. *Carbon* **2015**, *81*, 807–813.

(32)   Luong, D. X.; Bets, K. V; Algozeeb, W. A.; Stanford, M. G.; Kittrell, C.; Chen, W.; Salvatierra, R. V; Ren, M.; McHugh, E. A.; Advincula, P. A.; et al. Gram-Scale Bottom-up Flash Graphene Synthesis. *Nature* **2020**, *577* (7792), 647–651.

(33)   Huang, S.; Yankowitz, M.; Chattrakun, K.; Sandhu, A.; LeRoy, B. J. Evolution of the Electronic Band Structure of Twisted Bilayer Graphene upon Doping. *Sci. Rep.* **2017**, *7* (1), 7611.

Chapter 4.2

Highly sensitive and stretchable strain sensor based on intrinsically wrinkled twisted multilayer graphene

Summary: Twisted multilayer graphene (tMLG) is found to have ripples along with wrinkles which minimise stress arising due to differential expansion of metal substrate and graphene during synthesis. These ripples were characterised by microscopic examination and were found to branch out from the wrinkles orthogonally. The wrinkle areas were found to be more conducting compared to the flatter regions as inferred from Joule heating experiment. On applying strain, wrinkle interconnections got altered which allowed morphological changes in the robust tMLG system. In-situ Raman measurement revealed that there was no change in the chemical nature of the graphene sheets when stretched and the resistance change occurred purely due to changes in wrinkle interconnections and crack propagation at the later stage. Optical micrographs before and during strain showed that the sensing areas have not changed much and confirmed this mechanism. The sensor showed good repeatability and stability after repeated straining and relaxing cycles, and prolonged straining, respectively. The sensor used simple vacuum deposition for fabrication and was

demonstrated to have an ultra-high gauge factor of 10^8 along with a strain range of 0%-45%.

4.2.1 Introduction

Strain sensors form an integral part of soft electronics with applications in health monitoring,[1–3] human-machine interfaces,[4] energy storage,[5] prosthetic limbs[6,7] etc. The traditional strain sensors employed various metals and semiconductors; their working principle being based on change in resistance on elongation. The resistance change can happen due to change in geometry and change in resistivity. As conventional metals and semiconductors lack stretchability (<5%), sensitivity and biological compatibility,[8] new age strain sensors are being fabricated using metal nanoparticles,[9,10] conducting polymers,[11,12] graphite,[13] carbon black,[14,15] carbon nanotubes,[16,17] graphene[18,19] or their hybrids.[20,21] 1D nanomaterials have been majorly sought for stretchable conductors because their percolation networks have good tolerance to mechanical stress, but they suffer from having high junction resistance at intersections, poor adhesion with the substrate and their low stability in high thermal and humid environment.[22] Graphene on the other hand has a truly flat surface which allows good adhesion to polymer substrates such as polydimethylsiloxane (PDMS).[23] Graphene has inherently high electrical conductivity and does not get easily corroded under hot and humid conditions.[22] As graphene is a 2D material, it inherently lacks stretchability, due to which pristine monolayer graphene cannot be used and hence some structural modification needs to be utilized to afford large structural deformations. Some of these methods involve pre stretching of the polymer before bringing graphene onto the

polymer,[24] making percolation network of crumpled and folded graphene by etching the host substrate with ammonium persufate[22] or making elastomeric filler graphene woven fabric[8] etc. Also, piezoresistive sensitivity of a pristine graphene is low,[25] its electrical conductivity changes poorly on being strained. Due to this, graphene strain sensors have low gauge factor, defined by ratio of change in resistance to change in strain, which indicates how sensitively the device measures a change in strain. High gauge factors are important for fast and reversible strain switching required in early warning systems. The sensitivity in strain sensors has been greatly improved in the recent years by utilising mechanisms such as charge tunnelling by depositing nanographene films on a flexible substrate,[25] crack propagation[26] and making graphene/epoxy composite.[27]
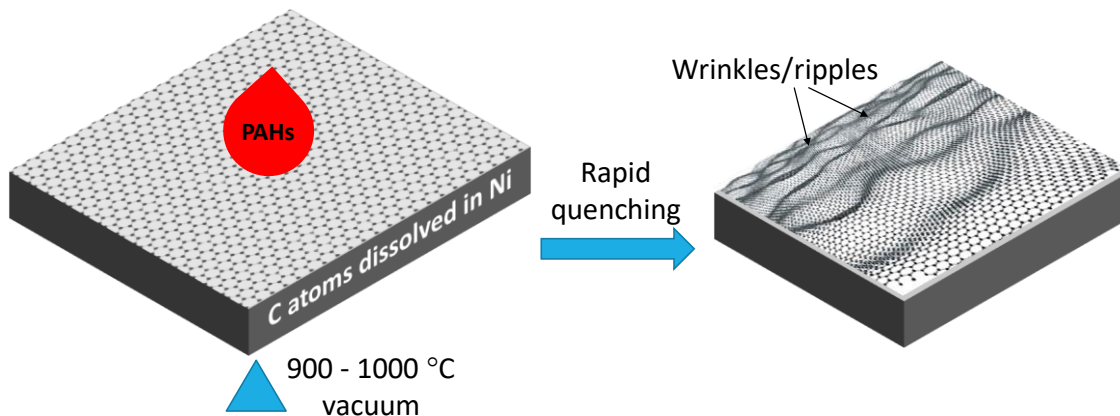

Figure 4.2.1 Process of wrinkle formation during graphene synthesis using chemical vapour deposition method. When polyaromatic hydrocarbons are drop casted on a Ni foil and heated at 900-1000 °C in vacuum, the carbon atoms are dissolved in the Ni and on rapid quenching, graphene sheets are ejected out having wrinkles in order to release the stress.[28]

For making strain sensors applicable for wider applications, it is necessary to have high gauge factor and wide strain range simultaneously. However, there always has been a trade-off between these parameters in most of the sensing materials. The surface of graphene is always found to have been associated with features such as wrinkles and ripples which minimise stress arising due to differential expansion of the metal surface and graphene during synthesis (see Figure 4.2.1).[29] Lim et. al. describes the wrinkles as pseudo 1D structures embedded in the 2D matrix.[30] These wrinkle networks are yet to be studied for observing high stretchability in the graphene.

4.2.2 Scope of the present investigation

The wrinkles structure on multi-layered graphene are utilised to make a strain sensor that simultaneously has high gauge factor and high strain range. The percolation network formed by these 1D structures observed in tMLG are utilised as sensing material for making the strain sensor and its performance is compared with other graphene-based sensors. The wrinkle structure is helpful to allow dispersing of stress to a great extent without cracking which has been previously achieved by prestretching the polymeric substrate before mounting the tMLG. As tMLG based strain sensor has both good stretching range as well as high gauge factor, it can be utilised to sense sensitive movements such as sound frequency and sense voices which requires high sensitivity. Raman spectroscopy can be used to decipher any chemical changes due to external strain and on comparing the optical micrographs, before and after strain, any morphological changes can be observed. A mechanism needs to be understood that explains how wrinkles are aiding the high stretchability or gauge factor in the sensor.

4.2.3 Experimental Section

A 7 μm Ni foil (7 mm × 30 mm, 99.9%, Advent Research Materials) was cut and fit in the slots of a vacuum chamber for passing current. A rotary pump was used to make a vacuum of 4×10^{-3} Torr. As a carbon source, 20 μL of 1 mM naphthalene solution in chloroform was drop-casted onto the fixed Ni foil and allowed to dry. An AC current of 20-25 A was passed for 15 minutes to make the foil red hot followed by sudden cooling. Temperature of the foil was measured using infrared thermometer MIKRON M90-R1. The Ni foil was etched away by keeping it in 1 M $FeCl_3$ for 8 hours followed by rinsing with deionised water. Raman spectra were recorded in backscattering geometry using the 532 nm excitation wavelength (Horiba XploRA ONE Raman microscope) with the laser power of ~2 mW at the sample surface.
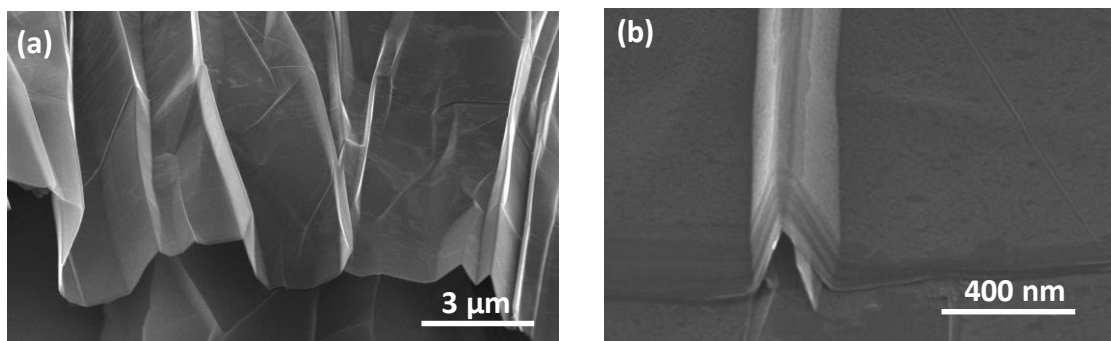
4.2.4 Results and Discussion

Figure 4.2.2 Wrinkle shape. Cross-sectional scanning electron microscopy of wrinkles present on tMLG.

The surface of graphene grown by chemical vapour deposition process, is usually found to have been associated with features like wrinkles and they are manifested when free graphene is suspended. In this work, the wrinkles were formed because of the

difference in thermal expansion coefficient of graphene and Ni, which is used as a catalyst for the growth of graphene. The features that appear brighter and mostly form crossed T-junctions are the wrinkles. They extend to a few micrometres and appear as if graphene has been folded, as apparent from the cross-sectional FESEM images in Figures 4.2.2a and b. The large number of interconnecting wrinkles show defect-free single layer like properties of tMLG. The flake contains several stacks of graphene layers.
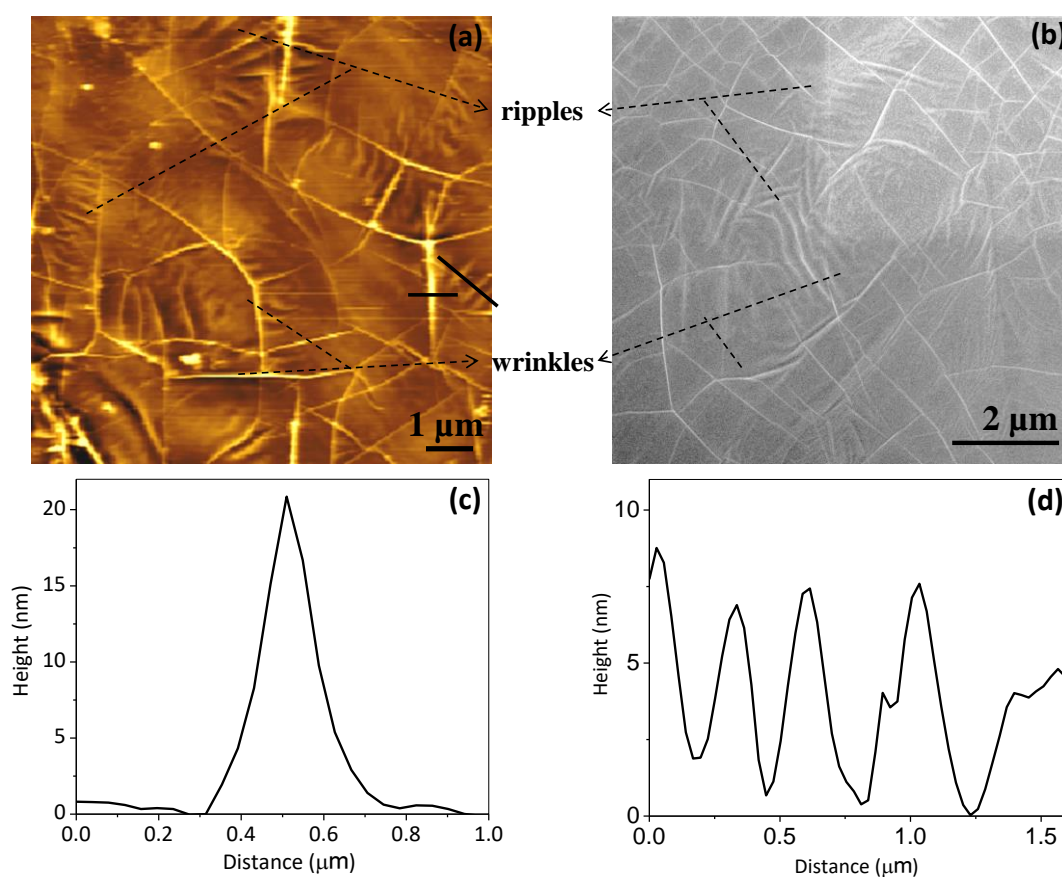

Figure 4.2.3 Size of wrinkles and ripples. Images of (a) AFM and (b) FESEM of graphene sheets showing wrinkles and ripples formed on its surface. Height profiles of wrinkle (c) and ripples (d) at the black line marked in (a), z-scale: 27 nm.

Each stack contains layers having common wrinkles whereas none share any wrinkle with the other stacks, making the stacks loosely bound to each other. Along with

wrinkles, the tMLG samples consist of several ripples originating from the wrinkles (see Figures 4.2.3a and b). These ripples are contained within polygons formed by wrinkles. Alternatively, wrinkles and ripples can be called as primary and secondary structures, respectively. The wrinkles are bigger with a height of about 20-22 nm while ripples are about 7-9 nm high, observed by height profiles in Figures 4.2.3c and d. The wrinkles are much lighter in contrast, as seen in the FESEM images (see Figure 4.2.3b), perhaps due to localisation of electrons in the region, showing that the wrinkles might be more conducting compared to the flatter regions. Unlike wrinkles, the ripples occur in multiplets and seem to exhibit a periodic wavelength, like those in water and hence, the word, ripples, is appropriate.
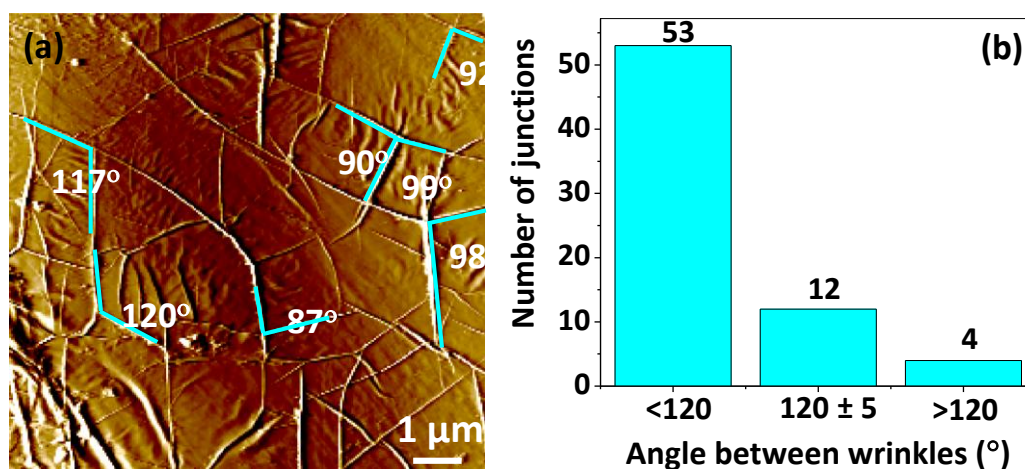

Figure 4.2.4 Angles between wrinkles. (a) AFM image of graphene surface showing different angles formed at T-junctions. (b) Histogram collected from the images of multiple regions of the sample showing the different angles formed at junctions.

The graphene surface was scanned under AFM and the angles formed at different junctions of wrinkles were measured as shown in Figure 4.2.4a. The number of junctions were plotted for different angular ranges (see Figure 4.2.4b). Among the three categories of the angles measured, it was seen that the junctions with a measured angle

between 90° and 120°, are the majorly formed structures. To study the conductivity through these wrinkles, a tMLG/PDMS device was fabricated. Graphene flake was mounted on PDMS substrate and contacts were made using silver epoxy paint. Briefly, a strip of polycrystalline Ni foil was connected between two electrodes in a chamber (see Figure 4.2.5a). Naphthalene solution in chloroform was drop coated on the Ni foil
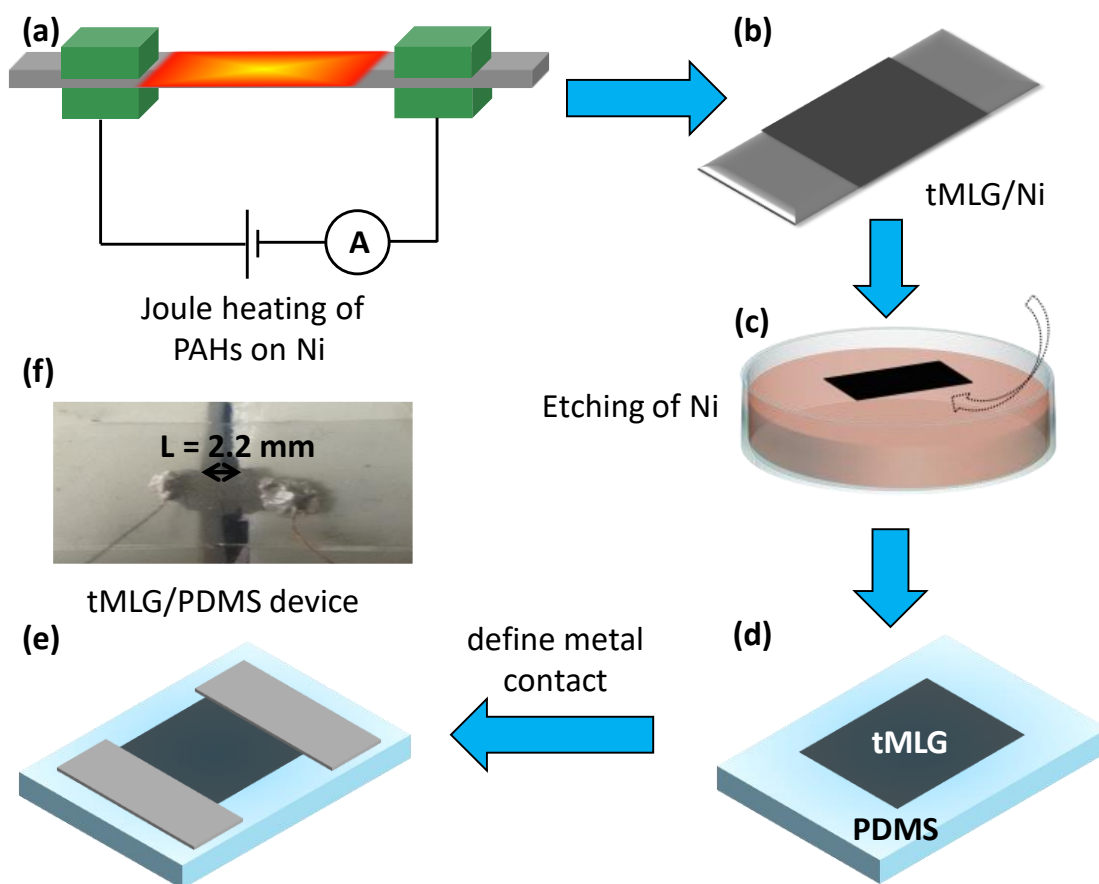

Figure 4.2.5 Synthesis of tMLG/PDMS device. (a) Schematic of synthesis of tMLG involving Joule heating of polyaromatic hydrocarbons (PAHs) coated on polycrystalline Ni foil connected to current electrodes in vacuum. (b) tMLG grown on Ni foil after cooling. (c) Etching of Ni foil in aqueous $FeCl_3$ to get free standing TG. (d) Scooping away tMLG graphene onto PDMS substrate. (e) silver epoxy contacts on both sides of tMLG flake. (f) Digital image of tMLG/PDMS device.

and allowed to dry before creating vacuum in the chamber. An AC current of 20-25 A was applied to Joule-heat the foil to red hot for 15 minutes and then was cooled immediately.[31] tMLG gets deposited in the middle of the foil, indicated by the black region in Figure 4.2.5b. The pressure was slowly brought back to 1 ATM and the tMLG coated foil was taken out of the chamber (see Figure 4.2.5c). In a petri-dish, 1M aqueous $FeCl_3$ solution was prepared and the tMLG coated Ni foil was kept floating on this solution overnight (see Figure 4.2.5d). In ~8 hours, the whole Ni got etched away. Rinsing the tMLG flake several times with deionised water, several free-standing flakes having an average area of ~4 mm² were obtained. For preparing a flexible substrate, PDMS prepolymer and curing agent were taken in the ratio 10:1 and whisked vigorously using a glass rod. Desiccating for 15 minutes, 3 mL of this mixture was poured on a PET sheet surrounded by a Cu ring, acting as a mould. Curing the mixture for 40 minutes at 80 °C, PDMS film was obtained. The film was cut into sizes of 1 cm × 3 cm to be used as a flexible substrate of the sensor. One of the free standing graphene flakes was scooped out using a glass slide and was put on PDMS substrate as shown in Figure 4.2.5d, followed by blowing with a hot air gun and heating in an oven at 100 °C for 2 hours to get rid of any water content. To make the electrodes, Silver epoxy paste A and B were mixed in equal amounts and cured on both the sides of the tMLG flake for 2 hours at 200 °C to get the tMLG/PDMS device (see Figure 4.2.5e); the camera photograph is shown in Figure 4.2.5f.
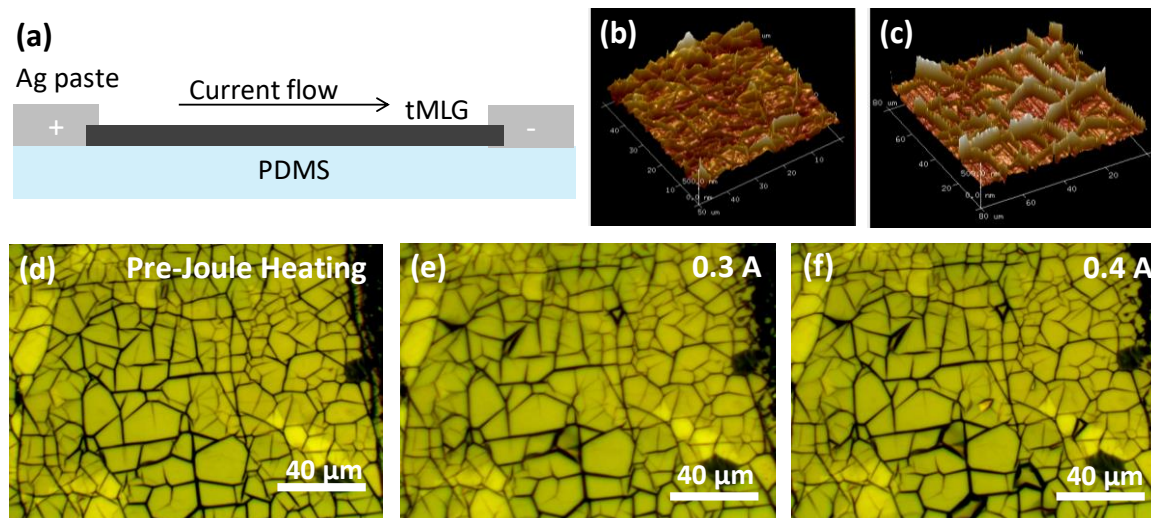
Figure 4.2.6 Joule heating experiment. (a) Schematic of joule heating set up. AFM of the wrinkles (b) before and (c) after joule heating. Optical micrographs of graphene wrinkles before starting joule heating (d), after providing 0.3 A for 30 s (e) and after further providing 0.4 A for 30 s.

This device was used to study the conductivity through wrinkles by Joule heating. For this, the device was connected to a DC power supply at constant current (see Figure 4.2.6a), while being kept under optical microscope to record the live changes in the tMLG flake. The current was applied in steps of 0.1 A for 30 s at each value, starting from 0.1 A. On comparing the optical micrographs in Figures 4.2.6d and e, it was observed that few wrinkle junctions have erupted randomly, probably due to higher Joule heating in these junctions. On further increasing the current, few more junctions got erupted (see Figure 4.2.6f), finally breaking the current flow after 0.5 A, due to complete loss of connectivity between the two contacts, as can be observed by comparing the AFM images in Figures 4.26b and c. This indicates that the probability of current flowing through the wrinkles is higher compared to flatter regions, due to which more Joule

heating takes place in the wrinkles and even more in junctions leading to burning of these regions. This property of wrinkles was utilised to use the tMLG/PDMS device as a strain sensor.
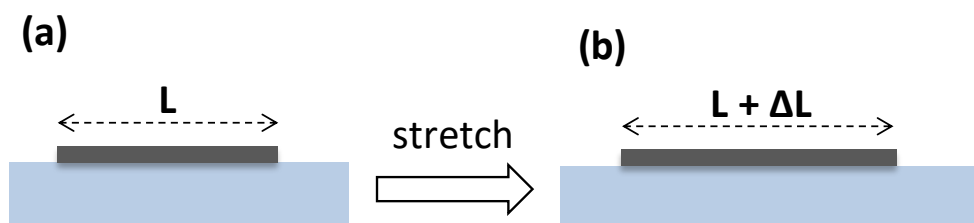

Figure 4.2.7 Schematic of tMLG based strain sensor on PDMS in (a) relaxed and (b) stretched states.

The electrical performance of the device was tested by measuring the current while sweeping voltage from -0.1 V to +0.1 V at different strains (see Figures 4.2.7a and b for the schematic of sensor in relaxed and stretched state). In order to observe the change in current at higher strains, the current values were plotted in log scale against voltage as shown in Figure 4.2.8a. The sensor clearly shows decrease in current at each increase in strain value. Plotting the resistance at 0.1 V versus strain values, a monotonic increase was observed with two regimes, I and II (see Figure 4.2.8b). Gauge factor, expressed as the ratio of relative change in resistance and change in strain, measures the sensitivity of the sensor. From Figure 4.2.8b, regime II is more sensitive than the regime I, however both can be fit linearly. The linearity is a crucial factor for accurate calibration of the device. The device also shows fast response and recovery times, 0.31 s and 0.10 s respectively (see Figure 4.2.8c). The sensor apart from tensile stretching is also sensitive

to bending. Figure 4.2.8d displays decrease in current values while sweeping from -0.1 V to +0.1 V for each decrease in bending radius.
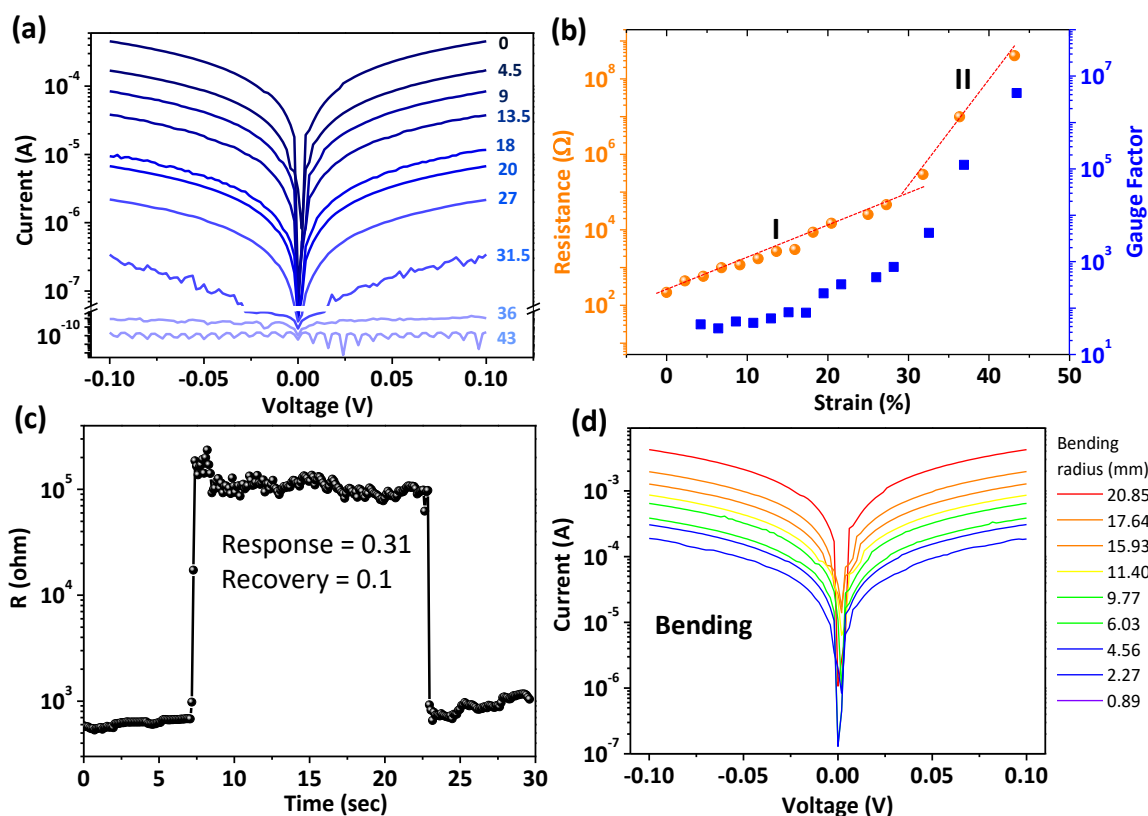

Figure 4.2.8 Plot $\log_{10}|I|$ versus Voltage for various tensile strains (0% to 45%). (b) Plot of resistance versus strain for a strain sensor device going through two slopes I and II, gauge factor is marked on the y-axis at the right. (c) Response and recovery time measured for resistance versus time plot. (d) Plot of $\log_{10}|I|$ versus Voltage for various bending strains.

To understand the mechanism of resistance-change on straining, Raman was measured on tMLG, before and after providing strain of 45%. There was no change in the D peak (see D intensity map in Figure 4.2.9), confirming that the external strain does not lead to any change in the interaction among graphene layers. As has been studied previously,[32] the wrinkles act like highways of current. Morphological studies

were done by capturing optical micrographs while straining a sensor, to realize any contribution from the wrinkles. The reflection mode micrographs at 0%, 30% and 45% strains are shown in the Figures 4.2.10a-c followed by a micrograph of the same region on returning to an unstrained state. It is quite evident that, initially at 0% strain, there are wrinkles present randomly in all directions and they are well connected. As the strain is applied vertically, the horizontal wrinkles start to fade away, fading completely at 45% strain, as can be clearly seen at the regions marked with red arrows in grayscale images. This leads to reduction in the connectivity among wrinkles, making the current to pass through the flatter regions. The flatter regions being less conductive, contribute to increase in resistance of the sensor. The sensor completely restores its original morphology on being relaxed as shown in the rightmost image, the wrinkles get connected, identical to the original morphology, hence returning to the original electrical performance Figure 4.2.10b shows lower magnification transmittance mode optical micrographs of the same region at 0%, 30% and 45% strains, followed by high magnification micrograph of the 45% strained state. Figure 4.2.10d, showing the change in resistance while increasing (black) and decreasing (red) strain between 0% and 30%, exhibits no hysteresis because till this stage, there are only morphological changes in the tMLG and there is no crack formation. As the strain exceeds 30%, cracks start to appear, finally becoming large enough to completely isolate the two electrodes at the strain of 45%. When change in resistance was recorded for increasing the strain to this limit, hysteresis was observed on relaxing the strain as depicted in Figure 4.2.10e. However, the resistance reached its original value on complete relaxation.
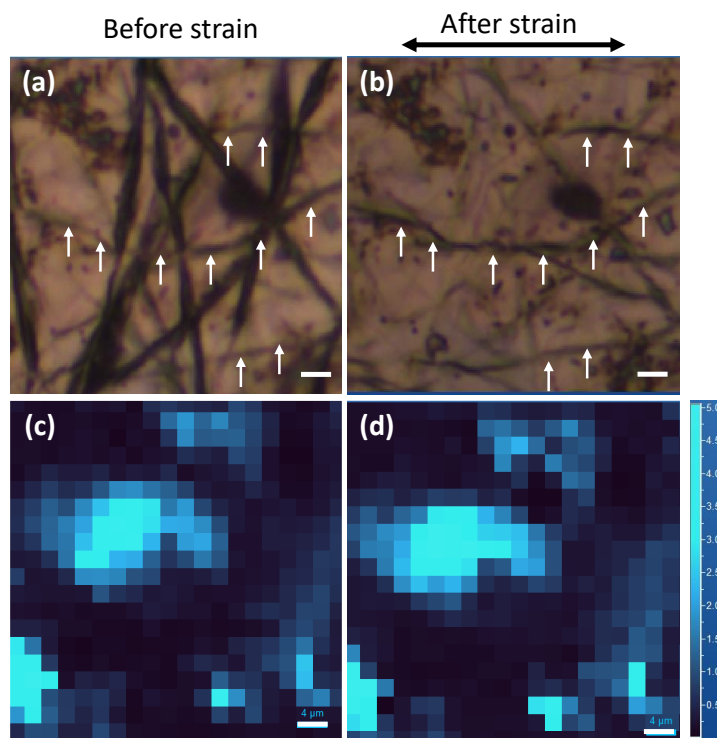
Figure 4.2.9 Optical images of tMLG (a) before and (b) after applying strain with corresponding Raman maps of normalised D peak intensity in (c) and (d) respectively. The scale bar is 4 μm. The strain direction is shown by black double-sided arrow. The white arrows represent the wrinkles in the direction of the strain that remain unaffected with strain.

The mechanism of change in resistance on stretching has been shown in Figure 4.2.10c. First, the wrinkles become flatter and become less in number leading to less percolation connectivity and thereby have higher resistance. On further increase in strain, cracks start to appear, making the current flow restricted, finally completely isolating the two regions. The sensor was stretched to 45% and relaxed for 10 cycles to see the robustness and electrodes. Figures 4.2.11a and b show a region before and after stretching it to its maximum limit (45%) in the vertical direction. It can be observed that a maximum number of wrinkles are present in the vertical direction. However, due
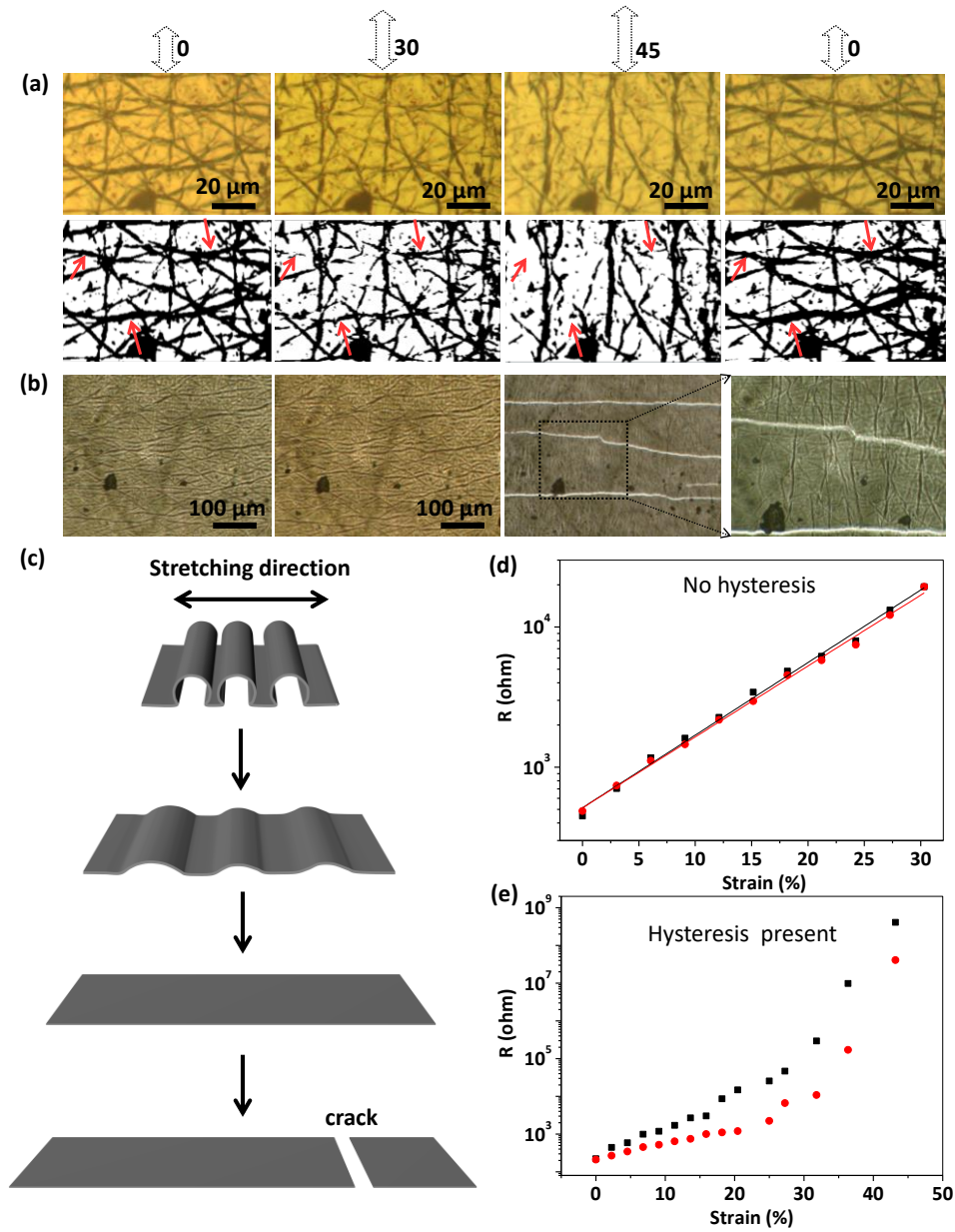
Figure 4.2.10 Optical Micrographs with corresponding 8-bit grayscale images as strain is increased from 0% to 45% and then brought back to 0%. The red arrows are marked at three regions to observe changes in a particular area on being strained. (b) Optical micrographs at lower magnification showing the appearance of cracks when the sensor is stretched beyond 45%. (c) Schematic of stepwise change in graphene morphology on providing strain. (d) Change in resistance of the strain sensor while increasing (black) the strain from 0% to 30% and returning (red) back. (e) Change in resistance of the strain sensor while increasing (black) the strain from 0% to 45% and returning back.

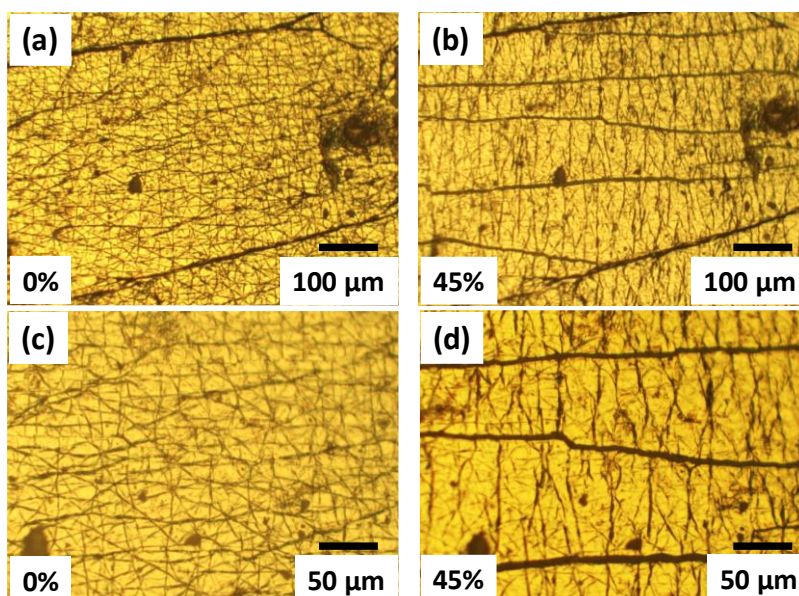**Figure 4.2.11** Optical micrographs of tMLG/PDMS in relaxed (a) and stretched (b) condition and the corresponding high magnification micrographs in (c) and (d) respectively.
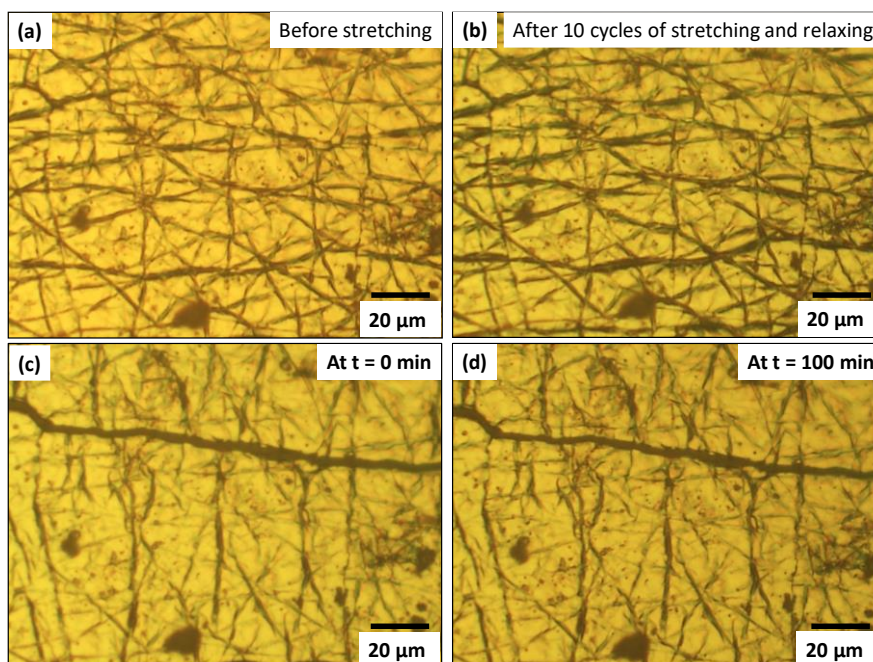

Figure 4.2.12 Optical micrographs of tMLG strain sensor before (a), and after (b), carrying out 10 stretching and relaxing cycles. Micrographs of stretched sensor at 0 minute (c), and at 100 minutes.

to the presence of cracks passing through all the vertical wrinkles, the wrinkles have broken into sections losing their connectivity. The Figures 4.2.11c and d show the magnified view of the same region. The sensor was stretched to 45% and relaxed for 10 cycles to see the robustness and reproducibility. The wrinkles after all the cycles resemble very well with the original ones (see Figures 4.2.12a and b). This means that there is no permanent change in the graphene morphology and the sensor gives reproducible results for over 10 cycles. One of the sensors was kept in stretched state for 100 minutes and there was no noticeable relaxation observed (see Figures 4.2.12c and d). It is evident that the sensor is stable and remains in a constant morphology under a strain.
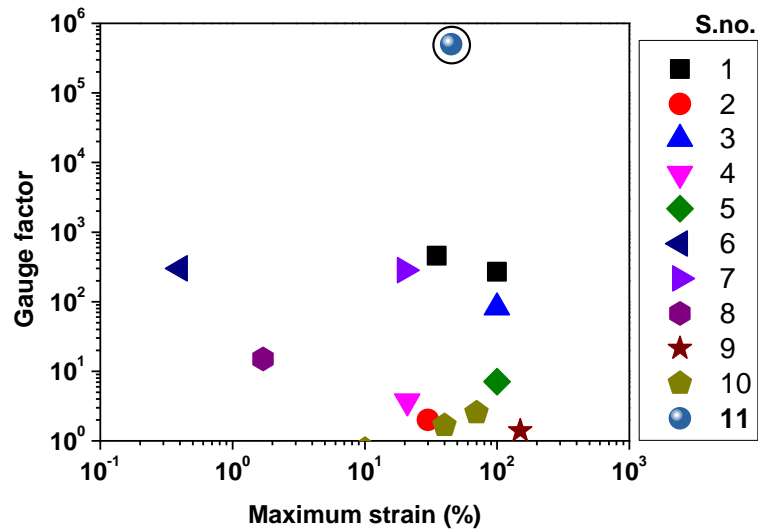

Figure 4.2.13 Plot of gauge factor versus maximum strain for best strain sensors reported in literature.

For a strain sensor to be effective for a large number of applications, it needs to be highly sensitive and have good range of stretchability simultaneously. A lot of reports

show highly stretchable sensors but lose out on the sensitivity (see Table 4.2.1). The tMLG based sensor shows these two properties owing to its reversible wrinkle interconnections. The wrinkles act like highways for current conduction and multilayer structure gives it robustness under frequent strain cycles. As can be seen in Figure 4.2.13, most of the sensors lie near the axes of the plot between maximum strain and gauge factor. On the other hand, tMLG based sensors have optimum values for both the parameters making its applicability diverse.

Table 4.2.1 Parameters for best strain sensors reported in literature (current work is marked in bold).

S. no.	Materials	Maximum workable range (%)	Gauge factor
1	Laser patterned graphene[4]	35	457
		100	268
2	Graphene ripples on PDMS[23]	30	2
3	Graphene Rubber Composite[33]	100	82.5
4	3D Graphene Foam/PDMS Composite[34]	21	3.7
5	Graphene-Nanocellulose films[35]	100	7.1
6	Nanographene films[25]	0.4	300
7	Graphene woven fabrics on polymer[8]	20	282
8	Graphene-based layered percolative film[36]	1.7	15

9	Layer-by-layer assembly of graphene on nylon covered rubber[37]	150	~1.4
10	Entangled graphene mesh network[22]	10	0.76
		40	1.67
		70	2.55
11	**Current work (TG)**	**45**	**0.1-10^6**

4.2.5 Conclusions

Twisted multilayer graphene was successfully mounted on top of a PDMS substrate to work as a strain sensor. The wrinkles align in one direction losing connectivity when external strain is provided which leads to increase in resistance linearly. Further straining induces cracks and the sensitivity becomes very high in this regime, reaching a gauge factor 10^8 at a strain of 45%. The sensor shows good repeatability for 10 cycles and is robust under frequent cycling. The sensor holds a promise for new age sensors requiring simultaneous high sensitivity and stretchability.

4.2.6 References

(1)   Yin, F.; Lu, H.; Pan, H.; Ji, H.; Pei, S.; Liu, H.; Huang, J.; Gu, J.; Li, M.; Wei, J. Highly Sensitive and Transparent Strain Sensors with an Ordered Array Structure of AgNWs for Wearable Motion and Health Monitoring. *Sci. Rep.* **2019**, *9* (1), 2403.

(2)   Kang, I.; Schulz, M. J.; Kim, J. H.; Shanov, V.; Shi, D. A Carbon Nanotube Strain Sensor for Structural Health Monitoring. *Smart Mater. Struct.* **2006**, *15* (3), 737–748.

(3)   Gupta, N.; Rao, K. D. M.; Srivastava, K.; Gupta, R.; Kumar, A.; Marconnet, A.; Fisher, T. S.; Kulkarni, G. U. Cosmetically Adaptable Transparent Strain Sensor for Sensitively Delineating Patterns in Small Movements of Vital Human Organs. *ACS Appl. Mater. Interfaces* **2018**, *10* (50), 44126–44133.

(4)   Wu, Y.; Karakurt, I.; Beker, L.; Kubota, Y.; Xu, R.; Ho, K. Y.; Zhao, S.; Zhong, J.; Zhang, M.; Wang, X.; et al. Piezoresistive Stretchable Strain Sensors with Human Machine Interface Demonstrations. *Sensors Actuators A Phys.* **2018**, *279*, 46–52.

(5)   Peng, J.; Zhou, X.; Jia, S.; Jin, Y.; Xu, S.; Chen, J. High Precision Strain Monitoring for Lithium Ion Batteries Based on Fiber Bragg Grating Sensors. *J. Power Sources* **2019**, *433*, 226692.

(6)   Zainuddin, N. 'Aqilah; Anuar, N. F.; Mansur, A. L.; Fauzi, N. I. M.; Hanim, W. F.; Herman, S. H. Resistive-Based Sensor System for Prosthetic Fingers Application. *Procedia Comput. Sci.* **2015**, *76*, 323–329.

(7)   Kim, J.; Lee, M.; Shim, H. J.; Ghaffari, R.; Cho, H. R.; Son, D.; Jung, Y. H.; Soh, M.; Choi, C.; Jung, S.; et al. Stretchable Silicon Nanoribbon Electronics for Skin Prosthesis. *Nat. Commun.* **2014**, *5* (1), 5747.

(8)   Liu, X.; Liu, D.; Lee, J.; Zheng, Q.; Du, X.; Zhang, X.; Xu, H.; Wang, Z.; Wu, Y.; Shen, X.; et al. Spider-Web-Inspired Stretchable Graphene Woven Fabric for Highly Sensitive, Transparent, Wearable Strain Sensors. *ACS Appl. Mater. Interfaces* **2019**, *11* (2), 2282–2294.

(9)   Lee, J.; Kim, S.; Lee, J.; Yang, D.; Park, B. C.; Ryu, S.; Park, I. A Stretchable Strain Sensor Based on a Metal Nanoparticle Thin Film for Human Motion Detection.

Nanoscale **2014**, *6* (20), 11932–11939.

(10) Herrmann, J.; Müller, K.-H.; Reda, T.; Baxter, G. R.; Raguse, B.; de Groot, G. J. J. B.; Chai, R.; Roberts, M.; Wieczorek, L. Nanoparticle Films as Sensitive Strain Gauges. *Appl. Phys. Lett.* **2007**, *91* (18), 183105.

(11) Wang, Y.; Zhu, C.; Pfattner, R.; Yan, H.; Jin, L.; Chen, S.; Molina-Lopez, F.; Lissel, F.; Liu, J.; Rabiah, N. I.; et al. A Highly Stretchable, Transparent, and Conductive Polymer. *Sci. Adv.* **2017**, *3* (3), e1602076.

(12) Wang, T.; Zhang, Y.; Liu, Q.; Cheng, W.; Wang, X.; Pan, L.; Xu, B.; Xu, H. A Self-Healable, Highly Stretchable, and Solution Processable Conductive Polymer Composite for Ultrasensitive Strain and Pressure Sensing. *Adv. Funct. Mater.* **2018**, *28* (7), 1705551.

(13) Zhang, M.; Wang, C.; Wang, Q.; Jian, M.; Zhang, Y. Sheath–Core Graphite/Silk Fiber Made by Dry-Meyer-Rod-Coating for Wearable Strain Sensors. *ACS Appl. Mater. Interfaces* **2016**, *8* (32), 20894–20899.

(14) Cochrane, C.; Koncar, V.; Lewandowski, M.; Dufour, C. Design and Development of a Flexible Strain Sensor for Textile Structures Based on a Conductive Polymer Composite. *Sensors* . 2007.

(15) Liu, P.; Liu, J.; Zhu, X.; Wu, C.; Liu, Y.; Pan, W.; Zhao, J.; Guo, X.; Liu, C.; Huang, Y.; et al. A Highly Adhesive Flexible Strain Sensor Based on Ultra-Violet Adhesive Filled by Graphene and Carbon Black for Wearable Monitoring. *Compos. Sci. Technol.* **2019**, *182*, 107771.

(16) Sahatiya, P.; Badhulika, S. Eraser-Based Eco-Friendly Fabrication of a Skin-like

Large-Area Matrix of Flexible Carbon Nanotube Strain and Pressure Sensors. *Nanotechnology* **2017**, *28* (9), 95501.

(17) Yu, L.; Shearer, C.; Shapter, J. Recent Development of Carbon Nanotube Transparent Conductive Films. *Chem. Rev.* **2016**, *116* (22), 13413–13453.

(18) Wang, Y.; Hao, J.; Huang, Z.; Zheng, G.; Dai, K.; Liu, C.; Shen, C. Flexible Electrically Resistive-Type Strain Sensors Based on Reduced Graphene Oxide-Decorated Electrospun Polymer Fibrous Mats for Human Motion Monitoring. *Carbon N. Y.* **2018**, *126*, 360–371.

(19) Yang, Z.; Pang, Y.; Han, X.; Yang, Y.; Ling, J.; Jian, M.; Zhang, Y.; Yang, Y.; Ren, T.-L. Graphene Textile Strain Sensor with Negative Resistance Variation for Human Motion Detection. *ACS Nano* **2018**, *12* (9), 9134–9141.

(20) Zheng, Y.; Li, Y.; Dai, K.; Wang, Y.; Zheng, G.; Liu, C.; Shen, C. A Highly Stretchable and Stable Strain Sensor Based on Hybrid Carbon Nanofillers/Polydimethylsiloxane Conductive Composites for Large Human Motions Monitoring. *Compos. Sci. Technol.* **2018**, *156*, 276–286.

(21) Fan, X.; Wang, N.; Yan, F.; Wang, J.; Song, W.; Ge, Z. A Transfer-Printed, Stretchable, and Reliable Strain Sensor Using PEDOT:PSS/Ag NW Hybrid Films Embedded into Elastomers. *Adv. Mater. Technol.* **2018**, *3* (6), 1800030.

(22) Han, J.; Lee, J.-Y.; Lee, J.; Yeo, J.-S. Highly Stretchable and Reliable, Transparent and Conductive Entangled Graphene Mesh Networks. *Adv. Mater.* **2018**, *30* (3), 1704626.

(23) Wang, Y.; Yang, R.; Shi, Z.; Zhang, L.; Shi, D.; Wang, E.; Zhang, G. Super-Elastic

Graphene Ripples for Flexible Strain Sensors. *ACS Nano* **2011**, *5* (5), 3645–3650.

(24) Wu, H.; Liu, Q.; Du, W.; Li, C.; Shi, G. Transparent Polymeric Strain Sensors for Monitoring Vital Signs and Beyond. *ACS Appl. Mater. Interfaces* **2018**, *10* (4), 3895–3901.

(25) Zhao, J.; He, C.; Yang, R.; Shi, Z.; Cheng, M.; Yang, W.; Xie, G.; Wang, D.; Shi, D.; Zhang, G. Ultra-Sensitive Strain Sensors Based on Piezoresistive Nanographene Films. *Appl. Phys. Lett.* **2012**, *101* (6), 63112.

(26) Ferrari, A. C. Raman Spectroscopy of Graphene and Graphite: Disorder, Electron–Phonon Coupling, Doping and Nonadiabatic Effects. *Solid State Commun.* **2007**, *143* (1), 47–57.

(27) Lee, Y.; Jin, W.-Y.; Cho, K. Y.; Kang, J.-W.; Kim, J. Thermal Pressing of a Metal-Grid Transparent Electrode into a Plastic Substrate for Flexible Electronic Devices. *J. Mater. Chem. C* **2016**, *4* (32), 7577–7583.

(28) Mogera, U.; Sundaresan, A.; Kulkarni, G. U. Graphene–Ni(111) Synergy Influencing Crystalline Orientation, Grain Morphology and Magnetic Properties of Poly-Ni. *J. Phys. Chem. C* **2018**, *122* (25), 13962–13968.

(29) Amini, S.; Kalaantari, H.; Garay, J.; Balandin, A.; Abbaschian, R. Growth of Graphene and Graphite Nanocrystals from a Molten Phase. *J. Mater. Sci.* **2011**, *46*, 6255–6263.

(30) Wang, B.; Huang, M.; Kim, N. Y.; Cunning, B. V; Huang, Y.; Qu, D.; Chen, X.; Jin, S.; Biswal, M.; Zhang, X.; et al. Controlled Folding of Single Crystal Graphene. *Nano Lett.* **2017**, *17* (3), 1467–1473.

(31) Mogera, U.; Dhanya, R.; Pujar, R.; Narayana, C.; Kulkarni, G. U. Highly Decoupled Graphene Multilayers: Turbostraticity at Its Best. *J. Phys. Chem. Lett.* **2015**, *6* (21), 4437–4443.

(32) Zhu, W.; Low, T.; Perebeinos, V.; Bol, A. A.; Zhu, Y.; Yan, H.; Tersoff, J.; Avouris, P. Structure and Electronic Transport in Graphene Wrinkles. *Nano Lett.* **2012**, *12* (7), 3431–3436.

(33) Lin, Y.; Liu, S.; Chen, S.; Wei, Y.; Dong, X.; Liu, L. A Highly Stretchable and Sensitive Strain Sensor Based on Graphene–Elastomer Composites with a Novel Double-Interconnected Network. *J. Mater. Chem. C* **2016**, *4* (26), 6345–6352.

(34) Maturos, T.; Phokaratkul, D.; Jaruwongrungsee, K.; Wisitsoraat, A.; Maturos, K.; Lomas, T.; Tuantranont, A. Fabrication of Stretchable 3D Graphene Foam/Poly-Dimethylsiloxane Composites for Strain Sensing. In *2015 IEEE 15th International Conference on Nanotechnology (IEEE-NANO)*; 2015; pp 1231–1234.

(35) Yan, C.; Wang, J.; Kang, W.; Cui, M.; Wang, X.; Foo, C. Y.; Chee, K. J.; Lee, P. S. Highly Stretchable Piezoresistive Graphene–Nanocellulose Nanopaper for Strain Sensors. *Adv. Mater.* **2014**, *26* (13), 2022–2027.

(36) Hempel, M.; Nezich, D.; Kong, J.; Hofmann, M. A Novel Class of Strain Gauges Based on Layered Percolative Films of 2D Materials. *Nano Lett.* **2012**, *12* (11), 5714–5718.

(37) Park, J. J.; Hyun, W. J.; Mun, S. C.; Park, Y. T.; Park, O. O. Highly Stretchable and Wearable Graphene Strain Sensors with Controllable Sensitivity for Human Motion Monitoring. *ACS Appl. Mater. Interfaces* **2015**, *7* (11), 6317–6324.

Chapter 5

Summary and Outlook

The thesis is essentially about two systems which are 2 dimensional in behavior but are mixed dimensional systems in physical terms. The thesis also explores the possible applications of these systems.

Chapter 3 discusses the metal mesh network, which has dimensionality between 1 and 2, because of being built up of metal wires (1D) into a flat surface (2D), which allows them to be transparent through the voids in the 2D structure and conducting through the metal wires. This property was utilized to make top electrodes of Si solar cells, making them more efficient and cost effective compared to the conventional screen-printed Ag electrodes. The other specialty of the mesh structure is that it is easy to be embedded into a polymer matrix, which has been utilized to make a strain sensor. The same device also works as a break junction, which joins itself after being broken, if kept undisturbed for a given time. The healing is expected to be faster on providing a voltage.

Solar cells generally make use of transparent conductors such as ITO, FTO, which increases their costs. The mesh holds good promise to be used in perovskite and tandem solar cells. It can also be tried for making see through devices. In this direction, research is going on in the lab currently and some results have already been achieved by the other lab members. The strain sensor can be used for continuous online health

monitoring of pulse, diet, sleeping, etc. The break junctions could be utilized for making self-healing components for artificial skin.

Chapter 4 presents a better understanding of Twisted Multilayer Graphene which has several layers (3D), twisted with respect to each other, thus behaving like a single layer (2D). A term called turbostratic factor has been defined to describe how much single layer like behavior is there in the system. This term can be used to describe the nature of other 2D materials as well which are twisted. Apart from this, the electron diffraction pattern intensities have been analyzed to figure out maximum relative Raman intensities of a system. The analysis is in good agreement with the experimental values in literature. The second part of the chapter demonstrates application of this graphene as a strain sensor based on change in resistance with opening and closing of wrinkles on applying strain. The strain sensor has a high gauge factor and stretching range simultaneously, making it suitable for detecting most of the movements in the human body. Its application can be further explored to detect audible frequencies.

Twisted multilayer graphene is a superior material for making dispersions compare to RGO, as it is free from defects. Ampacity measurements can be tried out to measure the current carrying capacity of this graphene as the layers are mutually non-interacting. Its usage in supercapacitor can also be explored. As twisted graphene have already demonstrated to show superconductivity at 1.1°, the same can be explored for this system which possesses a wide range of twists in it.

Publications

Highly conformal Ni micromesh as a current collecting front electrode for reduced cost Si solar cell

N. Gupta, K. D. M. Rao, R. Gupta, F. C. Krebs & G. U. Kulkarni

ACS Applied Materials & Interfaces, 2017, 9, 863

Cosmetically Adaptable Transparent Strain Sensor for Sensitively Delineating Patterns in Small Movements of Vital Human Organs

N. Gupta, K. D. M. Rao, K. Srivastava, R. Gupta, A. Kumar, A. Marconnet, T. S. Fisher & G. U. Kulkarni

ACS Applied Materials & Interfaces, 2018, 10, 44126

Stress modulation in desiccating crack networks for producing effective templates for patterning metal network based transparent conductors

A. Kumar, R. Pujar, **N. Gupta,** S. Tarafdar & G. U. Kulkarni

Applied Physics Letters, 2017, 111, 013502

Twist dependent Raman and Electron Diffraction Correlations in Twisted Multilayer Graphene

N. Gupta, W. Sunil, U. Mogera & G. U. Kulkarni

The Journal of Physical Chemistry Letters, 2020, 11, 8, 2797-2803

Highly sensitive and stretchable strain sensor based on intrinsically wrinkled twisted multilayer graphene

N. Gupta, U. Mogera & G. U. Kulkarni

2020, submitted

Electrical field assisted healing of nano-constrictions in Au break junctions

N. Gupta & G. U. Kulkarni

2020, submitted

Observation of surface enhanced Raman spectroscopy in corrugated surface of Au mesh network embedded in polystyrene

N. Gupta & G. U. Kulkarni

2020, under preparation

Patents

Solar cell and method therefore

N. Gupta, K. D. M. Rao & G. U. Kulkarni

Indian patent, Application No. 201741003497

Date of filing: January 31, 2017

Turbostratic Graphene dispersions, coatings, and process therefore

N. Gupta, U. Mogera & G. U. Kulkarni

Indian patent, Application No. 201741004449

Date of Filing: February 07, 2017